UNIVERSITY OF CALIFORNIA SAN DIEGO

Mechanical Effects of Regional Structural Remodeling in the Left Ventricle

A dissertation submitted in partial satisfaction of the
requirements for the degree Doctor of Philosophy

in

Bioengineering with a Specialization in Multi-Scale Biology

by

Eric David Carruth

Committee in charge:

Professor Jeffrey H. Omens, Chair
Professor Lawrence R. Frank, Co-Chair
Professor Adam J. Engler
Professor Andrew D. McCulloch
Professor Kirk L. Peterson

2018

The Dissertation of Eric David Carruth is approved, and it is acceptable in quality and form for publication on microfilm and electronically:

_____

_____

_____

_____
Co-chair

_____
Chair

University of California San Diego

2018

DEDICATION

This work is dedicated to my incredible wife Kimberly, who has dealt with the challenges of bearing, delivering, and raising three (amazing) children in less-than-ideal circumstances during the difficult years I was a PhD student, all while encouraging me to do my best work, despite her day job being much more difficult (and important) than my own.

It is also dedicated to my children. If I can complete a PhD, you kids can do anything if you are persistent.

EPIGRAPH

A new heart also will I give you, and a new spirit will I put within you: and I will take away the stony heart out of your flesh, and I will give you an heart of flesh.

Ezekiel 36:26

TABLE OF CONTENTS

Signature Page iii

Dedication iv

Epigraph v

Table of Contents vi

List of Abbreviations ix

List of Figures xi

List of Tables xiii

Acknowledgements xiv

Vita xvii

Abstract of the Dissertation xviii

Chapter 1. Transmural Gradients of Myocardial Structure and Mechanics: Implications for Fiber Stress and Strain in Pressure Overload 1
- 1.1. Introduction to Regional Gradients 2
- 1.2. Fiber Strain and Stress 4
  - 1.2.1. Fiber Strain 4
  - 1.2.2. Fiber Stress 9
  - 1.2.3. Mechanisms of Uniform Fiber Stress and Strain 11
- 1.3. Transmural Gradients as Mechanisms of Uniform Fiber Stress and Strain 13
  - 1.3.1. Fiber Angle and Torsion 13
  - 1.3.2. Material Anisotropy 15
  - 1.3.3. Residual Stress 17
  - 1.3.4. Protein Densities 18
- 1.4. Summary and Conclusions 27
- 1.5. Scope of the Dissertation 28
- 1.6. Acknowledgements 30
- 1.7. References 31

Chapter 2 Regional Gradients of Calcium Handling and Sarcomere Activating Proteins in Pressure Overload Hypertrophy in the Rat Ventricles 50
- 2.1. Introduction 50
- 2.2. Materials and Methods 52
  - 2.2.1. Transverse Aortic Constriction (TAC) Surgery 52

2.2.2. Dissection into Regions 52
2.2.3. Protein Isolation 53
2.2.4. Western Blot 54
2.2.5. Data Analysis and Statistics 54
2.2.6. Immunofluorescence Microscopy of Entire Ventricle Cross-Sections 55
2.2.7. Tissue Sectioning, Staining, and Imaging 56
2.3. Results 58
2.3.1. Transverse Aortic Constriction (TAC) 58
2.3.2. Western Blot 59
2.3.3. Immunofluorescence Microscopy of Entire Ventricle Cross-Sections 61
2.4. Discussion 63
2.5. Acknowledgements 64
2.6. References 65

Chapter 3. Regional Variations in Diffusion Tensor Anisotropy are Associated with Myocyte Remodeling in Left Ventricular Pressure Overload 68
3.1. Introduction 68
3.2. Methods 71
3.2.1. Pressure Overload Hypertrophy Model and Tissue Preparation 71
3.2.2. Diffusion Tensor MRI Acquisition 72
3.2.3. Tissue Sectioning, Staining, and Confocal Microscopy 73
3.2.4. Image Processing, Registration, Mesh Generation, and Parameter Calculation 74
3.2.5. Statistics 77
3.3. Results 78
3.3.1. Transverse Aortic Constriction and Left Ventricular Hypertrophy 78
3.3.2. Diffusion Tensor MRI 84
3.3.3. Confocal Micrographs 87
3.3.4. Correlations Between DT-MRI and Myocyte Geometry 87
3.4. Discussion 88
3.5. Acknowledgements 93
3.6. Appendix 94
3.7. References 102

Chapter 4. Myocardial Infarction Sizing in the Mouse by 3D Multiplanar Reconstruction of Late Gadolinium Enhanced Magnetic Resonance Cardiac Imaging: Correlations with Regional Left Ventricular Dysfunction and Contractile Reserve 108
4.1. Introduction 108
4.2. Methods 109
4.2.1. Animal Model and Experimental Protocol 109

4.2.2. MI Surgery 110
4.2.3. MRI Protocol 110
4.2.4. Hemodynamic Measurements 111
4.2.5. Post-Mortem Histology 112
4.2.6. Image Analysis 113
4.2.7. 3D Reconstruction in Continuity – 3D Kinesis Analysis 113
4.2.8. MRI Determination of LV Mass and LV Ejection Fraction 115
4.2.9. 3D Reconstruction in Continuity – Regional Surface Area Change Analysis 116
4.2.10. Regional Variability of Contraction 116
4.2.11. MRI Determination of Myocardial Infarction Size 118
4.2.12. Statistical Data Analysis 119
4.3. Results 119
4.3.1. Validation of MRI-Derived LV Mass and Infarct Size 119
4.3.2. Quantification of Regional Myocardial Dysfunction 120
4.3.3. Hemodynamics 122
4.4. Discussion 124
4.4.1. Territory of Regional Dysfunction in Mouse Model of Myocardial Infarction 125
4.4.2. Chronic MI Model 126
4.4.3. Inotropic Reserve and LGE MI Size 128
4.4.4. Limitations 129
4.5. Conclusions 129
4.6. Acknowledgements 130
4.7. References 131

Chapter 5. Conclusion to the Dissertation 135

LIST OF ABBREVIATIONS

DT-MRI or DTI ..... Diffusion Tensor MRI

MLC ..... Myosin Light Chain

MLCK ..... MLC Kinase

MHC ..... Myosin Heavy Chain

APD ..... Action Potential Duration

Ito ..... Transient Outward Potassium Current

Kcnk2 ..... Potassium Channel Subfamily K, Member 2

TREK-1 ..... 2-Pore Domain Potassium Channel TWIK-Related K+

Cx43 ..... Connexin 43

SERCA2a ..... Sarco-/Endoplasmic Reticulum Calcium ATPase Pump

POH ..... Pressure Overload Hypertrophy

ENDO ..... Sub-endocardium

MID ..... Midwall

EPI ..... Sub-epicardium

FA ..... Fractional Anisotropy

TAC ..... Transverse Aortic Constriction

WGA ..... Wheat Germ Agglutinin

MD ..... Mean Diffusivity

CL ..... Linear Anisotropy

CP ..... Planar Anisotropy

CS ..... Spherical Anisotropy

MFA ..... Myocyte Fractional Anisotropy

HW/BW ..... Heart-Weight to Body-Weight Ratio

MI ..... Myocardial Infarction

LGE ..... Late Gadolinium Enhancement

LAD ..... Left Anterior Descending Coronary Artery

TTC ..... 2,3,5-Triphenyltetrazolium Chloride

ED ..... End-Diastolic

ES ..... End-Systolic

3DK ..... 3D Kinesis

RSAC ..... Regional Surface Area Change

PLB ..... Phospholamban

PMCA ..... Plasma Membrane Calcium ATPase

NCX ..... Sodium-Calcium Exchanger

GAPDH ..... Glyceraldehyde 3-Phosphate Dehydrogenase

LIST OF FIGURES

Figure 1.1: Summary of transmural gradients 26

Figure 2.1: Regional dissection of the ventricles 53

Figure 2.2: Representative western blot 55

Figure 2.3: Regional variation of Cx43 58

Figure 2.4: Regional distribution of SERCA2a 59

Figure 2.5: Regional distribution of PLB 60

Figure 2.6: Regional distributions of NCX 61

Figure 2.7: Representative cross-sectional image of Cx43 immunofluorescent staining 62

Figure 2.8: Representative cross-sectional image of SERCA2a immunofluorescent staining 62

Figure 3.1: DT-MRI of rat ventricles 73

Figure 3.2: Transmural gradients of DTI-derived parameters in the LV free wall 77

Figure 3.3: Regional variations in select DTI-derived parameters 80

Figure 3.4: Orthogonal views of a representative confocal image volume 86

Figure 3.5: Summary of measurements from histological sections 88

Figure 3.6: Correlations between DTI and histology 89

Figure 3.7 Regional distributions in additional DTI-derived parameters 94

Figure 4.1: Segmentation of MRI and TTC images 113

Figure 4.2: RSAC Algorithm 114

Figure 4.3: Representative serial parametric images of infarcted mouse heart 115

Figure 4.4: Verification of MRI segmentation 118

Figure 4.5: Time course of MI size 120

Figure 4.6: Correlations of MI size with area of dysfunction 121

Figure 4.7: Correlation of MI size with inotropic contractile reserve 123

Figure 4.8: Time course of MI zone nodes and correlation of 3DK and RSAC 125

LIST OF TABLES

Table 2.1: ANOVAs for regional and group variation in protein density 56

Table 3.1: Summary of echocardiographic data 79

Table 3.2: ANOVAs for DT-MRI parameter regional variation 85

Table 3.3: ANCOVAs for correlations between DT-MRI and histological measurement 85

Table 4.1: Summary of functional parameters from MRI 119

Table 4.2: Hemodynamic data 124

ACKNOWLEDGEMENTS

I would like to acknowledge and thank my primary advisors, Dr. Jeff Omens, Dr. Andrew McCulloch, and Dr. Larry Frank for their consistent feedback and advice. Their guidance not only improved the quality of my dissertation, but also helped me to become a more critical thinker and better scientist. Also, I am extremely grateful for the support and advice of Dr. Kirk Peterson, who supported me in multiple ways and provided extremely valuable additional research opportunities, and to Dr. Adam Engler for, along with the others, serving on my dissertation committee.

There were several others who helped and contributed in various ways to this work. I am especially grateful to Diane Huang for her help with animal handling, surgeries, anesthesia for MRI, echocardiographic imaging, hemodynamics studies, and more. I thank Jennifer Stowe for her experimental expertise and willingness to teach and learn together new techniques in microscopy, staining, western blotting, on top of ordering lab supplies and providing advice and encouragement with a realistic perspective. Other former and current members of the cardiac mechanics research group, including Kevin Vincent, Will Valdez, and Kate Herum, contributed technical expertise, guidance, and friendship and commiserated at times about the challenges and difficulties of completing a PhD.

I was fortunate to work with experienced researchers from other universities internationally. I am extremely grateful for the imaging expertise and willingness to share data by Irvin Teh and Jurgen Schneider and their colleagues, as well as the computational modeling work by Alex Lewalle and colleagues.

I had the opportunity to train and learn from several other students. Younouss Faye helped perform western blot analysis, and stain and image entire cross-sections of protein

distributions in rat ventricular tissue. Rachel Lucero and Melody Dong, as Amgen Scholars, did a significant amount of work in creating models of a normal and hypertrophied rat heart and performing a large number of western blot experiments.

Marcus Bobar was helpful in considering all possible optimizations to our left ventricle fitting approach and worked tirelessly to segment countless rings of myocardium from cardiac MR images, and he was always encouraging and complimentary. He also facilitated other opportunities for research collaboration and learning, and he was kind enough to share snacks when we were working long hours together.

I also want to acknowledge my parents, who have continually supported me in everything I've ever pursued, especially my education. I'm also grateful to my children, who greeted me with squeals and hugs whenever I came home and made my work more purposeful, which continually encouraged me to do my best work.

Most importantly, I again recognize the incredibly significant efforts of my wife Kimberly. She has consistently amazed me with how many responsibilities she is capable of managing, and how she does so with increasing patience, kindness, and love. She has encouraged and supported me through all 2,088 days of my PhD.

Chapter 1, in part, is a reformatted reprint of the material as it appears in Progress in Biophysics and Molecular Biology 2016. Carruth, E.D.; McCulloch, A.D.; Omens, J.H., "Transmural Gradients of Myocardial Structure and Mechanics: Implications for Fiber Stress and Strain in Pressure Overload", vol. 122. The dissertation author was the primary investigator and author of this paper.

Chapter 2 comprises an original document.

Chapter 3, in full, is in preparation to be submitted for publication. Carruth, E.D.; Teh, I.; Schneider, J.E.; McCulloch, A.D.; Omens, J.H.; Frank, L.R., "Regional Variations in Diffusion Tensor Anisotropy are Associated with Myocyte Remodeling in Left Ventricular Pressure Overload". The dissertation author was the primary investigator and author of this paper.

Chapter 4, in full, is in preparation to be submitted for publication. Chao, C.J.; Carruth, E.D.; Bobar, M.; Bradford, W.; Bussell, R.; Gu, Y.; Hoshijima, M.; Peterson, K.L., "Myocardial Infarction Sizing in the Mouse by 3D Multiplanar Reconstruction of Late Gadolinium Enhanced Magnetic Resonance Cardiac Imaging: Correlation with Regional Left Ventricular Dysfunction and Contractile Reserve". The dissertation author contributed equally as a primary co-author of this paper.

VITA

2012 Bachelor of Science, University of Utah

2012-2018 Graduate Student Researcher, University of California San Diego

2018 Doctor of Philosophy, University of California San Diego

PUBLICATIONS

A. Lewalle, S. Land, E. Carruth, L. R. Frank, P. Lamata, J. H. Omens, A. D. McCulloch, S. A. Niederer, and N. P. Smith, "Decreasing compensatory ability of concentric ventricular hypertrophy in aortic-banded rat hearts," Front. Physiol., vol. 9, no. FEB, 2018.

D. McClymont, I. Teh, E. Carruth, J. Omens, A. McCulloch, H. J. Whittington, P. Kohl, V. Grau, and J. E. Schneider, "Evaluation of non-Gaussian diffusion in cardiac MRI," Magn. Reson. Med., Sep. 2016.

E. D. Carruth, A. D. Mcculloch, and J. H. Omens, "Transmural gradients of myocardial structure and mechanics : Implications for fiber stress and strain in pressure overload," Prog. Biophys. Mol. Biol., vol. 122, no. 3, pp. 215–226, 2016.

J. G. Lichter, E. Carruth, C. Mitchell, A. S. Barth, T. Aiba, D. A. Kass, G. F. Tomaselli, J. H. Bridge, and F. B. Sachse, "Remodeling of the sarcomeric cytoskeleton in cardiac ventricular myocytes during heart failure and after cardiac resynchronization therapy," J. Mol. Cell. Cardiol., vol. 72, pp. 86–95, 2014.

C. R. Henak, E. D. Carruth, A. E. Anderson, M. D. Harris, B. J. Ellis, C. L. Peters, and J. A. Weiss, "Finite element predictions of cartilage contact mechanics in hips with retroverted acetabula," Osteoarthritis Cartilage, vol. 21, no. 10, pp. 1522–9, 2013.

B. C. Schwab, G. Seemann, R. A. Lasher, N. S. Torres, E. M. Wulfers, M. Arp, E. D. Carruth, J. H. B. Bridge, and F. B. Sachse, "Quantitative analysis of cardiac tissue including fibroblasts using three-dimensional confocal microscopy and image reconstruction: Towards a basis for electrophysiological modeling," IEEE Trans. Med. Imaging, vol. 32, no. 5, pp. 862–872, 2013.

D. P. Lackey, E. D. Carruth, R. A. Lasher, J. Boenisch, F. B. Sachse, and R. W. Hitchcock, "Three-dimensional modeling and quantitative analysis of gap junction distributions in cardiac tissue," Ann. Biomed. Eng., vol. 39, no. 11, pp. 2683–2694, 2011.

ABSTRACT OF THE DISSERTATION

Mechanical Effects of Regional Structural Remodeling in the Left Ventricle

by

Eric David Carruth

Doctor of Philosophy in Bioengineering with a Specialization in Multi-Scale Biology

University of California San Diego, 2018

Professor Jeffrey H. Omens, Chair
Professor Lawrence R. Frank, Co-Chair

Cardiovascular disease is the primary cause of death in the United States and presents a significant challenge for researchers and clinicians due to the complexity and non-uniformity of structure-function relationships in the heart. The largest of the four heart chambers, the left ventricle, must pump efficiently and adapt to changes in demand or blood

flow, which the normal heart does remarkably well. However, in disease states, the compensatory response of the myocardium and persistent overloading can cause remodeling to become counter-productive.

Two of the major diseases contributing to overall cardiac morbidity and mortality are hypertension and myocardial infarction. While much is understood about the forms of remodeling and the associated dysfunction that occur in these disease states, they are usually measured at the scale of the entire organ (e.g. ejection fraction), or only in a select region of tissue. Many studies have shown regional variations in structural properties in the normal heart, but a comprehensive understanding of regional remodeling and the resultant functional consequences in disease states is lacking. Thus, the primary aims of this dissertation are to:

1. Determine the effect of pressure overload on regional distributions of electrophysiological and calcium handling proteins in the rat left ventricle.
2. Test the hypothesis that regional gradients in structural properties such as myocyte geometry are diminished in pressure overload.
    a. Determine whether regional variations in these structural features could be comprehensively and non-invasively quantified using DT-MRI.
3. Compare the measured size of a scar after myocardial infarction using traditional methods to the size of the corresponding region of dysfunction using a novel 3D MRI-based approach.

A better understanding of regional variations in normal and diseased ventricles will be valuable in identifying potential targets for therapeutic intervention to slow, prevent, or reverse adverse remodeling in patients with cardiac diseases such as hypertension or

infarction, and provide insight as to the mechanisms by which regional variations contribute to overall pump function.

1. Transmural Gradients of Myocardial Structure and Mechanics: Implications for Fiber Stress and Strain in Pressure Overload

The heart is a vital organ, supplying life-sustaining oxygen- and nutrient-rich blood to the entire organism, as well as removing cell waste and carbon dioxide. This is achieved by a cyclical pumping motion of the atria and ventricles, which beat approximately 100,000 times per day, 40 million times per year, or roughly 3 billion times in the lifetime of an average human. To achieve such longevity and performance, the structural composition of the heart at each spatial scale, from the subcellular sarcomere units to the entire organ, must be extremely well optimized for efficiency in its singular role to pump blood. Incredibly, the heart is also capable of adaptation to variations in blood pressure and flow, oxygen demand, or other external stimuli, allowing for large changes, acutely or chronically, in heart rate, developed pressure, and even myocyte geometry to compensate for variations in environmental properties, e.g. demand or downstream resistance.

Because of the high demands placed on the heart and its vital importance to maintaining life, perhaps it is not surprising that diseases of the heart and cardiovascular system continue to be the primary cause of death in the United States [1]. This fact, together with the aging of the population, indicates that it is imperative to better understand the diseases of the heart, specifically the structural and functional changes that occur during disease, as well as the mechanisms by which those changes occur. Such an understanding will enable clinicians to better treat those with cardiovascular disease to improve function and quality of life, as well as provide opportunities to improve preventive care, especially for younger generations.

To those who have studied the tissue structures of the heart in detail, it becomes obvious that the myocardium is spatially non-uniform. Many have studied these spatial heterogeneities and have concluded that such regional variations are necessary to allow for the highly efficient pumping action of the heart. However, it is unclear what role these regional variations in structural features play in the progression of common diseases of the ventricle.

It is with these considerations in mind that I, with the aid of many others, undertook to investigate the structural and functional changes that occur in animal models of two of the most common diseases in the left ventricle: pressure overload hypertrophy and myocardial infarction.

1.1. Introduction to Regional Gradients

The motion of the ventricular walls during normal cardiac pump function is highly complex, involving the coordinated activation and contraction of electromechanically coupled myocytes, followed by relaxation, and refilling. Despite numerous studies attempting to describe and model cardiac biomechanics, significant gaps of knowledge remain regarding the mechanisms by which cross-bridge force generation and sarcomere shortening are integrated by the hierarchical intracellular and extracellular organization of the myocardium and the anatomy of the chambers to produce the driving pressures for blood flow through pulmonary and systemic circulations. These gaps in knowledge represent potential opportunities for generating therapies or treatments for widespread cardiac disease, which remains the primary cause of death in the United States [1]. Hence, it remains of central importance to study the structure-function relationships that determine myocardial mechanics in the normal and diseased ventricles.

Much work has been done to quantify the three-dimensional deformation patterns in the normal left ventricle (LV) by tracking myocardial tissue during relaxation and filling (diastole), as well as during contraction and ejection (systole). Likewise, efforts have been made to characterize the internal tissue forces (stresses), with experimental measurements and mathematical or computational models. These studies have brought to light the complexity of normal cardiac mechanics, including insights regarding the mechanisms by which shortening along the axis of the myocytes drives circumferential and longitudinal shortening in the tissue, with concordant wall (radial) thickening and chamber torsion, to efficiently eject blood during systole, as well as the reverse process during diastole.

One notable feature that has been described is the surprisingly homogeneous transmural distribution of fiber strain and stress across the wall of the normal LV in several mammalian species, including humans. Because simple mechanical theory of thick-walled pressure vessels predicts transmural gradients of strain and stress, with higher levels in the subendocardium, researchers have sought to understand how this uniformity (which is an optimal design principle in engineering) is achieved in the normal heart. Studies have shown many structural and functional features of normal LV myocardium that have transmural gradients, that may contribute to maintaining uniformity of fiber stress and strain during LV ejection and filling. Alterations in these structure-function relationships could contribute to adverse remodeling and ventricular dysfunction in heart disease, particularly in load-mediated remodeling processes such as cardiac hypertrophy.

In this chapter, we review studies of transmural gradients of myocardial structure, and how variations in regional architecture affect transmural distributions of strains and stresses in the myocardium. In particular, we aim to summarize the mechanisms by which the structural

features that exhibit a transmural gradient may contribute to uniformity of fiber strain and stress, and how these distributions may change during disease. During remodeling processes in which mechano-sensing and mechano-transduction are important, understanding mechanisms that regulate the distributions of stress and strain will help define interventions aimed at altering the course of detrimental myocardial remodeling. We focus on examples related to mechanical regulation of concentric hypertrophy due to pressure overload, noting the high prevalence of hypertension, with one in three adults in the U.S. alone having high blood pressure [1].

1.2. Fiber Strain and Stress

1.2.1. Fiber Strain

While metrics of whole heart function such as ejection fraction, cardiac output, or wall thickening are informative and useful, especially for clinical classification of patients, the measurement of intra-myocardial deformation within the ventricle wall is imperative to fully understand regional mechanical function in myocardial tissue, and how load/deformation-related mechanisms of remodeling could be affected by regional variations in mechanics. Since consistent anatomic material landmarks are not readily detected in myocardial tissue, specialized techniques for imaging and recording the displacement of material points within the myocardium have been developed and used to quantify mechanical strain.

The measurement of strain within the ventricle walls has been achieved for decades using various techniques. In general, direct measurement of mechanical strain requires tracking of material points/markers in the tissue. Early, invasive studies involved the implantation of strain gauges, needles, radiopaque beads, ultrasonic crystals, or other markers whose positions were tracked in time [2]–[28]. Non-invasive methods have become more

available in animal models and humans, such as speckle tracking echocardiography [29], strain rate magnetic resonance imaging (MRI) [30], and tagged MRI [31]–[40]. MRI tagging is a technique whereby regions of myocardium are "tagged" with patterns of magnetization for a limited time as they deform through the cardiac cycle, thus enabling tracking of material point locations and strain calculations. The advantages of using tagged MRI include its non-invasiveness, relative ease of use, and comprehensive coverage of the ventricles at relatively high resolution. Difficulties include potentially low signal to noise ratio and the challenge of converting data from 2D tagged images to 3D displacements, which has been addressed in various ways [31], [34], [40]–[42]. Despite these few challenges, tagged MRI with harmonic phase material point tracking is one of the best methods for a full 3D description of tissue deformation [34], [43].

To completely describe three-dimensional deformation in a given volume, the six unique components of the strain tensor are necessary, which can be defined with respect to any chosen coordinate system. Some natural reference frame options which have been used in the heart include "cardiac coordinates", which locally correspond with circumferential, longitudinal, and radial directions of cylindrical or prolate spheroidal systems, "fiber coordinates", in which the circumferential direction from cardiac coordinates is rotated by the fiber angle to align with the local myofiber direction resulting in fiber, cross-fiber, and radial directions [27], and "material coordinates", which align with local fiber, sheet, and sheet-normal directions [6]. The latter two systems allow for quantifying strain aligned with the fiber axis, which is parallel to the long axis of the myocytes, and therefore the direction along which sarcomeres shorten during systolic contraction.

The strain tensor describes shape change between two time points or states. Fiber strain measured with respect to the unloaded state in passively loaded isolated arrested hearts or measured in vivo at end-diastole, with respect to early diastasis, has been used to investigate resting tissue mechanics. End-systolic fiber strain in vivo, usually referenced to end-diastole, characterizes the regional systolic mechanics of the myocardium. Using the above-mentioned techniques, researchers have sought to characterize fiber strains in the LV at end-diastole and end-systole to better understand how fiber mechanics relate to pump function and remodeling.

End-diastolic fiber strain

End-diastolic fiber strain gives insight into the passive material properties of myocardium, and describes the state of the sarcomeres at the moment of electrical activation. McCulloch et al. [17] used radiopaque markers and biplane radiography to measure epicardial end-diastolic strains with respect to an unloaded state (i.e. LV pressure ≈0) in dog and found that epicardial stretch during passive loading is greatest along the axis of the fibers. The same authors in a subsequent study suggested that the consequent torsional shear strain may serve to minimize transmural gradients of fiber lengthening during filling [44].

Omens et al. [21] measured transmural end-diastolic strains with respect to an unloaded state in the canine left ventricle. A major finding of that study, that corresponded well with previous studies of systolic strain [26], [27], was that the end-diastolic principal strain axis did not vary nearly as much with the wall depth as the fiber orientations, and increased in magnitude toward the endocardium. Given the gradient in the orientations of the myofibers across the wall, this result indicated that the maximum principal end-diastolic strain aligned closely with the subepicardial fibers, but was roughly orthogonal to the

subendocardial fibers, such that the subepicardial fiber orientation was the axis of maximum passive lengthening, but the subendocardial fibers were aligned with the axis of minimum in-plane strain. To examine this more directly, they used measured myofiber orientations in the tissues at the regions of the markers to resolve the strains with respect to fiber, cross-fiber and radial axes. They found that fiber strain at end-diastole is strikingly uniform across the wall, whereas the radial and cross-fiber strain components displayed transmural gradients [21] with significantly higher magnitudes on the endocardium than epicardium. This uniformity of fiber strain at end-diastole has also been shown in other in-vivo studies including the rat [22] and dog [45]. End-diastolic fiber strain measured in these studies ranged from 0.05 to 0.15 at pressures of ~1.0 kPa up to ~0.2 at 2.4 kPa.

As early as 1982, mathematical models of the left ventricle were used to test how transmural fiber angle variations and ventricular torsion affect transmural strain (and stress) distributions [46]. Simplified geometric models of the LV with spherical, cylindrical, and prolate spheroidal geometries, and anisotropy due to fiber orientation, have demonstrated uniformity in fiber strain across the wall at end-diastole with respect to an unloaded state [13], [47]–[49]. In agreement with the above experiments, end-diastolic strain values in these models were uniform and approximately 0.05-0.15 at 1.0 kPa filling pressure.

End-systolic fiber strain

Whereas measurements of fiber strains at end-diastole are necessary to describe myocardial passive mechanics, distributions of fiber strain at end-systole are key to understanding systolic pumping mechanics. Fenton et al. [11] were among the first to measure transmural systolic strain distributions using implanted radiopaque beads as material markers. They did not measure fiber orientations, but their results suggested mostly uniform end-

systolic fiber deformation. Many experiments following this approach have carefully quantified transmural fiber strain, including those in which the fiber orientations across the wall were measured by histology in the same region of the systolic strain measurement in dog and sheep LV [3]–[6], [27], [45]. In every case, fiber strains at end-systole with respect to end-diastole were found to be quite uniform transmurally, with values typically around -0.1 (i.e. about 10% fiber shortening) in each case in open-chest anesthetized animals.

Biplane radiography of implanted radiopaque markers is quite invasive, and therefore not typically feasible in humans, though it has been done in donor hearts received by heart transplant recipients [28]. A more feasible, non-invasive approach to regional strain recording in-vivo was developed using cardiac MRI [33], [35]. Experiments using these non-invasive approaches, including MRI tagging for material point tracking, have found that transmural fiber strain is uniform at end-systole with respect to end-diastole in several animal species and humans [36], [38]. The values of these measured end-systolic fiber strains are typically in the range of -0.1 to -0.2, corresponding to a uniform fiber shortening of about 10-20%.

Several models were developed to aid in the description of fiber strains during active contraction of the myocardium (systole), most often at end-systole, with end-diastole or an unloaded configuration as the reference phase. Early models, using a cylindrical shape for the LV, showed that fiber strain was uniform at end-systole [2]. This result was confirmed by modeling multiple fiber angle distributions in an ellipsoidal model [50], in a more realistic geometry of dog LV [13], and by iterative optimization of the fiber angle, which matched previously published measurements [51], [52].

A major result that surfaced from these models of myocardial mechanics is that anisotropy, fiber orientations, and the resultant torsion are key elements of myocardial

structure in the development of homogeneous fiber strain distributions across the wall. The myocardium is stiffer in the fiber direction than in the cross-fiber direction, and the direction of torsion is the same at both the epicardium and endocardium. Since torsion is essentially a shear in the circumferential-longitudinal plane, in which the fibers lie, it acts to increase the stretch of epicardial fibers during filling. Conversely the same torsion on endocardial fibers reduces fiber stretch during diastole. During systole these mechanisms are reversed, increasing fiber shortening in the subepicardium and decreasing it in the subendocardium. These important features will be discussed in greater detail in section 1.3 below.

With these key mechanisms accounted for, the consistent result of these experiments and mathematical models has been that fiber strain at end-systole is transmurally uniform, at a value of approximately -0.10 to -0.20, corresponding to about 10-20% fiber-aligned segment shortening from end-diastole.

1.2.2. Fiber Stress

The direct experimental measurement of stress within the myocardium is extremely challenging, especially while preserving native tissue structure and function, although some groups have attempted to implant stress sensors to achieve this, with limited success [53]–[55]. However, the development of computational tools such as finite element modeling, and the measurement and optimization of tissue material properties ex vivo [56]–[60] provide probably the best approach to estimate regional and 3D stresses given a set of reliable strains [61], [62]. A large number of such models have been developed to better understand regional cardiac mechanics [63].

End-diastolic fiber stress

Early models of end-diastolic stress distributions by Beyar and Sideman report circumferential stress rather than fiber stress, but do note that allowing torsion in their prolate spheroidal model reduced the heterogeneity of wall stress at end-diastole [64], [65]. Understanding true fiber stress, however, requires measurement of fiber orientations across the wall. One of the first modeling studies that reported end-diastolic fiber stress in models of rat and dog LVs under passive inflation showed relatively uniform fiber stresses, especially in the rat (~1 kPa), but less so in dog (2-9 kPa) [22]. Other models of end-diastole confirmed transmural uniformity of fiber stress in cylindrical models with papillary muscles and valves [66], radially symmetric canine LV geometry [13], and prolate spheroids of varying sphericity [47], though still others reported a less uniform distribution in spherical, cylindrical, and prolate geometries [48], [49]. The reported fiber stresses were approximately 1.9-2.5 kPa at a filling pressure of 1.0 kPa. In general, the stress distributions follow strain distributions, but several factors and mechanisms can alter this relationship as described in more detail below.

End-systolic fiber stress

As early as 1970, models were developed to quantify stresses at end-systole based on the measured distribution of fiber angles in the LV [67]. In this model, it was assumed that fiber stresses during systole were uniform across the wall (~20 kPa), then circumferential and longitudinal stresses were compared with those obtained from direct measurement, which agreed closely. Subsequently, models wherein fiber stress and strain were calculated found strong uniformity in end-systolic (and end-diastolic) fiber stresses and strains across the wall, as long as appropriate physiological fiber orientations were included [50], [66], [68]. A model with a more realistic geometry (though still radially symmetric), found strong uniformity of end-systolic fiber stress in the equatorial region, but a more heterogeneous distribution near

the base and apex [13]. In this model and others, end-diastolic and end-systolic in-plane (i.e. circumferential and longitudinal) strains matched measured data, but out of plane strain components (i.e. radial) generally did not. Modeling the myocardium as orthotropic, i.e. material properties corresponding to both fiber orientation and the laminar sheets of tightly coupled muscle fibers, with these sheets oriented roughly perpendicular to ventricular wall [69], improved the estimation of these out of plane strain components, but they still did not match directly measured strains [70]. Even recent computational models still cannot accurately predict all deformation and strain tensor patterns, even if bimodal sheet populations, which have been observed in animal studies [71], and whose supposed function has been modeled [72], are included (see e.g. [73]). This indicates a lack of understanding of the mechanical contribution of sheet structures to material strains. Despite difficulty in predicting radial strains due to the complexity of myocardial structure and contractile function, the majority consensus from these modeling studies has been that fiber stress at end-diastole and end-systole is transmurally uniform.

1.2.3. Mechanisms of Uniform Fiber Stress and Strain

Overall, a consistent result from experiments and models is that fiber strain and stress are quite uniform transmurally both at end-diastole and at end-systole in the normal left ventricle. It is worth appreciating that classical engineering analyses of uniform thick-walled pressure vessels predict high stresses and strains on the inner surface [74], [75], with large transmural gradients. This is a natural consequence of deformation of an incompressible, homogeneous, thick-walled chamber under an internal pressure load. The endocardial circumference must increase more than the epicardial circumference during filling, and decrease more than the epicardial circumference during ejection, resulting in large transmural

gradients of stress and strain. Thus, in both phases of the cardiac cycle, the circumferential filling (diastolic) and ejection (systolic) strains are higher on the endocardium, and experimental measurements consistently show this behavior. How then, can fiber strain (and stress) be uniform, especially since similar arguments can be made for longitudinal strain distributions?

The mechanisms leading to transmural uniformity of fiber stress and strain likely depend on specific transmural non-homogeneities in the myocardium. As mentioned previously and prominent among these is the fiber direction, which, along with chamber torsion, tends to normalize mechanical gradients. This has led several groups to propose that transmural uniformity of myocardial fiber stress and strain, and hence of regional myocardial work, is an important homeostatic principle of myocardial mechanics. It has been postulated that this uniformity may help maximize the efficiency with which regional contractile work is converted to pumping function and minimize vulnerability to ischemia or injury in systole [21], [44], [76]. All else being equal, this idea implies that there must exist one or more transmural gradient in tissue properties, architecture, or cellular characteristics that normalizes fiber stress and strain across the ventricle wall. In reality, several such transmural gradients have been observed that may explain this phenomenon. Here, we discuss measured transmural gradients from the literature, and how they may contribute to uniform fiber stress and strain. We also discuss effects of changes in these distributions during cardiac disease, with a focus on compensated concentric hypertrophy due to pressure overload.

1.3. Transmural Gradients as Mechanisms of Uniform Fiber Stress and Strain

1.3.1. Fiber Angle and Torsion

As previously mentioned, one of the most intriguing aspects of normal left ventricular function that has been observed for centuries is torsion or twist during the cardiac cycle. In the 17th century, Lower [77] described this phenomenon during systole as the "wringing of a linen cloth to squeeze out the water", and it has since been well characterized [78]. During isovolumic contraction, the ventricle rotates counterclockwise when viewed from the apex [79]. During ejection, the base changes directions, rotating clockwise, while the apex continues its counterclockwise rotation. Studies have also shown that the heart untwists rapidly during early relaxation independent of any contractile activity [3], [80], [81]. Many studies have measured torsion using various techniques, with spatial modulation of magnetization tagged cardiac MRI being the gold standard, and speckle tracking echocardiography as a relatively new and potentially valuable clinical approach [82]. Interestingly, a transmural gradient of torsion appears to exist, with endocardial rotations being greater at apex, mid, and basal levels than epicardial rotation [33], [39], [83], [84].

The muscle fiber architecture in the mammalian left ventricle is the fundamental cause of torsion. Since the histological studies of Streeter and colleagues in the 1960s [85] it has been appreciated that the orientation of myofibers in the left ventricle changes gradually from a left-handed helix with a pitch of 50-80 degrees on the epicardium, to a right-handed helix with a pitch of 60-90 degrees on the endocardium, with a smooth, nearly monotonic variation in between. Subsequent studies have verified this fiber architecture, and many have shown that it can be detected via Diffusion Tensor Magnetic Resonance Imaging (DT-MRI) [86]–[88].

Of the reports mentioned previously, several models were employed to understand the influence of fiber angle distribution on LV mechanics. It was found that stresses and strains were highly sensitive to the fiber orientation distribution [50]–[52], [89], [90]. It has also recently been proposed that torsion may be important in stress sensing, which may help to protect the heart from injury due to excessive stresses [91].

Because of the thick-walled shape of the left ventricle, the epicardial tissues have a larger radius from the LV center, and thus a greater lever arm during contraction-induced torsion. If all the fibers across the wall were aligned with the same helical pitch, then this contractile force in the epicardium would obviously necessitate more shortening in the endocardium. However, because the helical pitches are opposite (approximately 120° separation) from epicardium to endocardium, shortening of the epicardium and its resultant torsion result in shortening in the cross-fiber direction in the endocardium. This allows the sarcomeres in the endocardial fiber direction to contract relatively independently from (orthogonal to) those of the subepicardium.

It is apparent that the transmural fiber orientation gradient in normal hearts is important in dictating normal torsion and in normalizing fiber stress and strain across the wall. Perturbations to this fiber architecture could contribute substantially to altered cardiac function. Several studies have sought to determine if fiber orientations change during disease. An early study showed a decrease in fiber inclination angle only in the subendocardium in eccentric and concentric hypertrophy, though less so in concentric [92]. However, a later study reported more longitudinal fibers in pressure overload (concentric) hypertrophy and no change in exercise or volume overload (eccentric) hypertrophy [93]. Omens, et al. later found no difference in fiber angle in pressure overloaded rat hearts [94], [95]. However, fiber

orientations were measured in mice with left ventricular hypertrophy using DT-MRI, and slight but statistically significant differences in helix and inclination angles were found in the free wall and septum [96]. Also, the fiber orientation and dispersion in the right ventricle changed with pulmonary artery constriction [97].

For the most part, it appears that pressure overload hypertrophy minimally affects fiber angle distributions in the LV, though some small changes may occur. Together with the high level of conservation of this pattern in mammalian hearts, this fact suggests that the native fiber orientation is highly important and needs to be preserved in order to maintain normal cardiac function.

1.3.2. Material Anisotropy

Material anisotropy in most biological tissues is a direct determinant of local mechanical function. Myocardium is no different as it has a distinct fiber architecture, as well as laminar sheets that create a mechanically and electrically orthotropic material wherein fiber, sheet, and sheet-normal directions and function can be defined at any location in the ventricle wall [69], [70], [98]–[100]. Early biomechanical and electrophysiological modeling studies assumed transverse isotropy, however, several invaluable biomechanics studies have shown that ventricular tissue is in fact orthotropic [56], [57], and these directional properties related to fiber and sheet architecture play a significant role in determining tissue stress and strain.

Biomechanical experiments by Humphrey and Yin showed that the anisotropy of myocardial tissue may vary as a function of wall depth [60], [101]. Novak, et al. [57] later demonstrated that while myocardial tissue anisotropy is qualitatively uniform (i.e. the form of anisotropy does not change) in the canine left ventricle, it is quantitatively different between

epicardium and mid-myocardium. Lin and Yin [102] also showed that the material properties of active myocardium are different than that of passive myocardium, and are of course anisotropic, with significant development of cross-fiber stresses during contracture. Most recently, Sommer, et al. have shown the orthotropic mechanical properties of human myocardium [103], [104].

Arts et al. [105] showed the importance of anisotropy in their early models of LV mechanics, but the significance of the orthotropic nature (i.e. the sheet structure) of the myocardium has surfaced more recently [4]–[6], [72], [106]–[112]. Since it is commonly argued that sheet structures contribute to wall thickening by allowing large shear deformations to occur [4], [6], the orientation, dispersion, and mechanical properties of these sheets are undoubtedly important factors contributing to fiber stress and strain. The conduction of the electrical signal along the sheets is faster than across them, so timing of contraction is also affected by sheet structures [113], which in turn also affects regional stresses and strains [114].

Pressure overload induces hypertrophic remodeling of the extracellular matrix (ECM) by fibrosis (increase in collagen content) and collagen remodeling by fibroblasts [115]–[118]. Since the ECM is a major load-bearing component of cardiac tissue, fibrosis directly affects passive tissue properties [119]–[122]. Additionally, disorder of sheet structures has been measured in hypertensive heart disease [123]. The implications of this reorganization of sheet structures combined with fibrosis, mechanical stiffening, and other forms of remodeling on tissue mechanics require further study. Nonetheless, collagen content and remodeling and fiber and sheet reorganization undoubtedly alter tissue anisotropy and the distribution of fiber stresses and strains.

1.3.3. Residual Stress

Another potential mechanism contributing to uniform fiber stress and strain is that ventricular tissue is residually stressed (i.e. the unloaded, resting ventricle has internal stresses) and that the observed residual stress is non-uniform transmurally. Omens and Fung [124] first examined residual stress and strain in the rat LV following similar approaches used in other tissues, such as blood vessels [125]. Residual stress in cylindrical or spherical vessels is known to reduce stress concentrations at the inner surfaces, and this same mechanism is thought to occur in biological tissues. In the heart, it was found that making a radial cut in an equatorial cylindrical slice of rat left ventricle relieves circumferential residual stress, and results in an "opening angle" of approximately 45˚ [124]. This suggests that resting, unloaded ventricular tissue supports internal, residual stresses. It was shown that this residual stress is regionally variable as expected for the geometry of the ventricle, with endocardial residual stress being compressive, whereas epicardial residual stress is tensile. This work was later extended to show a linear transmural gradient in sarcomere length that becomes uniform when residual stress is released by a radial cut in the rat LV [126]. Similar results were observed in chick embryo [127] and dog [128]. Subsequent studies showed that 3D residual stress was even more complex with functional implications for distributions of normal and shear stresses during inflation [129].

Since normal, resting ventricular myocardium is residually stressed in this manner (with compressive stress in the subendocardium and tensile stress in the subepicardium), it is reasonable to postulate that fiber stress and strain are normalized by residual stress. Indeed, a cylindrical model showed that residual stress, together with anisotropy and torsion, normalize fiber stresses transmurally during filling [89]. Rodriguez et al. [126] commented that

Starling's law likely works in combination with shortening deactivation and force-velocity relationship effects to normalize fiber stresses during systole, and that end-diastolic sarcomere length is likely the primary factor that determines developed tension.

Residual stress has been shown to change in biological tissues due to external pressure overloads [130]. It was postulated that residual stress would increase under pressure overload hypertrophy [131]. Residual strain of the pressure overloaded left ventricle has been measured in rat [95] and chick embryo [132]. No significant difference in the opening angle was observed in rat, despite the reasonable hypothesis that it would increase with cell cross-sectional area [95]. Similarly, chick embryo opening angles did not change or even decreased [132]. Although residual stress has not clearly been shown to change with hypertrophic remodeling in the heart, residual stress does change in other cases such as extra-cellular matrix disease [133] and with normal cardiac growth [134]. With increased wall thickness without chamber dilation in pressure overload, residual stress is likely maintained in the tissue, indicating that the distribution of residual stress may be important for regulating fiber mechanics in both diastole and systole.

1.3.4. Protein Densities

In addition to tissue-scale properties that can modulate stress and strain gradients in the ventricles, molecular-scale distributions and gradients of structural and functional proteins in myocytes and ECM may contribute to uniformity of fiber stress and strain by modulating individual myocyte electromechanical functions, and the interplay between cells and the supporting ECM. Many of the reports summarized in the following sections describe heterogeneous protein distributions in the ventricles, with implications for active and passive function, as well and long-term remodeling in response to altered external loading conditions.

We review here several such proteins with transmural gradients that could affect fiber stress and strain distributions, mechanisms by which they might do so, and how disease-induced remodeling of those distributions may alter fiber stress and strain.

Passive structural proteins

Collagen

Collagen is a key structural component of the ECM and is therefore important in determining the passive mechanical properties of myocardial tissue [120], [135]. Collagen type I is predominant in the ventricles, and although its volume fraction is unchanged as a function of wall depth in rat LV, the form that collagen takes varies from subendocardium to subepicardium, in that the sheet structures mentioned above are clearly defined in the subendocardium and midwall, whereas toward the epicardium, collagen takes the form of longitudinal (parallel to the myocytes) cords [112]. This implies that the form and organization of collagen, rather than its content, may play a dominant role in terms of its transmural functional effects [136]. In **Figure 1.1**, collagen content is shown as uniform transmurally, with the implied understanding that the form is non-uniform.

Fibrosis is a well-documented remodeling response during pressure overload [115], [119], [137]–[139], and will certainly affect stress and strain distributions in this type of remodeling. Although the exact micromechanical-based contributions of ECM components and structure to the anisotropic passive material properties of myocardium in normal and fibrotic tissue are still mostly undefined, the form, distribution, and advanced glycation end-product mediated cross-linking of different types of collagen each can modulate cardiac stiffness [120]–[122], [140], [141]. Thus, it is reasonable to expect collagen/ECM remodeling

to modulate diastolic mechanics, possibly with regional variations due to the 3D laminar sheet architecture in the ventricular walls.

Titin isoform

Titin also represents a major component of passive mechanical properties in the cardiomyocytes. Two major isoforms, N2B and N2BA, are found in cardiac muscle. The shorter isoform, N2B, is stiffer than the larger N2BA isoform, and is predominant in human hearts [142]. Species-specific differences in the N2BA:N2B ratio exist, and it is thought that changes in this ratio modulate myocyte stiffness, where a higher ratio of N2BA:N2B corresponds with more compliant tissue, and vice versa [143]. Additionally, a transmural gradient of the N2BA:N2B ratio was observed in pig and canine hearts where a higher N2BA:N2B ratio exists in the subendocardium than in the subepicardium [80], [144]. Cazorla, et al. speculated that inter-species variations in cell-to-cell stiffness is related to strain normalization of myocytes in different regions of the ventricular walls [144]. This is consistent with the fact that the endocardial layer deforms more during a normal heart beat than the epicardium. The transmural gradient in the titin isoform ratio could suggest that stiffness along the fiber axis may also vary transmurally, leading to altered regional diastolic anisotropic material properties.

It has been shown that the N2BA:N2B ratio is decreased in spontaneously hypertensive rats [145], and in human patients with aortic stenosis [142], both of which are forms of pressure overload. In hearts that underwent two weeks of pacing tachycardia, the transmural gradient in titin ratios was exaggerated, and was postulated to contribute to a reduction in restoring forces after systolic contraction [80]. The changes to this isoform ratio in pressure overload need to be further examined, as well as the functional implications

postulated by the resultant changes in muscle stiffness. It is possible that this ratio is modulated to offset fibrotic stiffening during disease in order to maintain ventricular compliance and/or contractility.

Active sarcomere dynamics proteins

Myosin Regulatory Light Chain Phosphorylation

Myosin light chain (MLC) phosphorylation via myosin light chain kinase (MLCK) has been shown to increase the sensitivity of MLC to Ca2+, and is therefore a key determinant of tensile force produced in myofibers [146], [147]. Davis et al. observed a transmural gradient of phosphorylated regulatory light chain in normal mouse left ventricle, with increasing levels of phosphorylation from endocardium to epicardium [148]. They postulated that this gradient was required to facilitate normal LV torsion. Additionally, double mutant mice, in which MLC cannot be phosphorylated, had decreased performance and an eccentric hypertrophy phenotype with decreased LV torsion [149]. This study confirmed that MLC phosphorylation facilitates LV torsion, a key component of normalizing fiber stress and strain.

The latter study also proposed that phosphorylation of MLC is indispensable in regulating actin-myosin crossbridge dynamics and plays an important role in heart failure [149]. Toepfer, et al. also demonstrated that increased phosphorylation in rat trabeculae enhanced myocardial performance and suggested that decreased MLC-phosphorylation in cardiac disease is a key contributor to impaired cardiac contractile function [150]. MLC phosphorylation levels were significantly reduced in pressure overloaded and failing hearts [151], but heart failure was prevented in MLC kinase-overexpressing mice [152]. Additionally, constitutively phosphorylated cardiac MLC in mice was sufficient to prevent a hypertrophic cardiomyopathy phenotype [153], [154]. Conversely, knockout of MLC induced

heart failure [155]. These studies highlight the importance of MLC phosphorylation, including its transmural gradient, in the development of normal LV torsion and contraction, and a possible role in heart disease.

Myosin Heavy Chain Isoform

Myosin heavy chain (MHC) forms the head/neck region of the myosin crossbridge. Two major isoforms exist with different functionality. The α isoform (MHC- α) is faster and stronger but less energy-efficient than the β isoform (MHC-β). MHC-β is predominant in human hearts, whereas MHC-α is more highly expressed in rodents. Stones et al. measured a transmural gradient in MHC-β mRNA in rat LV, with more found in subendocardium than subepicardium [156]. No gradient in MHC-α was found in rat ventricular myocytes [157], but it has been shown in porcine hearts that greater expression in MHC-α isoform expression in the subepicardium contributes to differing mechanical function and timing, both of which may modify fiber stresses and strains [158]. Specifically, epicardial fibers were activated and developed force at higher rates than endocardial fibers. It is likely that the faster and supposedly stronger contraction of the MHC-α isoform will result in increased compressive stresses and strains in the fiber direction than that of the MHC-β isoform. This difference in the timing and rate of force production between epicardial and endocardial myocytes therefore is likely a major contributor to the distribution of fiber stresses and strains.

In small rodents, shifts in isoform expression toward MHC-β are associated with cardiac disease, including hypertrophy and failure [159]–[161]. This may suggest that cardiomyocytes attempt to improve their efficiency during increased workload demand, but some have reported that this shift may be maladaptive [160]. Regardless, even small changes

in MHC isoform levels during hypertrophic or other remodeling will likely contribute to altered LV functional mechanics by regulating the timing and force of contraction [159].

Electrophysiological proteins

I_{to} Proteins: KChIP/Kv4.2/Kv4.3

A well-known feature of myocardium is the difference in action potential duration (APD) across the wall, which, together with the activation sequence results in a positive QRS complex and a positive T-wave of the ECG [162]. This transmural gradient in APD is in part due to the transient outward potassium current (I_{to}). This current is comprised of contributions from Kv4.2, Kv4.3, and KChIP proteins. Interestingly, Kv4.2 but not Kv4.3 showed a transmural gradient in rat LV [163]. Similarly, there was only a slight gradient in Kv4.3 found in mouse, compared to more marked gradients in Kv4.2 and KChIP [164]. Canine and human LV showed no gradient in Kv4.3 but a significant gradient in KChIP [165], [166]. The KChIP and Kv4.2 expression patterns almost universally had higher levels in epicardium than endocardium. These gradients explain the observed phenomenon of differing APD across the wall [167].

The Kv4.2 protein is a subunit of voltage-gated potassium channel in cardiac myocytes, partially responsible for generating the Ito during the early plateau phase of the action potential, wherein Ca2+ ions are released and bind troponin C to initiate contraction. In rat, human, dog, and other mammals, Kv4.2 is denser in subepicardium than subendocardium. It is well known that endocardial cells are typically activated earlier than epicardial cells, and that the duration of the action potential in endocardial cells is longer than that of epicardial cells, so that they are repolarized after their epicardial counterparts. One of the potential reasons for this is the greater concentration of Kv4.2 in epicardial cells, which are responsible

for phase 1 early repolarization of the action potential in these cells. The early repolarization phase of the action potential is nearly nonexistent in subendocardial myocytes. This suggests that the endocardial myocytes are activated for a longer period of time than epicardial myocytes in the same heartbeat. Thus, the potential exists for more cross-bridges to be activated and to a greater extent. This would imply that higher strains (and stresses) may exist in the subendocardium due to this electrophysiology-based mechanism.

Wang et al. confirmed the native gradient in Kv4.2 in mice, and found that pressure overload reduced subepicardial Kv4.2 levels and current, eliminating the transmural gradient found in normal mice [168]. Thus, action potential-mediated myocyte function could play a role in hypertrophic remodeling.

Kcnk2 (TREK-1)

The potassium channel subfamily K, member 2 (Kcnk2), or 2-pore domain potassium channel TWIK-related K+ (TREK-1) has been extensively studied, and is thought to modulate the APD regionally and during sympathetic activation [169]. The TREK-1 gene, mRNA, and protein expression levels were greater in endocardial cells than epicardial cells [156], [170]–[172]. Interestingly, the gradient of this potassium channel is in the opposite direction to that of the Kv4.2 and KChIP channels, all of which contribute to repolarization, though with differing kinetics they are responsible for acting during different portions of the action potential [173], [174].

In hypertrophy, the levels of TREK-1 increased everywhere, such that the normal transmural gradient was maintained [172]. Similar to the discussion for the Ito proteins above, this protein's expression level is important in determining the sequence of activation and deactivation, and can thus impact regional stress and strain by impacting regional APD.

Connexins (Cx43)

Another important determinant of electrical conduction through cardiac muscle tissue is its anisotropy, which is dictated in part by the presence of gap junction channels, which primarily localize to the ends of the long, rod-shaped myocytes, reducing resistance to electrical conduction along the fiber direction. Connexin plaques are also found coupling adjacent cells, contributing to lateral propagation of activation [175]. The presence of the sheet structures makes this conduction orthotropic [113]. In ventricular myocytes, gap junctions are primarily formed by connexin-43 (Cx43). Yamada et al. found transmural gradients of Cx43 in the mouse LV, with a greater abundance in the subendocardium and mid-myocardium than subepicardium [176]. This pattern, however, was not observed in rat LV. A similar pattern to that in the mouse was seen in dog [177] and rabbit [178]. It is not straightforward to draw a connection between increased Cx43 expression and fiber strain, especially considering that expression may not necessarily influence conduction velocity per se. The use of finite element modeling of electromechanics in the ventricles with regionally variable fiber conduction would therefore be a useful study to help define the role of this transmural gradient for regional mechanical function.

Poelzing and Rosenbaum also showed that Cx43 expression is significantly reduced uniformly in dogs with heart failure, such that the gradient observed in normal dogs was preserved [179]. In humans with aortic stenosis, connexin-43 amounts increased during compensated hypertrophy, then decreased during decompensated hypertrophy [180]. An important feature of Cx43 remodeling during disease, including pressure overload and MI, is that of lateralization, which undoubtedly affects conduction anisotropy and velocity [180]–[183]. The effects of such remodeling on electromechanics require further study.

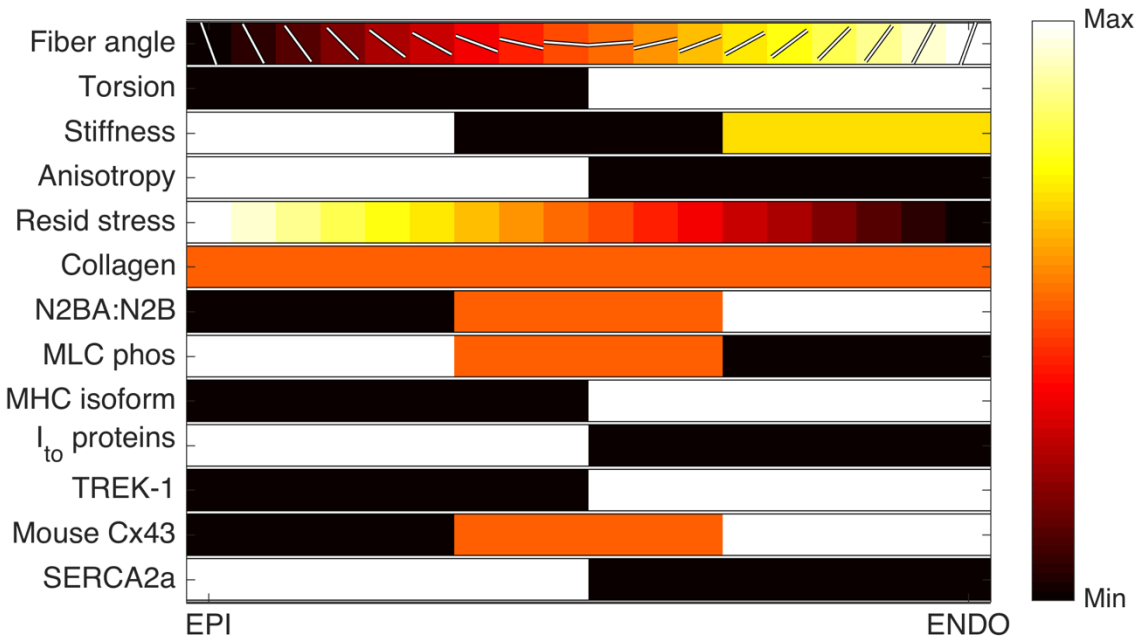

Figure 1.1. Summary of transmural gradients.

Calcium handling proteins

SERCA2a

The sarco-/endoplasmic reticulum calcium ATPase pump (SERCA2a) is a primary factor in removing Ca2+ ions from the cytosol following activation. Laurita et al. determined that more SERCA2a is expressed in the subepicardium than in the subendocardium in canine hearts, then showed using optical mapping how such differences may lead to altered activation patterns[184], [185]. Others confirmed this pattern in dog as well as both non-failing and failing human hearts [186]–[188]. However, this pattern was not observed in rat [189].

Cordeiro et al. also showed a difference in calcium transients in epi-, mid-, and endocardial cells from canine hearts [190]. Their results suggested that differences in calcium homeostasis regulate synchronization of ventricular contraction across the wall, despite

different electrical activation times. Computational models of these differences in Ca2+ dynamics within a finite element model of LV mechanics showed that this was not a factor in regulating end-systolic fiber strain, but that the effect of these gradients on fiber and cross-fiber strains in the LV is most apparent at early systole, rather than end-systole [191]. Even so, SERCA2a activity has been shown to affect contractility and relaxation in disease [192], [193], and changes in regional distributions may play a role in mechanical function of the myocardium.

In severe pressure overload, SERCA2a expression was decreased in the whole rat heart [194], [195]. This reduction in SERCA2a level was found to be nonhomogeneous throughout the LV [196], however the transmural pattern of SERCA2a decrease has not to our knowledge been reported.

1.4. Summary and Conclusion

A summary of transmural gradients described in this chapter is shown in **Figure 1.1.** Transmural uniformity of fiber stress and strain at end-diastole and end-systole appears to be a common finding from both experiments and mathematical models. Researchers have sought to understand the fundamental reasons for this homogeneity in function, postulating that uniform fiber stress and/or strain is likely important in improving ventricular pump efficiency. Several structural and functional factors in the normal myocardium that vary transmurally may be mechanisms contributing to the normalization of fiber stress and strain. In diseases such as pressure overload hypertrophy, several structural factors in myocytes and ECM may change, mediating the role of stress and strain in cardiac remodeling. The “holy grail” of work in this field would be to fully describe the contributions each transmural gradient to ventricular mechanics, and the mechanisms by which they do so. Computational modeling, in

conjunction with continued experimental measurements, constitute a challenging but tractable method to accomplish those goals.

1.5. Scope of the Dissertation

The objective of this dissertation is to characterize the 3D, regional variations in structural properties and the associated functional behavior in the left ventricle in two major cardiac diseases: hypertension (pressure overload) and myocardial infarction. Experimental data were combined with computer models of left ventricular geometry derived from magnetic resonance imaging to discover novel regionally varying structural features and regional dysfunction in these major diseases.

As described in Section 1.3.4 above, regional variations in protein densities affect regional mechanics and therefore left ventricular pump function. The first specific aim, therefore, is to determine the effect of pressure overload on regional distributions of electrophysiological and calcium handling proteins in the rat left ventricle. In this work, I showed novel significant regional gradients in protein densities and their redistribution in pressure overload. This information is valuable for generating computational models of ventricular mechanics and for identifying potential targets to reduce or reverse adverse remodeling in this prevalent disease.

The second aim is to test the hypothesis that regional gradients in structural properties such as myocyte geometry are diminished in pressure overload. A secondary goal of this aim was to determine whether regional variations in these structural features could be comprehensively and non-invasively quantified using diffusion tensor MRI. In Chapter 3, I show using confocal microscopy that a transmural gradient in myocyte geometry in normal hearts was reduced in pressure overload, and that diffusion tensor MRI is sensitive to

variations in structural features, regardless of whether those variations are due to regional heterogeneity or structural remodeling in pressure overload. This novel application of diffusion tensor MRI provides a faster, more comprehensive and non-invasive method to characterize tissue microstructure. Additionally, the measured regional variation in the remodeling response to hypertrophy is critical to understanding the functional effects of pressure overload and potential treatment options.

Many researchers rely on two-dimensional echocardiography to quantify globally the extent of injury during myocardial infarction and therefore the efficacy of a treatment. However, this two-dimensional, global approach is insufficient to capture the spatial complexity of regional, three-dimensional structural and functional deficits accurately. Therefore, the third aim is to compare the measured size of a scar after myocardial infarction using traditional methods to the size of the corresponding region of dysfunction using a novel 3D MRI-based approach. I show in Chapter 4 using this method that the region of dysfunction resulting from an infarction is significantly larger than the measured scar size, and this disparity increases with the duration of coronary blockage. This result indicates that a more comprehensive approach to understanding regional dysfunction in myocardial infarction is necessary and provides a straightforward method to do so.

Spatial heterogeneity is a key feature of left ventricular structures. Researchers and clinicians must appreciate this 3D heterogeneity in order to better understand the functional effects of regional remodeling during disease and develop treatments to address remodeling to improve patient outcomes.

1.6. Acknowledgements

Chapter 1, in part, is a reformatted reprint of the material as it appears in Progress in Biophysics and Molecular Biology 2016. Carruth, E.D.; McCulloch, A.D.; Omens, J.H., "Transmural Gradients of Myocardial Structure and Mechanics: Implications for Fiber Stress and Strain in Pressure Overload", vol. 122. The dissertation author was the primary investigator and author of this paper.

This work was supported by the National Institutes of Health grants HL103566 and GM094503.

1.7. References

[1] E. J. Benjamin, S. S. Virani, C. W. Callaway, A. R. Chang, S. Cheng, S. E. Chiuve, M. Cushman, F. N. Delling, R. Deo, S. D. de Ferranti, J. F. Ferguson, M. Fornage, C. Gillespie, C. R. Isasi, M. C. Jiménez, L. C. Jordan, S. E. Judd, D. Lackland, J. H. Lichtman, L. Lisabeth, S. Liu, C. T. Longenecker, P. L. Lutsey, D. B. Matchar, K. Matsushita, M. E. Mussolino, K. Nasir, M. O'Flaherty, L. P. Palaniappan, D. K. Pandey, M. J. Reeves, M. D. Ritchey, C. J. Rodriguez, G. A. Roth, W. D. Rosamond, U. K. A. Sampson, G. M. Satou, S. H. Shah, N. L. Spartano, D. L. Tirschwell, C. W. Tsao, J. H. Voeks, J. Z. Willey, J. T. Wilkins, J. H. Wu, H. M. Alger, S. S. Wong, and P. Muntner, "Heart Disease and Stroke Statistics—2018 Update: A Report From the American Heart Association," Circulation, p. CIR.0000000000000558, 2018.

[2] T. Arts and R. S. Reneman, "Measurement of deformation of canine epicardium in vivo during cardiac cycle.," Am. J. Physiol., vol. 239, no. 3, pp. H432-7, Sep. 1980.

[3] H. Ashikaga, J. C. Criscione, J. H. Omens, J. W. Covell, and N. B. Ingels, "Transmural left ventricular mechanics underlying torsional recoil during relaxation.," Am. J. Physiol. Heart Circ. Physiol., vol. 286, no. 2, pp. H640-7, 2004.

[4] A. Cheng, F. Langer, F. Rodriguez, J. C. Criscione, G. T. Daughters, D. C. Miller, and N. B. Ingels, "Transmural sheet strains in the lateral wall of the ovine left ventricle.," Am. J. Physiol. Heart Circ. Physiol., vol. 289, pp. H1234–H1241, 2005.

[5] A. Cheng, T. C. Nguyen, M. Malinowski, G. T. Daughters, D. C. Miller, and N. B. Ingels, "Heterogeneity of Left Ventricular Wall Thickening Mechanisms," Circulation, vol. 118, no. 7, pp. 713–721, 2008.

[6] K. D. Costa, Y. Takayama, A. D. McCulloch, and J. W. Covell, "Laminar fiber architecture and three-dimensional systolic mechanics in canine ventricular myocardium.," Am. J. Physiol., vol. 276, no. 2 Pt 2, pp. H595–H607, 1999.

[7] J. M. Dieudonné, "[Gradients of direction and principal deformations in the normal left ventricle wall].," J. Physiol. (Paris)., vol. 61, no. 4, pp. 305–30, Jan. .

[8] A. S. Douglas, E. K. Rodriguez, W. O'Dell, and W. C. Hunter, "Unique strain history during ejection in canine left ventricle.," Am. J. Physiol., vol. 260, no. 5 Pt 2, pp. H1596-611, 1991.

[9] K. Elshuraydeh, J. Smits, R. M. Heethaar, and J. J. Denier van der Gon, "Method for measuring cardiac dimensions and intramural deformations," J. Biomed. Eng., vol. 3, no. 1, pp. 49–52, Jan. 1981.

[10] I. Fann, E. Sarris, and D. Craig, “Regional epicardial and endocardial two-dimensional finite deformations in canine left ventricle,” Am. J. Physiol. Heart Circ. Physiol., vol. 261, pp. H1402–H1410, 1991.

[11] T. R. Fenton, J. M. Cherry, and G. A. Klassen, “Transmural myocardial deformation in the canine left ventricular wall,” Am J Physiol, vol. 235, no. 5, pp. H523-30, 1978.

[12] G. L. Freeman, M. M. LeWinter, R. L. Engler, and J. W. Covell, “Relationship between myocardial fiber direction and segment shortening in the midwall of the canine left ventricle.,” Circ. Res., vol. 56, no. 1, pp. 31–9, 1985.

[13] J. M. Guccione, K. D. Costa, and A. D. McCulloch, “Finite element stress analysis of left ventricular mechanics in the beating dog heart,” J. Biomech., vol. 28, no. 10, pp. 1167–1177, 1995.

[14] D. E. Hansen, G. T. Daughters, E. L. Alderman, N. B. Ingels, and D. C. Miller, “Torsional deformation of the left ventricular midwall in human hearts with intramyocardial markers: regional heterogeneity and sensitivity to the inotropic effects of abrupt rate changes.,” Circ. Res., vol. 62, no. 5, pp. 941–952, 1988.

[15] N. B. Ingels, G. T. Daughters, S. R. Davies, and I. B. Macdonald, “Stereo photogrammetric studies on the dynamic geometry of the canine left ventricular epicardium.,” J. Biomech., vol. 4, no. 6, pp. 541–50, Dec. 1971.

[16] M. M. LeWinter, R. S. Kent, J. M. Kroener, T. E. Carew, and J. W. Covell, “Regional differences in myocardial performance in the left ventricle of the dog.,” Circ Res, vol. 37, no. 2, pp. 191–199, 1975.

[17] A. D. McCulloch, B. H. Smaill, and P. J. Hunter, “Left ventricular epicardial deformation in isolated arrested dog heart.,” Am. J. Physiol., vol. 252, pp. H233–H241, 1987.

[18] A. D. McCulloch and J. H. Omens, “Non-homogeneous analysis of three-dimensional transmural finite deformation in canine ventricular myocardium,” J. Biomech., vol. 24, no. 7, pp. 539–548, 1991.

[19] G. D. Meier, M. C. Ziskin, W. P. Santamore, and a a Bove, “Kinematics of the beating heart.,” IEEE Trans. Biomed. Eng., vol. 27, no. 6, pp. 319–29, 1980.

[20] G. D. Meier, M. C. Ziskin, and A. A. Bove, “Helical fibers in myocardium of dogs change their pitch as they contract,” Am. J. Physiol., vol. 243, no. 1, p. 0, 1982.

[21] J. H. Omens, K. D. May, and a D. McCulloch, “Transmural distribution of three-dimensional strain in the isolated arrested canine left ventricle.,” Am. J. Physiol., vol. 261, no. 3 Pt 2, pp. H918–H928, 1991.

[22] J. H. Omens, D. A. MacKenna, and A. D. McCulloch, “Measurement of strain and analysis of stress in resting rat left ventricular myocardium.,” J. Biomech., vol. 26, no. 6, pp. 665–76, 1993.

[23] G. Osakada, S. Sasayama, C. Kawai, A. Hirakawa, W. S. Kemper, D. Franklin, and J. J. Ross, “The analysis of left ventricular wall thickness and shear by an ultrasonic triangulation technique in the dog,” Arch. Mikrosk. Anat., vol. 47, pp. 173–181, 1980.

[24] F. W. Prinzen, T. Arts, G. J. van der Vusse, and R. S. Reneman, “Fiber shortening in the inner layers of the left ventricular wall as assessed from epicardial deformation during normoxia and ischemia,” J. Biomech., vol. 17, no. 10, pp. 801–811, 1984.

[25] F. J. Villarreal and W. Y. Lew, “Finite strains in anterior and posterior wall of canine left ventricle,” Am. J. Physiol., vol. 259, no. 5 Pt 2, pp. H1409–H1418, 1990.

[26] L. K. Waldman, Y. C. Fung, and J. W. Covell, “Transmural myocardial deformation in the canine left ventricle. Normal in vivo three-dimensional finite strains.,” Circ. Res., vol. 57, no. 1, pp. 152–163, 1985.

[27] L. K. Waldman, D. Nosan, F. Villarreal, and J. W. Covell, “Relation between transmural deformation and local myofiber direction in canine left ventricle.,” Circ. Res., vol. 63, no. 3, pp. 550–562, 1988.

[28] K. L. Yun, M. A. Niczyporuk, G. T. Daughters, N. B. Ingels, E. B. Stinson, E. L. Alderman, D. E. Hansen, and D. C. Miller, “Alterations in left ventricular diastolic twist mechanics during acute human cardiac allograft rejection.,” Circulation, vol. 83, pp. 962–973, 1991.

[29] D. Bellavia, H. I. Michelena, M. Martinez, P. a Pellikka, C. J. Bruce, H. M. Connolly, H. R. Villarraga, G. Veress, J. K. Oh, and F. a Miller, “Speckle myocardial imaging modalities for early detection of myocardial impairment in isolated left ventricular non-compaction.,” Heart, vol. 96, no. 6, pp. 440–7, 2010.

[30] J. Dou, W. Y. I. Tseng, T. G. Reese, and V. J. Wedeen, “Combined diffusion and strain MRI reveals structure and function of human myocardial laminar sheets in vivo,” Magn. Reson. Med., vol. 50, no. 1, pp. 107–113, 2003.

[31] H. Azhari, J. L. Weiss, W. J. Rogers, C. O. Siu, E. a Zerhouni, and E. P. Shapiro, “Noninvasive quantification of principle strains in normal canine hearts using tagged MRI images in 3D,” Am. J. Physiol., vol. 264, no. 1 Pt 2, pp. H205-16, 1993.

[32] J. Bogaert and F. E. Rademakers, “Regional nonuniformity of normal adult human left ventricle.,” Am. J. Physiol. Heart Circ. Physiol., vol. 280, no. 2, pp. H610-20, 2001.

[33] M. B. Buchalter, J. L. Weiss, W. J. Rogers, E. a Zerhouni, M. L. Weisfeldt, R. Beyar, and E. P. Shapiro, "Noninvasive quantification of left ventricular rotational deformation in normal humans using magnetic resonance imaging myocardial tagging.," Circulation, vol. 81, no. 4, pp. 1236–1244, 1990.

[34] J. S. Chuang, A. Zemljic-Harpf, R. S. Ross, L. R. Frank, A. D. McCulloch, and J. H. Omens, "Determination of three-dimensional ventricular strain distributions in gene-targeted mice using tagged MRI," Magn. Reson. Med., vol. 64, no. 5, pp. 1281–1288, 2010.

[35] N. Clark, N. Reichek, P. Bergey, E. Hoffman, D. Brownson, L. Palmon, and L. Axel, "Circumferential myocardial shortening in the normal human left ventricle. Assessment by magnetic resonance imaging using spatial modulation of magnetization," Circulation, vol. 84, no. 1, pp. 67–74, 1991.

[36] G. A. MacGowan, E. P. Shapiro, H. Azhari, C. O. Siu, P. S. Hees, G. M. Hutchins, J. L. Weiss, and F. E. Rademakers, "Noninvasive Measurement of Shortening in the Fiber and Cross-Fiber Directions in the Normal Human Left Ventricle and in Idiopathic Dilated Cardiomyopathy," Circulation, vol. 96, no. 2, pp. 535–541, Jul. 1997.

[37] E. R. McVeigh and E. A. Zerhouni, "Noninvasive measurement of transmural gradients in myocardial strain with MR imaging.," Radiology, vol. 180, pp. 677–683, 1991.

[38] F. E. Rademakers, W. J. Rogers, W. H. Guier, G. M. Hutchins, C. O. Siu, M. L. Weisfeldt, J. L. Weiss, and E. P. Shapiro, "Relation of regional cross-fiber shortening to wall thickening in the intact heart. Three-dimensional strain analysis by NMR tagging," Circulation, vol. 89, no. 3, pp. 1174–1182, 1994.

[39] A. A. Young, H. Imai, C. N. Chang, and L. Axel, "Two-dimensional left ventricular deformation during systole using magnetic resonance imaging with spatial modulation of magnetization [published erratum appears in Circulation 1994 Sep;90(3):1584]," Circulation, vol. 89, no. 2, pp. 740–752, 1994.

[40] A. A. Young, C. M. Kramer, V. A. Ferrari, L. Axel, and N. Reichek, "Three-dimensional left ventricular deformation in hypertrophic cardiomyopathy.," Circulation, vol. 90, no. 2, pp. 854–867, 1994.

[41] E.-S. H. Ibrahim, "Myocardial tagging by cardiovascular magnetic resonance: evolution of techniques--pulse sequences, analysis algorithms, and applications.," J. Cardiovasc. Magn. Reson., vol. 13, no. 1, p. 36, 2011.

[42] J. Zhong, W. Liu, and X. Yu, “Characterization of three-dimensional myocardial deformation in the mouse heart: An MR tagging study,” J. Magn. Reson. Imaging, vol. 27, no. 6, pp. 1263–1270, 2008.

[43] N. F. Osman, W. S. Kerwin, E. R. McVeigh, and J. L. Prince, “Cardiac motion tracking using CINE harmonic phase (HARP) magnetic resonance imaging,” Magn. Reson. Med., vol. 42, no. 6, pp. 1048–1060, 1999.

[44] A. D. McCulloch, B. H. Smaill, and P. J. Hunter, “Regional left ventricular epicardial deformation in the passive dog heart.,” Circ. Res., vol. 64, no. 4, pp. 721–733, 1989.

[45] Y. Takayama, K. D. Costa, and J. W. Covell, “Contribution of laminar myofiber architecture to load-dependent changes in mechanics of LV myocardium.,” Am. J. Physiol. Heart Circ. Physiol., vol. 282, no. 4, pp. H1510-20, 2002.

[46] T. Arts, P. C. Veenstra, and R. S. Reneman, “Epicardial deformation and left ventricular wall mechanics during ejection in the dog.,” Am. J. Physiol., vol. 243, pp. H379–H390, 1982.

[47] H. F. Choi, J. D’hooge, F. E. Rademakers, and P. Claus, “Influence of left-ventricular shape on passive filling properties and end-diastolic fiber stress and strain,” J. Biomech., vol. 43, no. 9, pp. 1745–1753, 2010.

[48] K. D. Costa, P. J. Hunter, J. S. Wayne, L. K. Waldman, J. M. Guccione, and a D. McCulloch, “A three-dimensional finite element method for large elastic deformations of ventricular myocardium: Prolate spheroidal coordinates.,” J. Biomech. Eng., vol. 118, no. 4, pp. 464–472, 1996.

[49] K. D. Costa, P. J. Hunter, J. Rogers, J. M. Guccione, L. Waldman, and A. D. McCulloch, “A Three-Dimensional Finite Element Method for Large Elastic Deformations of Ventricular Myocardium: I - Cylindrical and Spherical Polar Coordinates,” J. Biomech. Eng., vol. 118, no. November 1996, p. 452, 1996.

[50] P. H. M. Bovendeerd, T. Arts, J. M. Huyghe, D. H. van Campen, and R. S. Reneman, “Dependence of local left ventricular wall mechanics on myocardial fiber orientation: A model study,” J. Biomech., vol. 25, no. 10, pp. 1129–1140, 1992.

[51] J. Rijcken, P. H. M. Bovendeerd, A. J. G. Schoofs, D. H. Van Campent, and T. Arts, “Optimization of cardiac fiber orientation for homogeneous fiber strain at beginning of ejection,” J. Biomech., vol. 30, no. 10, pp. 1041–1049, 1997.

[52] J. Rijcken, P. H. Bovendeerd, A. J. Schoofs, D. H. van Campen, and T. Arts, “Optimization of cardiac fiber orientation for homogeneous fiber strain during ejection.,” Ann. Biomed. Eng., vol. 27, no. 3, pp. 289–97, Jan. 1999.

[53] J. W. Burns, J. W. Covell, R. Myers, and J. Ross, “Comparison of Directly Measured Left Ventricular Wall Stress and Stress Calculated from Geometric Reference Figures,” Circ. Res., vol. 28, no. 6, pp. 611–621, 1971.

[54] E. O. Feigl, G. A. Simon, and D. L. Fry, “Auxotonic and isometric cardiac force transducers.,” J. Appl. Physiol., vol. 23, no. 4, pp. 597–600, 1967.

[55] P. A. McHale and J. C. Greenfield, “Evaluation of several geometric models for estimation of left ventricular circumferential wall stress,” Circ. Res., vol. 33, no. 3, pp. 303–312, 1973.

[56] S. Dokos, B. H. Smaill, A. a Young, and I. J. LeGrice, “Shear properties of passive ventricular myocardium.,” Am. J. Physiol. Heart Circ. Physiol., vol. 283, no. 6, pp. H2650–H2659, 2002.

[57] V. P. Novak, “Regional mechanical properties of passive myocardium,” J. Biomech., vol. 27, no. 4, pp. 403–412, 1994.

[58] J. D. Humphrey, R. K. Strumpf, and F. C. Yin, “Determination of a constitutive relation for passive myocardium: I. A new functional form.,” J. Biomech. Eng., vol. 112, no. 3, pp. 333–339, 1990.

[59] J. D. Humphrey, R. K. Strumpf, and F. C. Yin, “Determination of a constitutive relation for passive myocardium: II. Parameter Estimation,” J. Biomech. Eng., vol. 112, no. 3, pp. 333–339, 1990.

[60] F. C. P. Yin, R. K. Strumpf, P. H. Chew, and S. L. Zeger, “Quantification of the mechanical properties of noncontracting canine myocardium under simultaneous biaxial loading,” J. Biomech., vol. 20, no. 6, pp. 577–589, 1987.

[61] R. M. Huisman, G. Elzinga, N. Westerhof, and P. Sipkema, “Measurement of left ventricular wall stress.,” Cardiovasc. Res., vol. 14, no. 3, pp. 142–53, Mar. 1980.

[62] F. Yin, “Ventricular wall stress,” Circ. Res., vol. 49, no. 4, pp. 829–42, 1981.

[63] P. J. Hunter, A. J. Pullan, and B. H. Smaill, “Modeling total heart function.,” Annu. Rev. Biomed. Eng., vol. 5, pp. 147–77, 2003.

[64] R. Beyar and S. Sideman, “A computer study of the left ventricular performance based on fiber structure, sarcomere dynamics, and transmural electrical propagation velocity,” Circ. Res., vol. 55, no. 3, pp. 358–375, 1984.

[65] R. Beyar and S. Sideman, “The dynamic twisting of the left ventricle: A computer study,” Ann. Biomed. Eng., vol. 14, no. 6, pp. 547–562, 1986.

[66] T. Arts and R. S. Reneman, “Dynamics of left ventricular wall and mitral valve mechanics-A model study,” J. Biomech., vol. 22, no. 3, pp. 261–271, 1989.

[67] D. D. Streeter, R. N. Vaishnav, D. J. Patel, H. M. Spotnitz, J. Ross, and E. H. Sonnenblick, “Stress distribution in the canine left ventricle during diastole and systole.,” Biophys. J., vol. 10, no. 4, pp. 345–63, 1970.

[68] P. H. M. Bovendeerd, J. M. Huyghe, T. Arts, D. H. van Campen, and R. S. Reneman, “Influence of endocardial-epicardial crossover of muscle fibers on left ventricular wall mechanics,” J. Biomech., vol. 27, no. 7, pp. 941–951, 1994.

[69] I. J. LeGrice, B. H. Smaill, L. Z. Chai, S. G. Edgar, J. B. Gavin, and P. J. Hunter, “Laminar structure of the heart: ventricular myocyte arrangement and connective tissue architecture in the dog,” Am J Physiol, vol. 269, no. 2 Pt 2, pp. H571-82, 1995.

[70] T. P. Usyk, R. Mazhari, and A. D. Mcculloch, “Effect of laminar orthotropic myofiber architecture on regional stress and strain in the canine left ventricle,” J. Elast., vol. 61, no. 1–3, pp. 143–164, 2000.

[71] G. L. Kung, T. C. Nguyen, A. Itoh, S. Skare, N. B. Ingels, D. C. Miller, and D. B. Ennis, “The presence of two local myocardial sheet populations confirmed by diffusion tensor MRI and histological validation,” J. Magn. Reson. Imaging, vol. 34, no. 5, pp. 1080–1091, 2011.

[72] T. Arts, K. D. Costa, J. W. Covell, and a D. McCulloch, “Relating myocardial laminar architecture to shear strain and muscle fiber orientation.,” Am. J. Physiol. Heart Circ. Physiol., vol. 280, no. 5, pp. H2222–H2229, 2001.

[73] V. Carapella, R. Bordas, P. Pathmanathan, M. Lohezic, J. E. Schneider, P. Kohl, K. Burrage, and V. Grau, “Quantitative study of the effect of tissue microstructure on contraction in a computational model of rat left ventricle,” PLoS One, vol. 9, no. 4, pp. 1–12, 2014.

[74] H. Demiray, “Large deformation analysis of some basic problems in biophysics,” Bull. Math. Biol., vol. 38, no. 6, pp. 701–712, 1976.

[75] I. Mirsky, “Ventricular and arterial wall stresses based on large deformation analyses.,” Biophys. J., vol. 13, no. 11, pp. 1141–59, 1973.

[76] M. Vendelin, P. H. M. Bovendeerd, J. Engelbrecht, and T. Arts, “Optimizing ventricular fibers: uniform strain or stress, but not ATP consumption, leads to high efficiency.,” Am. J. Physiol. Heart Circ. Physiol., vol. 283, pp. H1072–H1081, 2002.

[77] R. Lower, Tractatus de corde: item de motu & colore sanguinis et chyli in cum transitu. Londini: Typis Jo. Redmayne impensis Jacobi Allestry, 1669.

[78] P. P. Sengupta, A. J. Tajik, K. Chandrasekaran, and B. K. Khandheria, “Twist Mechanics of the Left Ventricle,” JACC Cardiovasc. Imaging, vol. 1, no. 3, pp. 366–376, 2008.

[79] A. a Young and B. R. Cowan, “Evaluation of left ventricular torsion by cardiovascular magnetic resonance.,” J. Cardiovasc. Magn. Reson., vol. 14, p. 49, 2012.

[80] S. P. Bell, L. Nyland, M. D. Tischler, M. McNabb, H. Granzier, and M. M. LeWinter, “Alterations in the determinants of diastolic suction during pacing tachycardia.,” Circ. Res., vol. 87, no. 3, pp. 235–240, 2000.

[81] F. E. Rademakers, M. B. Buchalter, W. J. Rogers, E. A. Zerhouni, M. L. Weisfeldt, J. L. Weiss, and E. P. Shapiro, “Dissociation between left ventricular untwisting and filling. Accentuation by catecholamines.,” Circulation, vol. 85, no. 4, pp. 1572–81, 1992.

[82] I. K. Rüssel, M. J. W. Götte, J. G. Bronzwaer, P. Knaapen, W. J. Paulus, and A. C. van Rossum, “Left Ventricular Torsion. An Expanding Role in the Analysis of Myocardial Dysfunction,” JACC Cardiovasc. Imaging, vol. 2, no. 5, pp. 648–655, 2009.

[83] C. H. Lorenz, J. S. Pastorek, and J. M. Bundy, “Delineation of normal human left ventricular twist throughout systole by tagged cine magnetic resonance imaging.,” J. Cardiovasc. Magn. Reson., vol. 2, no. 2, pp. 97–108, Jan. 2000.

[84] E. a Zerhouni, D. M. Parish, W. J. Rogers, a Yang, and E. P. Shapiro, “Human heart: tagging with MR imaging--a method for noninvasive assessment of myocardial motion.,” Radiology, vol. 169, no. 1, pp. 59–63, 1988.

[85] D. D. Streeter, H. M. Spotnitz, D. P. Patel, J. Ross, and E. H. Sonnenblick, “Fiber orientation in the canine left ventricle during diastole and systole.,” Circ. Res., vol. 24, no. 3, pp. 339–347, 1969.

[86] A. A. Holmes, D. F. Scollan, and R. L. Winslow, “Direct histological validation of diffusion tensor MRI in formaldehyde-fixed myocardium,” Magn Reson Med, vol. 44, no. 1, pp. 157–161, 2000.

[87] E. W. Hsu, A. L. Muzikant, S. A. Matulevicius, R. C. Penland, and C. S. Henriquez, “Magnetic resonance myocardial fiber-orientation mapping with direct histological correlation.,” Am. J. Physiol., vol. 274, pp. H1627–H1634, 1998.

[88] D. F. Scollan, A. Holmes, R. Winslow, and J. Forder, “Histological validation of myocardial microstructure obtained from diffusion tensor magnetic resonance imaging.,” Am. J. Physiol., vol. 275, no. 6 Pt 2, pp. H2308-18, 1998.

[89] J. M. Guccione, A. D. McCulloch, and L. K. Waldman, “Passive material properties of intact ventricular myocardium determined from a cylindrical model.,” J. Biomech. Eng., vol. 113, no. 1, pp. 42–55, 1991.

[90] J. M. Huyghe, T. Arts, D. H. van Campen, and R. S. Reneman, “Porous medium finite element model of the beating left ventricle.,” Am. J. Physiol., vol. 262, no. 4 Pt 2, pp. H1256–H1267, 1992.

[91] A. C. van Mil, J. Pearson, A. L. Drane, J. R. Cockcroft, B. McDonnell, and E. J. Stöhr, “Interaction between left ventricular twist mechanics and arterial haemodynamics during localised, non-metabolic hyperaemia with and without blood flow restriction,” Exp. Physiol., p. n/a-n/a, 2016.

[92] F. Tezuka, “Muscle fiber orientation in normal and hypertrophied hearts.,” Tohoku J. Exp. Med., vol. 948025, no. 948025, pp. 289–297, 1975.

[93] T. E. Carew and J. W. Covell, “Fiber orientation in hypertrophied canine left ventricle,” Am. J. Physiol. Hear. Circ. Physiol., vol. 236, no. 3, p. 0, 1979.

[94] J. H. Omens, D. E. Milkes, and J. W. Covell, “Effects of pressure overload on the passive mechanics of the rat left ventricle,” Ann. Biomed. Eng., vol. 23, no. 2, pp. 152–163, 1995.

[95] J. H. Omens, E. K. Rodriguez, and A. D. McCulloch, “Transmural changes in stress-free myocyte morphology during pressure overload hypertrophy in the rat.,” J. Mol. Cell. Cardiol., vol. 28, no. 9, pp. 1975–1983, 1996.

[96] B. Schmitt, K. Fedarava, J. Falkenberg, K. Rothaus, N. K. Bodhey, C. Reischauer, S. Kozerke, B. Schnackenburg, D. Westermann, P. P. Lunkenheimer, R. H. Anderson, F. Berger, and T. Kuehne, “Three-dimensional alignment of the aggregated myocytes in the normal and hypertrophic murine heart.,” J. Appl. Physiol., vol. 107, no. 3, pp. 921–927, 2009.

[97] M. R. Hill, M. A. Simon, D. Valdez-Jasso, W. Zhang, H. C. Champion, and M. S. Sacks, “Structural and Mechanical Adaptations of Right Ventricle Free Wall Myocardium to Pressure Overload,” Ann. Biomed. Eng., vol. 42, no. 12, pp. 2451–2465, 2014.

[98] R. H. Anderson, M. Smerup, D. Sanchez-Quintana, M. Loukas, and P. P. Lunkenheimer, “The three-dimensional arrangement of the myocytes in the ventricular walls.,” Clin. Anat., vol. 22, no. 1, pp. 64–76, 2009.

[99] S. H. Gilbert, A. P. Benson, R. D. Walton, and O. Bernus, “Slowed propagation across the compacta-trabeculata interface: A consequence of fiber and sheet anisotropy,” Proc. Annu. Int. Conf. IEEE Eng. Med. Biol. Soc. EMBS, pp. 1688–1692, 2011.

[100] I. J. LeGrice, Y. Takayama, and J. W. Covell, “Transverse Shear Along Myocardial Cleavage Planes Provides a Mechanism for Normal Systolic Wall Thickening,” Circ. Res., vol. 77, no. 1, pp. 182–193, Jul. 1995.

[101] J. D. Humphrey and F. C. Yin, “Constitutive relations and finite deformations of passive cardiac tissue II: stress analysis in the left ventricle,” Circ. Res., vol. 65, no. 3, pp. 805–817, 1989.

[102] D. H. Lin and F. C. Yin, “A multiaxial constitutive law for mammalian left ventricular myocardium in steady-state barium contracture or tetanus.,” J. Biomech. Eng., vol. 120, no. 4, pp. 504–517, 1998.

[103] G. Sommer, A. J. Schriefl, M. Andr??, M. Sacherer, C. Viertler, H. Wolinski, and G. A. Holzapfel, “Biomechanical properties and microstructure of human ventricular myocardium,” Acta Biomater., vol. 24, pp. 172–192, 2015.

[104] G. Sommer, D. C. Haspinger, M. Andr??, M. Sacherer, C. Viertler, P. Regitnig, and G. A. Holzapfel, “Quantification of Shear Deformations and Corresponding Stresses in the Biaxially Tested Human Myocardium,” Ann. Biomed. Eng., vol. 43, no. 10, pp. 2334–2348, 2015.

[105] T. Arts and R. S. Reneman, “Analysis of intramyocardial pressure (IMP). A model study.,” Bibl. Anat., no. 15 Pt 1, pp. 103–7, Jan. 1977.

[106] H. Ashikaga, J. W. Covell, and J. H. Omens, “Diastolic dysfunction in volume-overload hypertrophy is associated with abnormal shearing of myolaminar sheets.,” Am. J. Physiol. Heart Circ. Physiol., vol. 288, no. 6, pp. H2603-10, 2005.

[107] H. Ashikaga, B. a Coppola, K. G. Yamazaki, F. J. Villarreal, J. H. Omens, and J. W. Covell, “Changes in regional myocardial volume during the cardiac cycle: implications for transmural blood flow and cardiac structure.,” Am. J. Physiol. Heart Circ. Physiol., vol. 295, pp. H610–H618, 2008.

[108] J. Chen, W. Liu, H. Zhang, L. Lacy, X. Yang, S.-K. Song, S. a Wickline, and X. Yu, “Regional ventricular wall thickening reflects changes in cardiac fiber and sheet structure during contraction: quantification with diffusion tensor MRI.,” Am. J. Physiol. Heart Circ. Physiol., vol. 289, no. 5, pp. H1898–H1907, 2005.

[109] B. a Coppola and J. H. Omens, “Role of tissue structure on ventricular wall mechanics.,” Mol. Cell. Biomech., vol. 5, no. 3, pp. 183–96, 2008.

[110] J. W. Covell, “Tissue structure and ventricular wall mechanics.,” Circulation, vol. 118, pp. 699–701, 2008.

[111] A. Nikou, S. M. Dorsey, J. R. McGarvey, J. H. Gorman, J. A. Burdick, J. J. Pilla, R. C. Gorman, and J. F. Wenk, “Computational Modeling of Healthy Myocardium in Diastole,” Ann. Biomed. Eng., 2015.

[112] A. J. Pope, G. B. Sands, B. H. Smaill, and I. J. LeGrice, “Three-dimensional transmural organization of perimysial collagen in the heart.,” Am. J. Physiol. Heart Circ. Physiol., vol. 295, no. 3, pp. H1243–H1252, 2008.

[113] D. A. Hooks, M. L. Trew, B. J. Caldwell, G. B. Sands, I. J. LeGrice, and B. H. Smaill, “Laminar arrangement of ventricular myocytes influences electrical behavior of the heart,” Circ. Res., vol. 101, no. 10, pp. 103–113, 2007.

[114] A. Krishnamurthy, C. T. Villongco, J. Chuang, L. R. Frank, V. Nigam, E. Belezzuoli, P. Stark, D. E. Krummen, S. Narayan, J. H. Omens, A. D. McCulloch, and R. C. P. Kerckhoffs, “Patient-specific models of cardiac biomechanics,” J. Comput. Phys., vol. 244, pp. 4–21, 2013.

[115] J. E. Bishop and G. J. Laurent, “Collagen turnover and its regulation in the normal and hypertrophying heart.,” Eur. Heart J., vol. 16 Suppl C, pp. 38–44, 1995.

[116] N. Bursac, “Cardiac fibroblasts in pressure overload hypertrophy: The enemy within?,” J. Clin. Invest., vol. 124, no. 7, pp. 2850–2853, 2014.

[117] T. Moore-morris, N. Guimarães-camboa, I. Banerjee, A. C. Zambon, T. Kisseleva, A. Velayoudon, W. B. Stallcup, Y. Gu, N. D. Dalton, M. Cedenilla, R. Gomez-amaro, B. Zhou, D. A. Brenner, K. L. Peterson, J. Chen, and S. M. Evans, “Resident fibroblast lineages mediate pressure overload – induced cardiac fi brosis,” J. Clin. Invest., vol. 124, no. 7, pp. 1–14, 2014.

[118] R. Pick, J. S. Janicki, and K. T. Weber, “Myocardial fibrosis in nonhuman primate with pressure overload hypertrophy.,” Am. J. Pathol., vol. 135, no. 5, pp. 771–81, 1989.

[119] C. H. Conrad, W. W. Brooks, J. A. Hayes, S. Sen, K. G. Robinson, and O. H. L. Bing, “Myocardial Fibrosis and Stiffness With Hypertrophy and Heart Failure in the Spontaneously Hypertensive Rat,” Circ. , vol. 91, no. 1, pp. 161–170, Jan. 1995.

[120] G. M. Fomovsky, S. Thomopoulos, and J. W. Holmes, “Contribution of extracellular matrix to the mechanical properties of the heart,” J. Mol. Cell. Cardiol., vol. 48, no. 3, pp. 490–496, 2010.

[121] O. M. Hess, J. Schneider, R. Koch, C. Bamert, J. Grimm, and H. P. Krayenbuehl, "Diastolic function and myocardial structure in patients with myocardial hypertrophy. Special reference to normalized viscoelastic data," Circulation, vol. 63, no. 2, pp. 360–371, 1981.

[122] K. U. Thiedemann, C. Holubarsch, I. Medugorac, and R. Jacob, "Connective tissue content and myocardial stiffness in pressure overload hypertrophy. A combined study of morphologic, morphometric, biochemical, and mechanical parameters.," Basic Res. Cardiol., vol. 78, no. 2, pp. 140–55, 1983.

[123] I. J. LeGrice, a. J. Pope, G. B. Sands, G. Whalley, R. N. Doughty, and B. H. Smaill, "Progression of myocardial remodeling and mechanical dysfunction in the spontaneously hypertensive rat," AJP Hear. Circ. Physiol., pp. 1353–1365, 2012.

[124] J. H. Omens and Y. C. Fung, "Residual strain in rat left ventricle.," Circ. Res., vol. 66, no. 1, pp. 37–45, 1990.

[125] C. J. Chuong and Y. C. Fung, "Residual Stress in Arteries," Front. Biomech., pp. 117–129, 1986.

[126] E. K. Rodriguez, J. H. Omens, L. K. Waldman, and a D. McCulloch, "Effect of residual stress on transmural sarcomere length distributions in rat left ventricle.," Am. J. Physiol., vol. 264, no. 4 Pt 2, pp. H1048–H1056, 1993.

[127] L. a Taber, N. Hu, T. Pexieder, E. B. Clark, and B. B. Keller, "Residual strain in the ventricle of the stage 16-24 chick embryo.," Circ. Res., vol. 72, no. 2, pp. 455–62, 1993.

[128] K. D. Costa, K. May-Newman, D. Farr, W. G. O'Dell, a D. McCulloch, and J. H. Omens, "Three-dimensional residual strain in midanterior canine left ventricle.," Am. J. Physiol., vol. 273, no. 4 Pt 2, pp. H1968–H1976, 1997.

[129] J. H. Omens, a D. McCulloch, and J. C. Criscione, "Complex distributions of residual stress and strain in the mouse left ventricle: experimental and theoretical models.," Biomech. Model. Mechanobiol., vol. 1, no. 4, pp. 267–77, 2003.

[130] Y. C. Fung and S. Q. Liu, "Change of residual strains in arteries due to hypertrophy caused by aortic constriction.," Circ. Res., vol. 65, no. 5, pp. 1340–9, 1989.

[131] E. K. Rodriguez, A. Hoger, and A. D. Mcculloch, "Stress-dependent finite growth in soft elastic tissues," J. Biomech., vol. 27, no. 4, pp. 455–467, 1994.

[132] L. A. Taber and S. Chabert, "Theoretical and experimental study of growth and remodeling in the developing heart," Biomech. Model. Mechanobiol., vol. 1, no. 1, pp. 29–43, 2002.

[133] S. M. Weis, J. L. Emery, K. D. Becker, D. J. McBride, J. H. Omens, and A. D. McCulloch, “Myocardial Mechanics and Collagen Structure in the Osteogenesis Imperfecta Murine (oim),” Circ. Res., vol. 87, no. 8, pp. 663–669, 2000.

[134] J. H. Omens, S. M. Vaplon, B. Fazeli, and A. D. McCulloch, “Left ventricular geometric remodeling and residual stress in the rat heart,” J. Biomech. Eng., vol. 120, no. 6, pp. 715–719, 1998.

[135] D. A. MacKenna, J. H. Omens, A. D. McCulloch, and J. W. Covell, “Contribution of collagen matrix to passive left ventricular mechanics in isolated rat hearts.,” Am. J. Physiol., vol. 266, no. 3 Pt 2, pp. H1007-18, 1994.

[136] D. A. MacKenna, S. M. Vaplon, and A. D. McCulloch, “Microstructural model of perimysial collagen fibers for resting myocardial mechanics during ventricular filling.,” Am. J. Physiol., vol. 273, no. 3 Pt 2, pp. H1576-86, 1997.

[137] O. H. Bing, S. Matsushita, B. L. Fanburg, and H. J. Levine, “Mechanical properties of rat cardiac muscle during experimental hypertrophy.,” Circ. Res., vol. 28, no. 2, pp. 234–245, 1971.

[138] P. G. Caspari, M. Newcomb, K. Gibson, and P. Harris, “Collagen in the normal and hypertrophied human ventricle.,” Cardiovasc. Res., vol. 11, no. 6, pp. 554–8, Nov. 1977.

[139] K. T. Weber, J. E. Jalil, J. S. Janicki, and R. Pick, “Myocardial collagen remodeling in pressure overload hypertrophy. A case for interstitial heart disease.,” Am. J. Hypertens., vol. 2, no. 12 Pt 1, pp. 931–40, Dec. 1989.

[140] K. L. Herrmann, A. D. McCulloch, and J. H. Omens, “Glycated collagen cross-linking alters cardiac mechanics in volume-overload hypertrophy.,” Am. J. Physiol. Heart Circ. Physiol., vol. 284, no. 4, pp. H1277-84, 2003.

[141] D. Mukherjee and S. Sen, “Collagen phenotypes during development and regression of myocardial hypertrophy in spontaneously hypertensive rats.,” Circ. Res., vol. 67, no. 6, pp. 1474–80, 1990.

[142] L. Williams, N. Howell, D. Pagano, P. Andreka, M. Vertesaljai, T. Pecor, M. Frenneaux, and H. Granzier, “Titin isoform expression in aortic stenosis.,” Clin. Sci. (Lond)., vol. 117, no. 6, pp. 237–42, 2009.

[143] C. Neagoe, C. A. Opitz, I. Makarenko, and W. A. Linke, “Gigantic variety: Expression patterns of titin isoforms in striated muscles and consequences for myofibrillar passive stiffness,” J. Muscle Res. Cell Motil., vol. 24, no. 2–3, pp. 175–189, 2003.

[144] O. Cazorla, A. Freiburg, M. Helmes, T. Centner, M. McNabb, Y. Wu, K. Trombitás, S. Labeit, and H. Granzier, "Differential expression of cardiac titin isoforms and modulation of cellular stiffness.," Circ. Res., vol. 86, no. 1, pp. 59–67, 2000.

[145] C. M. M. Warren, M. C. Jordan, K. P. Roos, P. R. Krzesinski, and M. L. Greaser, "Titin isoform expression in normal and hypertensive myocardium," Cardiovasc. …, vol. 59, no. 1, pp. 86–94, 2003.

[146] I. Morano, F. Hofmann, M. Zimmer, and J. C. Ruegg, "The influence of P-light chain phosphorylation by myosin light chain kinase on the calcium sensitivity of chemically skinned heart fibres," FEBS Lett., vol. 189, no. 2, pp. 221–224, 1985.

[147] M. C. Olsson, J. R. Patel, D. P. Fitzsimons, J. W. Walker, and R. L. Moss, "Basal myosin light chain phosphorylation is a determinant of Ca2+ sensitivity of force and activation dependence of the kinetics of myocardial force development.," Am J Physiol Hear. Circ Physiol, vol. 287, no. 6, pp. H2712-8, 2004.

[148] J. S. Davis, S. Hassanzadeh, S. Winitsky, H. Lin, C. Satorius, R. Vemuri, A. H. Aletras, H. Wen, and N. D. Epstein, "The overall pattern of cardiac contraction depends on a spatial gradient of myosin regulatory light chain phosphorylation," Cell, vol. 107, no. 5, pp. 631–641, 2001.

[149] F. Sheikh, K. Ouyang, S. G. Campbell, R. C. Lyon, J. Chuang, D. Fitzsimons, J. Tangney, C. G. Hidalgo, C. S. Chung, H. Cheng, N. D. Dalton, Y. Gu, H. Kasahara, M. Ghassemian, J. H. Omens, K. L. Peterson, H. L. Granzier, R. L. Moss, A. D. McCulloch, and J. Chen, "Mouse and computational models link Mlc2v dephosphorylation to altered myosin kinetics in early cardiac disease," J. Clin. Invest., vol. 122, no. 4, pp. 1209–1221, 2012.

[150] C. Toepfer, V. Caorsi, T. Kampourakis, M. B. Sikkel, T. G. West, M. C. Leung, S. A. Al-Saud, K. T. MacLeod, A. R. Lyon, S. B. Marston, J. R. Sellers, and M. A. Ferenczi, "Myosin regulatory light chain (RLC) phosphorylation change as a modulator of cardiac muscle contraction in disease," J. Biol. Chem., vol. 288, no. 19, pp. 13446–13454, 2013.

[151] K. Kotlo, K. R. Johnson, J. M. Grillon, D. L. Geenen, P. deTombe, and R. S. Danziger, "Phosphoprotein abundance changes in hypertensive cardiac remodeling," J. Proteomics, vol. 77, pp. 1–13, 2012.

[152] S. A. Warren, L. E. Briggs, H. Zeng, J. Chuang, E. I. Chang, R. Terada, M. Li, M. S. Swanson, S. H. Lecker, M. S. Willis, F. G. Spinale, J. Maupin-Furlowe, J. R. McMullen, R. L. Moss, and H. Kasahara, "Myosin light chain phosphorylation is critical for adaptation to cardiac stress," Circulation, vol. 126, no. 22, pp. 2575–2588, 2012.

[153] A. Karabina, K. Kazmierczak, D. Szczesna-Cordary, and J. R. Moore, “Myosin regulatory light chain phosphorylation enhances cardiac β-myosin in vitro motility under load.,” Arch. Biochem. Biophys., vol. 580, pp. 14–21, 2015.

[154] C.-C. Yuan, P. Muthu, K. Kazmierczak, J. Liang, W. Huang, T. C. Irving, R. M. Kanashiro-Takeuchi, J. M. Hare, and D. Szczesna-Cordary, “Constitutive phosphorylation of cardiac myosin regulatory light chain prevents development of hypertrophic cardiomyopathy in mice.,” Proc. Natl. Acad. Sci. U. S. A., vol. 112, no. 30, pp. E4138-46, 2015.

[155] M. T. Massengill, H. M. Ashraf, R. R. Chowdhury, S. M. Chrzanowski, J. Kar, S. A. Warren, G. A. Walter, H. Zeng, B.-H. Kang, R. H. Anderson, R. L. Moss, and H. Kasahara, “Acute heart failure with cardiomyocyte atrophy induced in adult mice by ablation of cardiac myosin light chain kinase.,” Cardiovasc. Res., Mar. 2016.

[156] R. Stones, S. C. Calaghan, R. Billeter, S. M. Harrison, and E. White, “Transmural variations in gene expression of stretch-modulated proteins in the rat left ventricle,” Pflugers Arch. Eur. J. Physiol., vol. 454, no. 4, pp. 545–549, 2007.

[157] S. G. Campbell, P. Haynes, W. Kelsey Snapp, K. E. Nava, and K. S. Campbell, “Altered ventricular torsion and transmural patterns of myocyte relaxation precede heart failure in aging F344 rats.,” Am. J. Physiol. Heart Circ. Physiol., vol. 305, no. 5, pp. H676-86, 2013.

[158] J. E. Stelzer, H. S. Norman, P. P. Chen, J. R. Patel, and R. L. Moss, “Transmural variation in myosin heavy chain isoform expression modulates the timing of myocardial force generation in porcine left ventricle,” J Physiol, vol. 586, no. 2008, pp. 5203–5214, 2008.

[159] T. J. Herron and K. S. McDonald, “Small amounts of alpha-myosin heavy chain isoform expression significantly increase power output of rat cardiac myocyte fragments.,” Circ. Res., vol. 90, no. 11, pp. 1150–1152, 2002.

[160] M. Krenz and J. Robbins, “Impact of beta-myosin heavy chain expression on cardiac function during stress,” J. Am. Coll. Cardiol., vol. 44, no. 12, pp. 2390–2397, 2004.

[161] K. Nakao, W. Minobe, R. Roden, M. R. Bristow, and L. A. Leinwand, “Myosin heavy chain gene expression in human heart failure,” J Clin Invest, vol. 100, no. 9, pp. 2362–2370, 1997.

[162] C. Antzelevitch, S. Sicouri, S. H. Litovsky, A. Lukas, S. C. Krishnan, J. M. Di Diego, G. a. Gintant, and D. W. Liu, “Heterogeneity Within the Ventricular Wall,” Circ. Res., vol. 69, no. 6, pp. 1427–1449, 1991.

[163] J. E. Dixon, W. Shi, H.-S. Wang, C. McDonald, H. Yu, R. S. Wymore, I. S. Cohen, and D. McKinnon, “Role of the Kv4.3 K+ Channel in Ventricular Muscle: A Molecular Correlate for the Transient Outward Current,” Circ. Res., vol. 79, no. 4, pp. 659–668, Oct. 1996.

[164] C. Teutsch, R. P. Kondo, D. A. Dederko, J. Chrast, K. R. Chien, and W. R. Giles, “Spatial distributions of Kv4 channels and KChip2 isoforms in the murine heart based on laser capture microdissection,” Cardiovasc. Res., vol. 73, no. 4, pp. 739–749, 2007.

[165] B. Rosati, Z. Pan, S. Lypen, H. S. Wang, I. Cohen, J. E. Dixon, and D. McKinnon, “Regulation of KChIP2 potassium channel β subunit gene expression underlies the gradient of transient outward current in canine and human ventricle,” J. Physiol., vol. 533, no. 1, pp. 119–125, 2001.

[166] B. Rosati, F. Grau, S. Rodriguez, H. Li, J. M. Nerbonne, and D. McKinnon, “Concordant expression of KChIP2 mRNA, protein and transient outward current throughout the canine ventricle.,” J. Physiol., vol. 548, no. Pt 3, pp. 815–22, 2003.

[167] R. B. Clark, R. A. Bouchard, E. Salinas-Stefanon, J. Sanchez-Chapula, and W. R. Giles, “Heterogeneity of action potential waveforms and potassium currents in rat ventricle.,” Cardiovasc. Res., vol. 27, no. 10, pp. 1795–9, Oct. 1993.

[168] Y. Wang, J. Cheng, G. Chen, F. Rob, R. Haris Naseem, L. Nguyen, J. L. Johnstone, and J. A. Hill, “Remodeling of outward K+ currents in pressure-overload heart failure,” J. Cardiovasc. Electrophysiol., vol. 18, no. 8, pp. 869–875, 2007.

[169] M. Bodnár, G. Schlichthörl, and J. Daut, “The potassium current carried by TREK-1 channels in rat cardiac ventricular muscle.,” Pflugers Arch., vol. 467, no. 5, pp. 1069–79, 2015.

[170] D. Kelly, L. Mackenzie, P. Hunter, B. Smaill, and D. A. Saint, “Gene expression of stretch-activated channels and mechanoelectric feedback in the heart,” Clin. Exp. Pharmacol. Physiol., vol. 33, no. 7, pp. 642–648, 2006.

[171] J. H. C. Tan, W. Liu, and D. a Saint, “Differential expression of the mechanosensitive potassium channel TREK-1 in epicardial and endocardial myocytes in rat ventricle.,” Exp. Physiol., vol. 89, no. 3, pp. 237–242, 2004.

[172] W. Wang, M. Zhang, P. Li, H. Yuan, N. Feng, Y. Peng, L. Wang, and X. Wang, “An Increased TREK-1-like Potassium Current in Ventricular Myocytes During Rat Cardiac Hypertrophy.,” J. Cardiovasc. Pharmacol., vol. 61, no. 4, pp. 302–10, 2013.

[173] A. O. Grant, “Cardiac ion channels,” Circ. Arrhythmia Electrophysiol., vol. 2, no. 2, pp. 185–194, 2009.

[174] J. M. Nerbonne and R. S. Kass, “Molecular physiology of cardiac repolarization.,” Physiol. Rev., vol. 85, no. 4, pp. 1205–53, 2005.

[175] D. P. Lackey, E. D. Carruth, R. A. Lasher, J. Boenisch, F. B. Sachse, and R. W. Hitchcock, “Three-dimensional modeling and quantitative analysis of gap junction distributions in cardiac tissue,” Ann. Biomed. Eng., vol. 39, no. 11, pp. 2683–2694, 2011.

[176] K. A. Yamada, E. M. Kanter, K. G. Green, and J. E. Saffitz, “Transmural distribution of connexins in rodent hearts,” J. Cardiovasc. Electrophysiol., vol. 15, no. 6, pp. 710–715, 2004.

[177] S. Poelzing, F. G. Akar, E. Baron, and D. S. Rosenbaum, “Heterogeneous connexin43 expression produces electrophysiological heterogeneities across ventricular wall.,” Am. J. Physiol. Heart Circ. Physiol., vol. 286, no. 5, pp. H2001–H2009, 2004.

[178] C. S. McLachlan, P. R. Jusuf, N. Rummery, S. K. Kummerfeld, B. Hambly, M. A. McGuire, and V. Turner, “Tyramide signal amplification enhances the detectable distribution of connexin-43 positive gap junctions across the ventricular wall of the rabbit heart.,” Arch. Histol. Cytol., vol. 66, no. 4, pp. 359–65, Oct. 2003.

[179] S. Poelzing and D. S. Rosenbaum, “Altered connexin43 expression produces arrhythmia substrate in heart failure.,” Am. J. Physiol. Heart Circ. Physiol., vol. 287, no. 4, pp. H1762-70, 2004.

[180] S. Kostin, S. Dammer, S. Hein, W. P. Klovekorn, E. P. Bauer, and J. Schaper, “Connexin 43 expression and distribution in compensated and decompensated cardiac hypertrophy in patients with aortic stenosis,” Cardiovasc. Res., vol. 62, no. 2, pp. 426–436, 2004.

[181] L. Emdad, M. Uzzaman, Y. Takagishi, H. Honjo, T. Uchida, N. J. Severs, I. Kodama, and Y. Murata, “Gap junction remodeling in hypertrophied left ventricles of aortic-banded rats: prevention by angiotensin II type 1 receptor blockade.,” J. Mol. Cell. Cardiol., vol. 33, no. 2, pp. 219–31, 2001.

[182] J. Qu, F. M. Volpicelli, L. I. Garcia, N. Sandeep, J. Zhang, L. M??rquez-Rosado, P. D. Lampe, and G. I. Fishman, “Gap junction remodeling and spironolactone-dependent reverse remodeling in the hypertrophied heart,” Circ. Res., vol. 104, no. 3, pp. 365–371, 2009.

[183] B. C. Schwab, G. Seemann, R. A. Lasher, N. S. Torres, E. M. Wulfers, M. Arp, E. D. Carruth, J. H. B. Bridge, and F. B. Sachse, “Quantitative analysis of cardiac tissue including fibroblasts using three-dimensional confocal microscopy and image reconstruction: Towards a basis for electrophysiological modeling,” IEEE Trans. Med. Imaging, vol. 32, no. 5, pp. 862–872, 2013.

[184] K. R. Laurita, R. Katra, B. Wible, X. Wan, and M. H. Koo, “Transmural heterogeneity of calcium handling in canine,” Circ. Res., vol. 92, no. 6, pp. 668–675, 2003.

[185] K. R. Laurita and R. P. Katra, “Delayed afterdepolarization-mediated triggered activity associated with slow calcium sequestration near the endocardium,” J. Cardiovasc. Electrophysiol., vol. 16, no. 4, pp. 418–424, 2005.

[186] T. Anderson, J. Wulfkuhle, E. Petricoin, and R. L. Winslow, “High resolution mapping of the cardiac transmural proteome using reverse phase protein microarrays.,” Mol. Cell. Proteomics, vol. 10, no. 7, p. M111.008037, 2011.

[187] Q. Lou, V. V. Fedorov, A. V. Glukhov, N. Moazami, V. G. Fast, and I. R. Efimov, “Transmural heterogeneity and remodeling of ventricular excitation- contraction coupling in human heart failure,” Circulation, vol. 123, no. 17, pp. 1881–1890, 2011.

[188] J. Prestle, S. Dieterich, M. Preuss, U. Bieligk, and G. Hasenfuss, “Heterogeneous transmural gene expression of calcium-handling proteins and natriuretic peptides in the failing human heart,” Cardiovasc. Res., vol. 4, no. 4, pp. 323–331, 1999.

[189] A. M. Feldman, E. O. Weinberg, P. E. Ray, and B. H. Lorell, “Selective changes in cardiac gene expression during compensated hypertrophy and the transition to cardiac decompensation in rats with chronic aortic banding.,” Circ. Res., vol. 73, no. 1, pp. 184–192, 1993.

[190] J. M. Cordeiro, L. Greene, C. Heilmann, D. Antzelevitch, and C. Antzelevitch, “Transmural heterogeneity of calcium activity and mechanical function in the canine left ventricle,” Am. J. Physiol. - Hear. Circ. Physiol., vol. 286, no. 4, pp. H1471–H1479, 2004.

[191] S. G. Campbell, E. Howard, J. Aguado-Sierra, B. a Coppola, J. H. Omens, L. J. Mulligan, A. D. McCulloch, and R. C. P. Kerckhoffs, “Effect of transmurally heterogeneous myocyte excitation-contraction coupling on canine left ventricular electromechanics.,” Exp. Physiol., vol. 94, no. 5, pp. 541–552, 2009.

[192] R. Erkens, C. M. Kramer, W. L??ckst??dt, C. Panknin, L. Krause, M. Weidenbach, J. Dirzka, T. Krenz, E. Mergia, T. Suvorava, M. Kelm, and M. M. Cortese-Krott, “Left ventricular diastolic dysfunction in Nrf2 knock out mice is associated with cardiac hypertrophy, decreased expression of SERCA2a, and preserved endothelial function,” Free Radic. Biol. Med., vol. 89, pp. 906–917, 2015.

[193] K. F. Frank, B. Bolck, E. Erdmann, and R. H. G. Schwinger, “S arcoplasmic reticulum Ca -ATPase modulates cardiac contraction and relaxation,” Cardiovasc. Res., vol. 57, pp. 20–27, 2003.

[194] D. De La Bastie, D. Levitsky, L. Rappaport, J. J. Mercadier, F. Marotte, C. Wisnewsky, V. Brovkovich, K. Schwartz, and a M. Lompré, “Function of the sarcoplasmic reticulum and expression of its Ca2(+)-ATPase gene in pressure overload-induced cardiac hypertrophy in the rat.,” Circ. Res., vol. 66, no. 2, pp. 554–564, 1990.

[195] K. Wong, K. R. Boheler, M. Petrou, and M. H. Yacoub, “Pharmacological Modulation of Pressure-Overload Cardiac Hypertrophy : Changes in Ventricular Function, Extracellular Matrix, and Gene Expression,” Circulation, vol. 96, no. 7, pp. 2239–2246, Oct. 1997.

[196] M. Anger, A. M. Lompré, O. Vallot, F. Marotte, L. Rappaport, and J. L. Samuel, “Cellular distribution of Ca2+ pumps and Ca2+ release channels in rat cardiac hypertrophy induced by aortic stenosis.,” Circulation, vol. 98, no. 22, pp. 2477–86, Dec. 1998.

2. Regional Gradients of Calcium Handling and Sarcomere Activating Proteins in Pressure Overload Hypertrophy in the Rat Ventricles

2.1. Introduction

As has been detailed in Chapter 1, regional variations in tissue structures in the heart obviously play an important role in supporting and maintaining optimal regional and global function in the left ventricle, and the disruption of normal structural features likely contributes negatively to pump function. However, the interplay between the myriad structural features that exhibit such regional variation, and the contributions of each to the global pump function of the heart is not known. Computational modeling is one potential approach to study these interactions. Finite element modeling of the ventricles allows for defining physiology-based mathematical relationships that vary spatially across a discretized mesh and which contribute to the generation of stresses and strains [1]. Such modeling constitutes the best current approach to studying these interactions, however, they rely on accurate measurements of regionally varying structural features from experimentation, such as protein distributions.

One such transmurally varying protein that has been previously described is the calcium (Ca^{2+}) handling protein, sarco-/endoplasmic reticulum calcium ATPase (SERCA2a), whose primary function is to remove Ca^{2+} from the cytosol of myocytes after activation. As mentioned in Chapter 1, it has been shown that SERCA2a exhibits a transmural gradient in normal canine hearts, with more SERCA2a in the subepicardium (EPI) than the subendocardium (ENDO) [2]–[4]. This regional gradient was confirmed in human hearts but was not observed in the rat [5]–[8].

Ca^{2+} is the signaling messenger that is responsible for activating sarcomeric contraction in myocytes and is therefore an important component for maintaining normal

cardiac function. Considering this fact, and the previously described transmural distributions of tissue features such as myocyte geometry, electrical activation and repolarization, and more [9], [10], it is not illogical to predict that Ca^{2+} handling proteins may also exhibit a transmural gradient, especially given the evidence in favor of this pattern in other species. Additionally, a better understanding of regional Ca^{2+} dynamics could provide valuable insight as to how cardiac function is optimized in normal tissue and how it is affected in disease. Although it is clear from the literature that regional variations in structural features and protein density are present in the normal mammalian ventricles, most studies investigating remodeling during disease ignore the regional gradients described and assume that the changes in protein level are global. Therefore, a clear understanding of the regional changes in protein density in disease is lacking.

We hypothesized that even if it is the case that SERCA2a does not exhibit a transmural gradient in the rat LV [8], other Ca^{2+} handling proteins such as phospholamban (PLB), the plasma membrane calcium ATPase (PMCA), or the sodium-calcium exchanger (NCX) vary transmurally to produce a similar functional effect in Ca^{2+} dynamics. We explored this hypothesis using western blotting (WB) and immunofluorescence microscopy on entire cross-sections of both ventricles from rats with four weeks of transverse aortic constriction (TAC) and sham controls (SHAM).

As an exploratory experiment, we also investigated the regional variations in myosin light chain kinase (MLCK) and the gap junction channel protein connexin-43 (Cx43). Phosphorylation of myosin light chain (facilitated by MLCK) modulates the sensitivity of myosin light chain to Ca^{2+} and has been shown to vary transmurally in the mouse LV with higher levels of phosphorylation in EPI than ENDO [11]. Also, Cx43 levels were higher in

ENDO than EPI in mouse [12], dog [13], and rabbit [14], but not in rat [12]. Cx43 is important in maintaining normal electrical conduction and is known to remodel with respect to myocyte geometry in diseases such as heart failure [15], compensated hypertrophy [16], and myocardial infarction [17]. The balance of these transmural gradients are considered important mechanisms to maintain optimal cardiac function in the healthy heart.

2.2. Materials and Methods

2.2.1. Transverse Aortic Constriction (TAC) Surgery

All procedures were performed in compliance with the National Institutes of Health *Guide for the Care and Use of Laboratory Animals* and were approved by the Institutional Animal Care and Use Committee. A total of 22 male Sprague-Dawley rats (mean body weight = 210 ± 12 g) were randomly separated into two groups, SHAM (N=8) or TAC (N=14). Anesthesia was administered via inhalation of 1.25%-2.00% isoflurane and confirmed with a toe pinch. The chest was opened via lateral thoracotomy, and the aortic arch was exposed. For TAC animals, a hemo-clip was inserted between the right innominate and left carotid arteries and clamped down to a width of 0.5 mm, which constricted the aorta to approximately 60% the original diameter. SHAM controls underwent the same procedure, with the exception of clip insertion. The surgical incisions were sutured closed and the animal recovered normally. The clip remained in the animal until four weeks after the surgery date. M-mode echocardiographic data were obtained 1 day prior to the surgery, at two weeks, and at four weeks after surgery.

2.2.2. Dissection into Regions

At the four-week time point, the heart was excised, blotted dry, weighed, and placed in high-potassium Krebs-Henseleit buffer. Hearts were then dissected on ice as shown in **Figure**

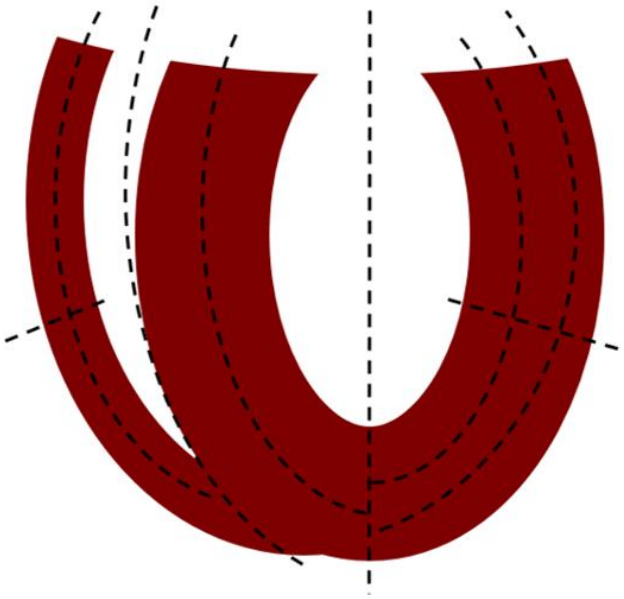

Figure 2.1. Regional dissection of the ventricles. Schematic illustration of the sectioning method used to divide ventricles regionally. 12 total regions were defined. The LV free wall was divided longitudinally into apex and base, then transmurally for EPI, MID, and ENDO. The RV was divided twice longitudinally (apex and base), and these were divided twice into EPI and ENDO. The SP was only divided transmurally into EPI and ENDO.

2.1, described as follows: A cut was made inferior to the valve plane using a razor blade to isolate the ventricles from the atria. Ventricles were then separated into left ventricular (LV) free wall, septum (SP), and right ventricular (RV) free wall. The LV free wall was subdivided into two longitudinal sections – apex and base, and each of those were subdivided further transmurally into EPI, mid-myocardium (MID), and ENDO. The RV was also divided into two longitudinal sections (apex and base) but only two transmural sections (EPI and ENDO), and the SP was only divided transmurally into EPI and ENDO. The RV side of the SP was considered EPI.

2.2.3. Protein Isolation

Protein was isolated from these regions in the following manner. Tissue was placed in RNAlater (ThermoScientific AM7020) and stored at room temperature. Tissue was lysed with

a Knotes Duall # 20 glass Dounce homogenizer in RIPA lysis buffer (50mM Tris-HCl, 150mM NaCl, 0.1% Sodium Dodecyl Sulfate, 0.5% Sodium Deoxycholate, 1% Triton-X 100, 1X Halt Protease & Phosphatase Inhibitor Cocktail (78442 ThermoFisher Scientific) in Ultra-pure water). Cell lysates were vortexed three times for 15 seconds at maximum speed, rocked on ice for 15 minutes, centrifuged at 15,000 x g for 10 mins at 4°C. Supernatant concentration was determined by BCA assay (23235 ThermoFisher Scientific).

2.2.4. Western Blot

Measurements were performed with a standard Western Blot protocol using ThermoScientific Mini Gel Tank (#A25977), Bolt 4-12% Bis-Tris gels (such as #NW04125BOX), PVDF 0.2um pore size membrane (LC2002). Antibodies used from Santa Cruz Biotechnology: SERCA2a, 1:2000 (#sc-376235), NCX, 1:200 (#sc-32881), PMCA, 1:100 (#sc-271917), PLB, 1:200 (#sc-30142). Antibodies from other vendors: glyceraldehyde 3-phosphate dehydrogenase (GAPDH), 1:10,000 (AbCam #ab9484), Connexin43, 1:8000 (Sigma #C6219), MLCK, 1:5000 (AbCam #ab76092). Secondary antibodies used: Goat anti-Mouse-HRP, 1:5000-1:100,000 (Sigma #A5478), Goat anti-Rabbit, 1:2500-1:3000 (Cell Signaling #7074), Donkey anti-Goat, 1:5000 (Novex #A15999). Western blot quantification was performed in ImageJ [18] (**Figure 2.2**).

2.2.5. Data Analysis and Statistics

All statistical comparisons between groups were performed in MatLab (The MathWorks, Natick, MA). Comparisons of measurements comparing TAC and SHAM groups are represented as mean ± SEM. Once raw data were acquired and compiled, protein levels were normalized to GAPDH or α-Actinin for each run. Analysis of variance (ANOVA) was performed for each protein investigated for the LV, RV, and SP, with intervention

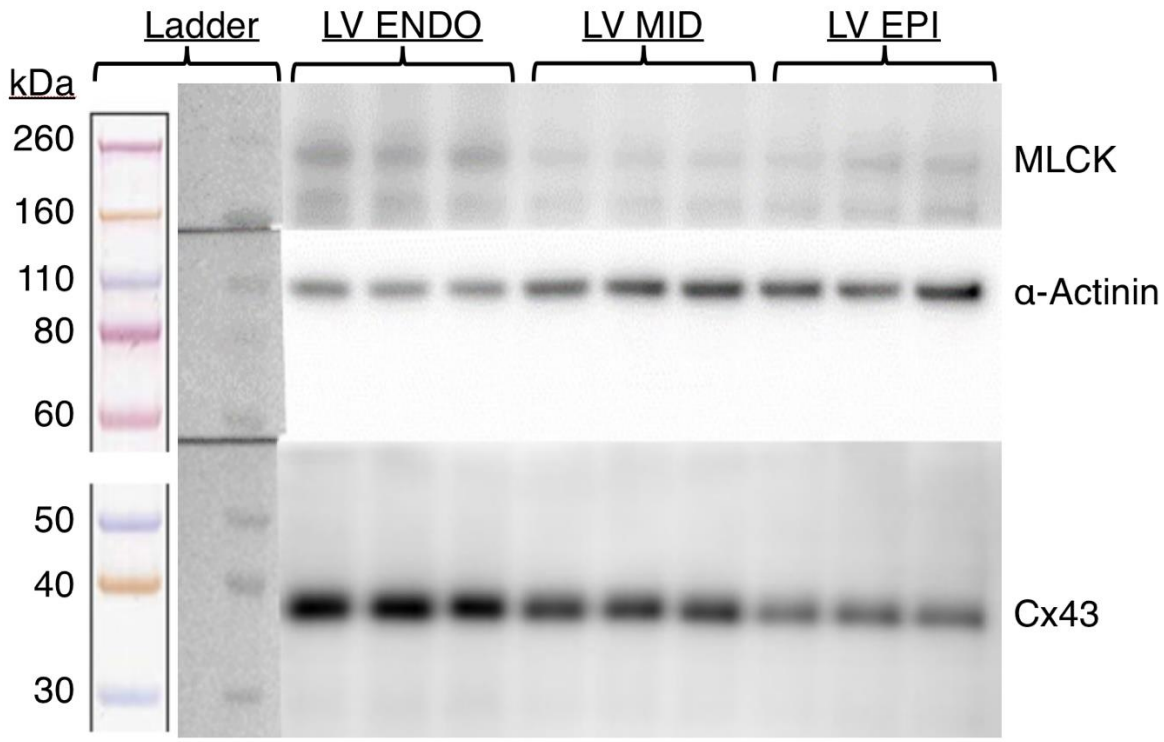

Figure 2.2. Representative western blot. Both MLCK and Cx43 were normalized to α-Actinin. An obvious transmural gradient in Cx43 (~43 kDa) is observed in this sample. MLCK signal was lower overall than both Cx43 and α-Actinin. This may reduce the chances of observing a transmural gradient even if one truly exists due to higher variance.

(SHAM/TAC), transmural position, and longitudinal position as factors, and total protein as the dependent variable.

Only population marginal means and two-factor interaction effects were considered for this study. The percent difference of TAC levels vs. SHAM were computed for each region. Significance was defined as a p-value < 0.05, and for population marginal means, p-values were corrected for multiple comparisons using the Tukey-Kramer method.

2.2.6. Immunofluorescence Microscopy of Entire Ventricle Cross-Sections

As an additional method to evaluate the normal regional variations in protein levels of Cx43 and SERCA2a in higher detail, we sought to generate a high-resolution map of immunofluorescence intensity in entire cross-sections of rat ventricles. A separate set of rats

Table 2.1. ANOVAs for regional and group variation in protein density

Main Region	Test	PLB	PMCA	NCX	SERCA2a	MLCK	Cx43
Overall	Hyp	0.413	0.847	0.215	0.281	0.839	0.016
	Region	**<0.001***	0.405	**<0.05***	0.593	0.227	0.077
	Hyp*Region	0.965	0.894	0.631	0.467	0.813	0.487
LV	Hyp	0.254	0.423	0.190	**<0.01***	0.249	0.765
	Hyp*Trans	0.642	0.751	0.774	0.557	0.661	0.846
	Hyp*Long	0.485	0.430	0.109	0.992	0.687	0.788
RV	Hyp	0.615	0.216	0.410	0.246	0.148	**<0.01***
	Hyp*Trans	0.430	0.572	0.378	0.960	0.725	0.193
	Hyp*Long	0.458	0.431	0.959	0.673	0.545	0.681
SP	Hyp	0.502	0.682	0.294	0.765	0.832	0.077
	Trans	0.483	0.131	0.186	0.518	0.082	0.033
	Hyp*Trans	0.629	0.420	0.210	0.522	0.202	0.700

of similar weight were anesthetized, and hearts were removed, blotted dry and weighed. Hearts were suspended and retrograde perfused with Krebs-Henseleit buffer until the tissue was cleared of blood and regular beating resumed. A modified Krebs-Henseleit solution with high potassium was then used to arrest the heart, and 4% paraformaldehyde in PBS was used to fix the heart in the slack state. The hearts were then dropped into 50 ml of 4% paraformaldehyde in PBS until sectioning.

2.2.7. Tissue Sectioning, Staining, and Imaging

Whole hearts were embedded in OCT (Leica Biosystems, Wetzlar, Germany) after ensuring that no residual fixative remained inside the ventricle chambers and that both were filled with OCT with no air bubbles. Samples were frozen and stored at -80°C until sectioning. Axial sections were acquired at 20-µm thickness through the length of the ventricles and mounted on glass slides. Primary antibodies used were as follows: Cx43 produced in rabbit (1:2000, cat# SIGMA C6219, Sigma-Aldrich, Inc.); SERCA2a produced in mouse (1:200, cat# sc-376235, Santa Cruz Biotechnology, Inc.); α-Actinin (control) produced

in mouse (1:500, cat# sc-1506, Santa Cruz Biotechnology, Inc). Secondary antibodies used were goat anti-mouse conjugated with Alexa Fluor-488 secondary antibody (1:800, cat# A11029, Invitrogen, Inc.) or goat anti-rabbit IgG conjugated with FITC secondary antibody (1:500, cat# sc-2012, Santa Cruz Biotechnology, Inc). Only one primary antibody was used for each section. Sections were washed with PBS, permeabilized with 0.5% Triton X-100 for 45 minutes at room temperature and washed again. Blocking was performed with goat serum (0.5%), with 1% bovine serum albumin (BSA) in PBS for 45 minutes at room temperature, and sections were washed again. Primary antibodies were diluted in 1% BSA in PBS and applied to slides overnight at 4°C. Slides were then washed again, and secondary antibodies (also diluted in PBS with 1% BSA) were applied for 1 hour at room temperature in the dark. After a final wash, Prolong Gold w/DAPI was applied, cover slips were placed carefully on the sample, and sections were dried shielded from light overnight. Slides were sealed with nail polish.

Images were acquired using a Nanozoomer slide scanning microscope (Hamamatsu, Hamamatsu City, Shizuoka, Japan). A 20x objective with 0.75 NA was used to obtain brightfield and fluorescence images with Texas Red, FITC, and DAPI filters. Imaging parameters included the following: FOV: ~13mm×13mm, resolution: ~450 nm/pixel isotropic, resulting in a final image matrix of ~28,000×28,000. We observed strong autofluorescence in all channels and therefore attempted to reduce this effect using the Texas Red image. Although we attempted to quantify the data from intensity or density of punctate points (in the case of Cx43), this proved difficult and ambiguous, so the images herein are used only for a visual representation of the regional variation in protein densities.

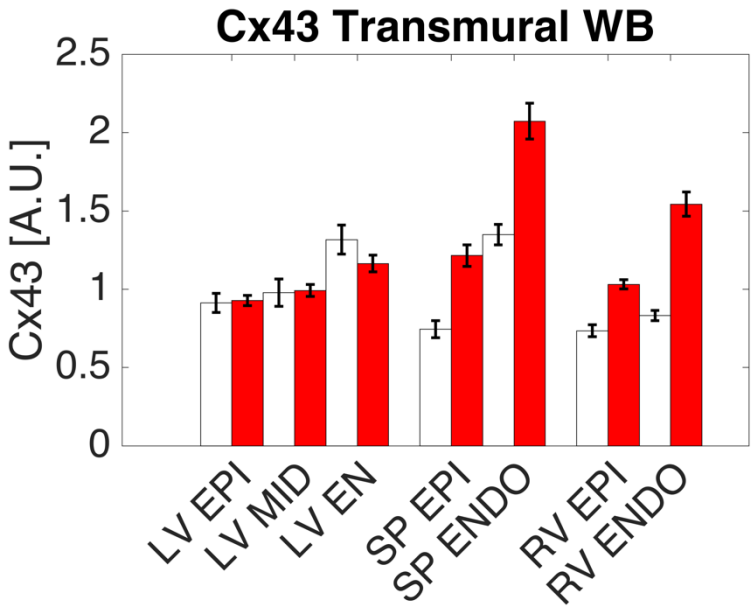

Figure 2.3. Regional variation of Cx43. A consistent transmural gradient can be seen, with increasing Cx43 from EPI to ENDO, consistent with previous studies, though this effect only reached statistical significance in the SP region in the current study. (White = SHAM, Red = TAC)

2.3. Results

2.3.1. Transverse Aortic Constriction (TAC)

Consistent with the results from Chapter 2, at four weeks post-surgery, the systolic pressures in the ascending aorta were significantly elevated in the TAC group compared to SHAM controls (158±2 mmHg TAC vs 108±2 mmHg SHAM, $p<0.0001$). Animals in the TAC group were found to be in a state of compensated hypertrophy, with significantly higher HW/BW ratio (4.44±0.05 g/kg TAC vs 3.57±0.02 g/kg SHAM, $p<0.01$), and a significantly lower, yet still normal, (i.e. >50%) ejection fraction (80±1% SHAM vs. 73±5% TAC, $p<0.01$).

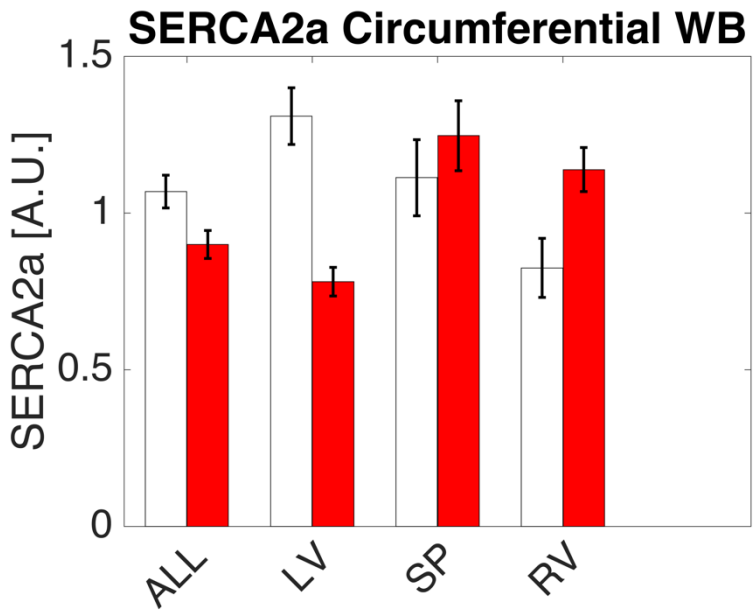

Figure 2.4. Regional distribution of SERCA2a The mean density of SERCA2a in the LV of TAC hearts was significantly lower than SHAM (-40%, $p < 0.01$). This difference was offset by slightly (not significant) higher values in the SP and RV of TAC hearts. (White = SHAM, Red = TAC)

2.3.2. Western Blot

The major results of this study are summarized in **Table 2.1** and **Figures 2.3 - 2.6**. In brief, the overall amount of Cx43 in the rat ventricles was 15% greater in TAC hearts compared to SHAM controls ($p = 0.0163$), but this effect was due mostly to large increases in the SP (57%, $p = 0.077$) and RV (64%, $p = 0.006$) regions, since in the LV (free wall), the total amount of Cx43 was not statistically different between the two groups (-4%, $p = 0.765$). The transmural gradient of Cx43 we observed was consistent between LV, RV, and SP, with increasing amounts of Cx43 from EPI to ENDO. However, this transmural gradient only reached statistical significance in the SP region ($p = 0.037$) **(Figure 2.3)**.

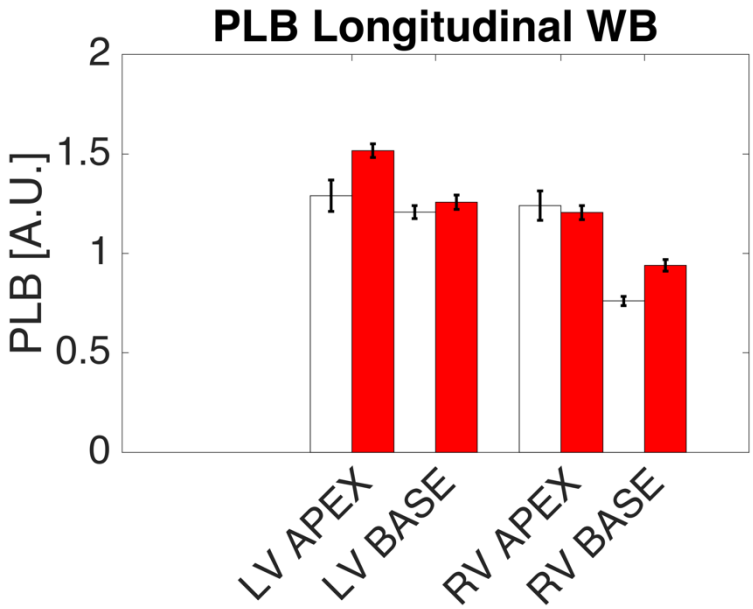

Figure 2.5. Regional distribution of PLB. Mean values were significantly lower in the base than apex of the RV (-26.5%, p = 0.011).
(White = SHAM, Red = TAC)

In the LV region, SERCA2a was significantly lower in TAC hearts vs. SHAM (-40%, p = 0.002), although the effect of this difference over the ventricles as a whole was offset by the greater levels of SERCA2a in TAC vs. SHAM hearts in the SP and RV (12%, p = 0. 765; 38%, p = 0. 246, respectively) **(Figure 2.4)**. Phospholamban (PLB) amounts were significantly lower in the base than apex in the RV (-26.5%, p = 0.011) **(Figure 2.5)**. NCX only differed significantly across regions. The ANOVA does not provide region-by-region statistics, however, so we are left to speculate about which regions were statistically different from each other **(Figure 2.6)**. Perhaps unexpectedly, all other proteins studied showed no significant differences, either across spatial regions or between groups (SHAM vs. TAC).

Somewhat surprisingly, neither MLCK nor PMCA exhibited any differences, either between groups or regions. This could be due to the low signal observed in the bands of these proteins when quantified using western blot **(Figure 2.2)**.

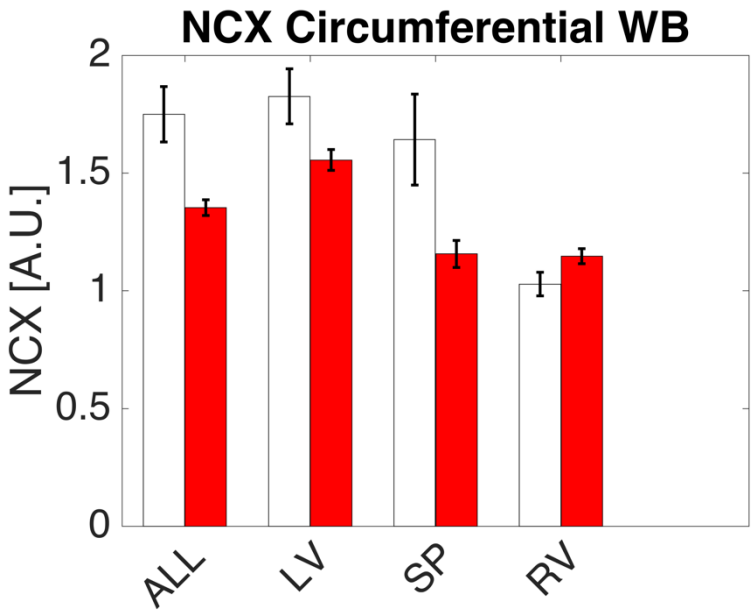

Figure 2.6. Regional distribution of NCX. Mean values were markedly lower in TAC hearts vs. SHAM in the LV and SP regions, but not RV. There was a significant difference between regions, which is indicative of the higher values in the LV and SP than RV. (White = SHAM, Red = TAC)

2.3.3. Immunofluorescence Microscopy of Entire Ventricle Cross-Sections

Figures 2.7 and 2.8 show the regional distributions of Cx43 and SERCA2a, respectively, in representative samples of normal rat LV myocardium. Although attempts were made to quantify regional distributions of Cx43 or SERCA2a density from these cross-section fluorescent images, we struggled to identify a reliable and reproducible method. However, qualitatively, the density of Cx43 did appear slightly higher in EPI regions compared to MID and ENDO. In the case of SERCA2a, the EPI region is very bright, the ENDO region is less so, and the MID region is darkest. This result corresponds well with what we observed using western blot **(Figure 2.4)**, though further studies will be required to

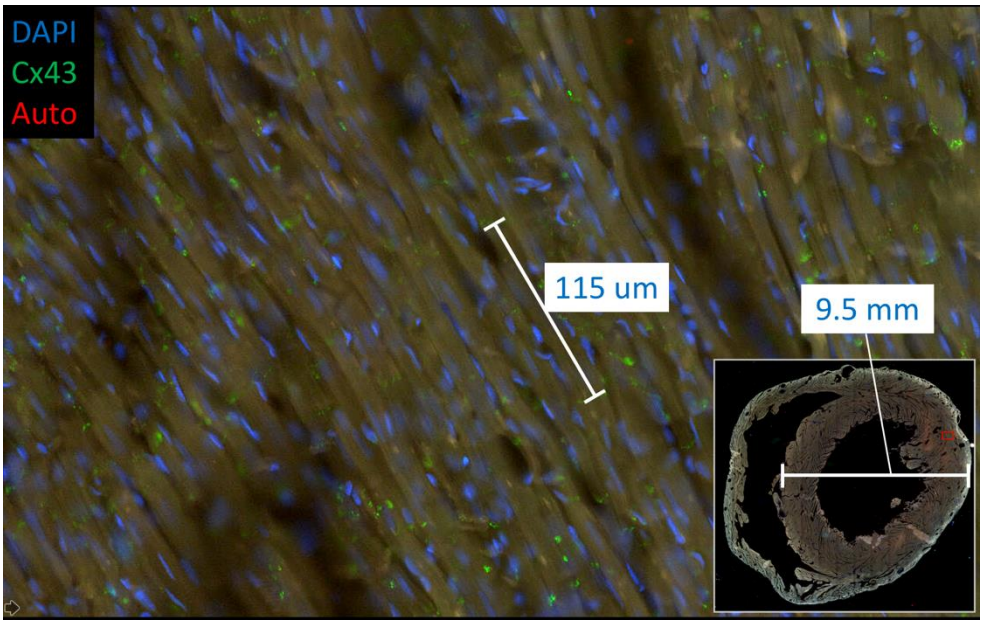

Figure 2.7. Representative cross-sectional image of Cx43 immunofluorescent staining. Cx43 (green) and DAPI (blue) Autofluorescence is observed since there was no fluorescent label in the red color range. Cx43 appear as localized bands at the intercalated discs. Our imaging protocol allows for scanning entire cross-sections in the 10s of mms at high enough resolution to count nuclei or other cellular features.

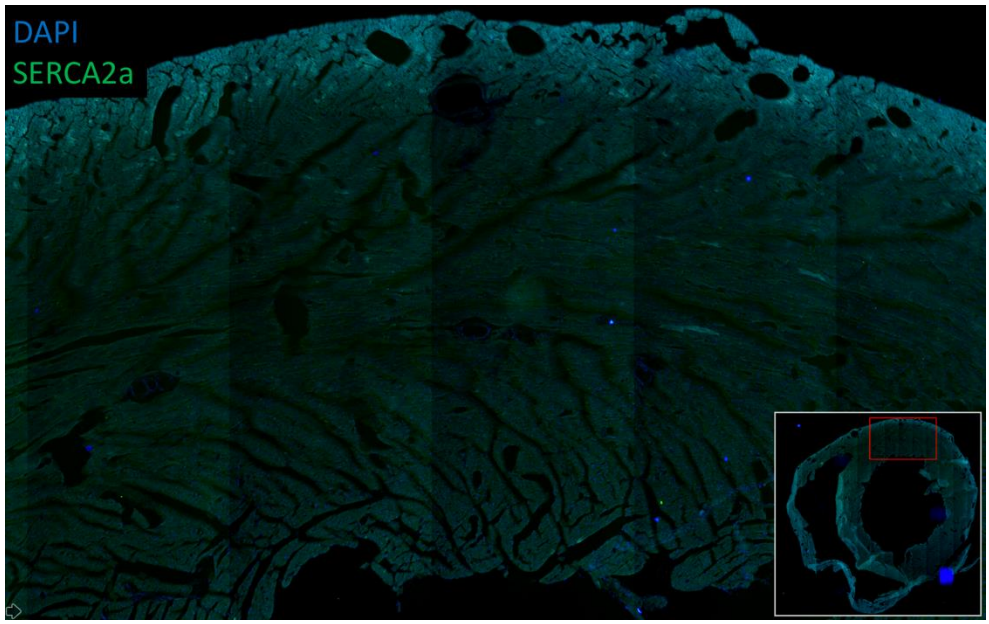

Figure 2.8. Representative cross-sectional image of SERCA2a immunofluorescent staining. SERCA2a (green) DAPI (blue) SERCA2a appears as a diffuse green color but was stronger than autofluorescence in tissues with no green label. The transmural pattern here reflects that observed with western blot.

determine whether the quantitative distribution of these and other proteins differs significantly between regions.

2.4. Discussion

In this work, we have used western blot and fluorescence microscopy of entire ventricle cross-sections to investigate the regional (especially transmural) distribution of protein densities in the rat ventricles after 4 weeks of pressure overload (TAC) and in SHAM controls. We observed several transmural or other regional gradients in these protein densities, as well as differences between TAC and SHAM groups, however, only a few of these achieved statistical significance.

There were mostly favorable comparisons between our data and those reported previously, however there were also some discrepancies that should be addressed. Firstly, the transmural gradient we observed in Cx43 across the ventricle wall, with increasing levels of Cx43 from EPI to ENDO, is very consistent with what has been observed in the dog and mouse [12], [13]. However, Yamada, et al reported no transmural gradient of Cx43 in the rat [12]. However, they used Wistar rats whereas we used Sprague-Dawley, and this may explain the discrepancy.

Our finding that SERCA2a decreases with POH comports with previous studies which showed similar decreases in SERCA2a expression [19]–[21]. The differential response in the right ventricle and septum vs the left ventricle has not to our knowledge been previously reported. Additionally, we are unaware of any report of regional variations in the density distributions of the remaining proteins we investigated herein.

The functional implications of the regional gradients we observed in this study and the spatially heterogeneous remodeling of those structures are quite complex and a simple

explanation would be insufficient. We propose that the above data could be implemented into mathematical models of ventricular mechanics, as has been done previously [22]. Such models would help to elucidate the normal contributions of transmural gradients, and the functional ramifications of regional remodeling in a heart with POH.

2.5. Acknowledgements

The author recognizes the significant contributions of Jennifer Stowe, Younouss Faye, and Melody Dong for their superb experimental work.

2.6. References

[1] J. M. Guccione, K. D. Costa, and A. D. McCulloch, “Finite element stress analysis of left ventricular mechanics in the beating dog heart,” *J. Biomech.*, vol. 28, no. 10, pp. 1167–1177, 1995.

[2] K. R. Laurita, R. Katra, B. Wible, X. Wan, and M. H. Koo, “Transmural heterogeneity of calcium handling in canine,” *Circ. Res.*, vol. 92, no. 6, pp. 668–675, 2003.

[3] J. M. Cordeiro, L. Greene, C. Heilmann, D. Antzelevitch, and C. Antzelevitch, “Transmural heterogeneity of calcium activity and mechanical function in the canine left ventricle,” *Am. J. Physiol. - Hear. Circ. Physiol.*, vol. 286, no. 4, pp. H1471–H1479, 2004.

[4] K. R. Laurita and R. P. Katra, “Delayed afterdepolarization-mediated triggered activity associated with slow calcium sequestration near the endocardium,” *J. Cardiovasc. Electrophysiol.*, vol. 16, no. 4, pp. 418–424, 2005.

[5] T. Anderson, J. Wulfkuhle, E. Petricoin, and R. L. Winslow, “High resolution mapping of the cardiac transmural proteome using reverse phase protein microarrays.,” *Mol. Cell. Proteomics*, vol. 10, no. 7, p. M111.008037, 2011.

[6] Q. Lou, V. V. Fedorov, A. V. Glukhov, N. Moazami, V. G. Fast, and I. R. Efimov, “Transmural heterogeneity and remodeling of ventricular excitation- contraction coupling in human heart failure,” *Circulation*, vol. 123, no. 17, pp. 1881–1890, 2011.

[7] J. Prestle, S. Dieterich, M. Preuss, U. Bieligk, and G. Hasenfuss, “Heterogeneous transmural gene expression of calcium-handling proteins and natriuretic peptides in the failing human heart,” *Cardiovasc. Res.*, vol. 4, no. 4, pp. 323–331, 1999.

[8] A. M. Feldman, E. O. Weinberg, P. E. Ray, and B. H. Lorell, “Selective changes in cardiac gene expression during compensated hypertrophy and the transition to cardiac decompensation in rats with chronic aortic banding.,” *Circ. Res.*, vol. 73, no. 1, pp. 184–192, 1993.

[9] S. E. Campbell, A. M. Gerdes, and T. D. Smith, “Comparison of regional differences in cardiac myocyte dimensions in rats, hamsters, and guinea pigs.,” *Anat. Rec.*, vol. 219, no. 1, pp. 53–9, Sep. 1987.

[10] C. Antzelevitch, S. Sicouri, S. H. Litovsky, A. Lukas, S. C. Krishnan, J. M. Di Diego, G. a. Gintant, and D. W. Liu, “Heterogeneity Within the Ventricular Wall,” *Circ. Res.*, vol. 69, no. 6, pp. 1427–1449, 1991.

[11] J. S. Davis, S. Hassanzadeh, S. Winitsky, H. Lin, C. Satorius, R. Vemuri, A. H. Aletras, H. Wen, and N. D. Epstein, “The overall pattern of cardiac contraction

depends on a spatial gradient of myosin regulatory light chain phosphorylation," *Cell*, vol. 107, no. 5, pp. 631–641, 2001.

[12] K. A. Yamada, E. M. Kanter, K. G. Green, and J. E. Saffitz, "Transmural distribution of connexins in rodent hearts," *J. Cardiovasc. Electrophysiol.*, vol. 15, no. 6, pp. 710–715, 2004.

[13] S. Poelzing, F. G. Akar, E. Baron, and D. S. Rosenbaum, "Heterogeneous connexin43 expression produces electrophysiological heterogeneities across ventricular wall.," *Am. J. Physiol. Heart Circ. Physiol.*, vol. 286, no. 5, pp. H2001–H2009, 2004.

[14] C. S. McLachlan, P. R. Jusuf, N. Rummery, S. K. Kummerfeld, B. Hambly, M. A. McGuire, and V. Turner, "Tyramide signal amplification enhances the detectable distribution of connexin-43 positive gap junctions across the ventricular wall of the rabbit heart.," *Arch. Histol. Cytol.*, vol. 66, no. 4, pp. 359–65, Oct. 2003.

[15] S. Poelzing and D. S. Rosenbaum, "Altered connexin43 expression produces arrhythmia substrate in heart failure.," *Am. J. Physiol. Heart Circ. Physiol.*, vol. 287, no. 4, pp. H1762-70, 2004.

[16] S. Kostin, S. Dammer, S. Hein, W. P. Klovekorn, E. P. Bauer, and J. Schaper, "Connexin 43 expression and distribution in compensated and decompensated cardiac hypertrophy in patients with aortic stenosis," *Cardiovasc. Res.*, vol. 62, no. 2, pp. 426–436, 2004.

[17] B. C. Schwab, G. Seemann, R. A. Lasher, N. S. Torres, E. M. Wulfers, M. Arp, E. D. Carruth, J. H. B. Bridge, and F. B. Sachse, "Quantitative analysis of cardiac tissue including fibroblasts using three-dimensional confocal microscopy and image reconstruction: Towards a basis for electrophysiological modeling," *IEEE Trans. Med. Imaging*, vol. 32, no. 5, pp. 862–872, 2013.

[18] C. A. Schneider, W. S. Rasband, and K. W. Eliceiri, "NIH Image to ImageJ: 25 years of image analysis," *Nat. Methods*, vol. 9, no. 7, pp. 671–675, 2012.

[19] D. De La Bastie, D. Levitsky, L. Rappaport, J. J. Mercadier, F. Marotte, C. Wisnewsky, V. Brovkovich, K. Schwartz, and a M. Lompré, "Function of the sarcoplasmic reticulum and expression of its Ca2(+)-ATPase gene in pressure overload-induced cardiac hypertrophy in the rat.," *Circ. Res.*, vol. 66, no. 2, pp. 554–564, 1990.

[20] M. Anger, A. M. Lompré, O. Vallot, F. Marotte, L. Rappaport, and J. L. Samuel, "Cellular distribution of Ca2+ pumps and Ca2+ release channels in rat cardiac hypertrophy induced by aortic stenosis.," *Circulation*, vol. 98, no. 22, pp. 2477–86, Dec. 1998.

[21] K. Wong, K. R. Boheler, M. Petrou, and M. H. Yacoub, "Pharmacological Modulation

of Pressure-Overload Cardiac Hypertrophy : Changes in Ventricular Function, Extracellular Matrix, and Gene Expression," *Circulation*, vol. 96, no. 7, pp. 2239–2246, Oct. 1997.

[22] S. G. Campbell, E. Howard, J. Aguado-Sierra, B. a Coppola, J. H. Omens, L. J. Mulligan, A. D. McCulloch, and R. C. P. Kerckhoffs, "Effect of transmurally heterogeneous myocyte excitation-contraction coupling on canine left ventricular electromechanics.," *Exp. Physiol.*, vol. 94, no. 5, pp. 541–552, 2009.

3. Regional Variations in Diffusion Tensor Anisotropy are Associated with Myocyte Remodeling in Left Ventricular Pressure Overload

3.1. Introduction

Nearly one half of adults in the United States has hypertension [1]. The well-known response in the left ventricle (LV) to such pressure overload is concentric hypertrophy, which is characterized by the addition of sarcomeres in parallel within cardiac myocytes, resulting in ventricle wall thickening without chamber dilation. Such remodeling in pressure overload hypertrophy (POH) is considered a compensatory mechanism to maintain cardiac output despite increased downstream resistance to blood flow. This compensatory state, however, results in impaired diastolic filling, and often progresses to wall thinning, chamber dilation, impaired systolic function, and heart failure [2]–[4].

Many studies have described effects of pressure overload on structural features, e.g. myocyte hypertrophy, laminar sheet architecture, proteins (both myocyte and ECM), signaling, and gene expression networks [4]–[10]. However, it is unclear whether remodeling of these structural features during POH occurs uniformly in all regions of the LV. Several structural features in the normal LV have been shown to vary spatially, especially transmurally, in normal hearts [11]. These transmural gradients, together with other factors, are thought to contribute to normalizing the otherwise large gradients in "fiber" (parallel to myocytes) stress and strain during both diastolic filling and systolic contraction [11]–[16].

For example, Campbell, et al observed a transmural gradient in myocyte geometry in isolated cells from normal hearts, with larger myocyte volume and cross-sectional area (CSA) in the sub-endocardium (ENDO) than midwall (MID) or sub-epicardium (EPI) [17]. In POH, this transmural gradient was "abolished" [18]. Conversely, Omens, et al showed that in intact,

fixed tissue, a transmural gradient in myocyte CSA only appeared after 3 weeks of aortic constriction, with increasing myocyte CSA towards ENDO [19]. Finally, McCrossan, et al reported a transmural gradient in myocyte geometry similar to that of Campbell, et al in normal hearts, but in POH, the gradient increased slightly, as opposed to being "abolished" [20]. These conflicting results could be due to differences in loading conditions, different strains of rat, experimental processes such as fixation, or other factors. Regardless, further study is required to elucidate the transmural variation in myocyte geometry in normal hearts and in those with POH.

We [11] and others [16], [21] have summarized how transmural gradients in LV structures likely contribute to uniform fiber strain during diastole and systole, resulting in optimized ventricular function. Thus, it has been argued that uniform fiber strain is an important homeostatic principle in maintaining cardiac function, and therefore as myocardium grows and remodels due to chronic overloads, it will attempt to keep regional heterogeneity in fiber strain to a minimum. It has been shown that ventricular torsion, driven by the transmural variation in fiber angle, is a requirement for uniformity of fiber stress and strain (review by Russel, et al [22]). However, it is unclear whether this uniformity is actually preserved in POH due to the quantity of structural features that remodel, and the complexity with which individual structural components contribute to mechanics. It has also been shown that torsion, which is driven mainly by epicardial myocytes, is increased in POH [23]–[25]. Additionally, a distinct relationship between torsion and ventricle geometry has been shown wherein torsion increases with a decrease in the ratio of cavity area to wall area [26]. In this study, the observed increase in torsion during endocardial ischemia was explained by a decrease in endocardial shortening strain, exaggerating the contribution of orthogonally-oriented

epicardial regions [27]. Conversely, in pressure overload, it may be that epicardial shortening strain must increase to maintain optimal torsion and cardiac output despite the increased load. Therefore, we hypothesized that the structural remodeling response to pressure overload varies transmurally, including greater myocyte hypertrophy in EPI than in ENDO.

Measuring variations in these structural features is not trivial and usually involves tissue sectioning, staining, imaging, and careful measurement. Not only is this time-consuming and tedious, but such experiments cannot be performed in vivo, are destructive, and are usually only performed in small sub-regions of an organ or tissue. Non-destructive imaging is a much more appealing approach, especially methods which can relatively quickly and accurately capture the information in the entire organ or tissue of interest, while preserving 3D geometry. Diffusion tensor MRI (DT-MRI or DTI) has surfaced as one such technique to measure local structural orientations from eigenvectors, such as the local myocyte orientation described by the "helix" or "fiber" angle, and the laminar "sheet(let)" orientation described by the sheet angle [28]–[30]. The diffusion tensor not only provides orientation information in its eigenvectors, but also the apparent diffusivities along those eigenvectors in the eigenvalues. Some recent studies have described transmural variations in fractional anisotropy (FA), which is derived from the eigenvalues and indicates the degree of self-diffusion anisotropy [31]–[33]. Others have shown an increase in cross-fiber diffusivities and sheet reorientation in heart failure patients [34], [35]. These results are also somewhat conflicting and unclear, and even less well understood are the contributions of different structural features to variations in 3D diffusivity. Thus, a secondary objective of this study was to determine whether regional and pathophysiological variations in these structural features could be detected consistently using DT-MRI.

To test our hypothesis, we performed high-resolution, high-fidelity DT-MRI on transverse aortic constricted (TAC) and sham control (SHAM) rat hearts ex vivo, and investigated the regional variations in DTI-derived parameters of orientation, diffusivity, and anisotropy in the LV. In the same hearts, we performed quantitative measurements of myocyte orientations and dimensions from bright field and confocal microscope images, respectively, to corroborate our findings from DT-MRI and suggest potential structural contributors to regional variation in the DT-MRI signal. We found that there are indeed regional variations in myocyte geometry and structural organization which become more uniform in POH. Additionally, several structural features correlated significantly with DTI-derived parameters, regardless of phenotype. This remodeling and the association with DTI are quite complex. Nonetheless, these results will be valuable in understanding the mechanisms by which cardiac myocytes in different regions of the LV respond to hypertension and may provide a tool for diagnosing the early stages of hypertrophy or other remodeling clinically and non-invasively, allowing for earlier lifestyle changes or interventions to reverse early stage remodeling before the progression to heart failure occurs.

3.2. Methods

3.2.1. Pressure Overload Hypertrophy Model and Tissue Preparation

All animal studies were approved by the Institutional Animal Care and Use Committee at UCSD and followed the Guide for the Care and Use of Laboratory Animals. 16 male rats weighing approximately 200 grams were randomly divided equally into TAC and SHAM groups. Rats were intubated and anesthetized with 1.25-2.00% isoflurane in air. An appropriate level of anesthesia was confirmed by toe pinch. Once sufficiently anesthetized, a small incision was made to expose the ascending aorta. In TAC animals, a hemo-clip was

inserted between the right innominate and left carotid arteries, then constricted to a width of 0.5 mm. SHAM controls underwent the same procedure but did not have the clip inserted. The incision layers were closed and sutured, and the animal was allowed to recover fully.

M-mode echocardiography was performed 1 day before surgery, and at 2 weeks and 4 weeks after surgery. At 4 weeks, manometer (Millar, Houston, TX, USA) catheter recordings of aortic (proximal to the clip) and LV cavity pressures as well as concurrent electrocardiogram were also recorded. Hearts were then excised, weighed, and retrograde perfused with Krebs-Henseleit buffer until the tissue was cleared of blood and regular beating resumed. Cardiac arrest was achieved using a modified Krebs-Henseleit buffer with high potassium, and hearts were then fixed using Karnovsky's fixative with 2mM gadolinium chelate (ProHance; Bracco, Eden Prairie, Minnesota, USA). For imaging, hearts were embedded in a 1% agarose gel containing 2mM gadolinium chelate. A subset of these hearts was used in a previously published imaging study [36].

3.2.2. Diffusion Tensor MRI Acquisition

Images were acquired in a similar fashion to previously published data, with some modification [37]. Briefly, a 9.4 Tesla MRI magnet (Agilent, CA, USA) capable of a maximum gradient strength of 1 T/m was used, together with a 20 mm inner diameter birdcage coil (Rapid Biomedical, Rimpar, Germany). Important imaging parameters were as follows: TR = 250 ms, TE = 9.3 ms, echo spacing = 4.9 ms, echo train length = 8, FOV = 21.6×14.4×14.4 mm, resolution = 100×100×100 μm, number of non-DW (b=0) images = 4, number of DW directions = 30 forward + 30 reverse, $b_{effective}$ = 1,000 s/mm^2, diffusion duration (δ) = 2 ms, diffusion time (Δ) = 5.5 ms. Total acquisition time per heart was 11.5 h.

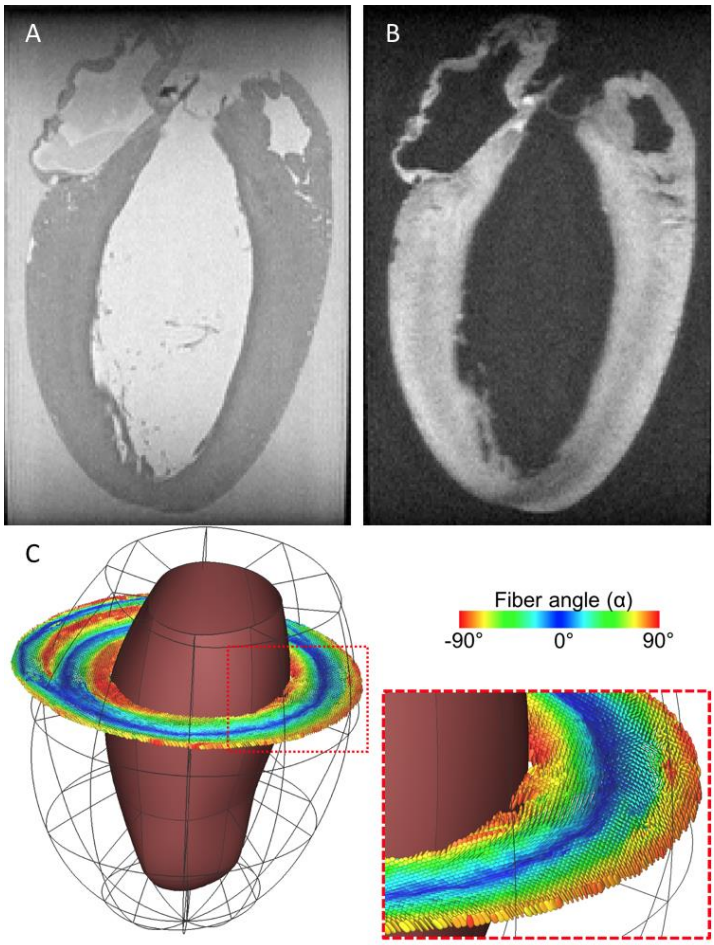

Figure 3.1. DT-MRI of rat ventricles. (A) Non-diffusion weighted (b=0) image shows high SNR of the myocardium (33 ± 4 for all animals). **(B)** Example diffusion-weighted image. SNR for weighted images for all rats was 24 ± 4. **(C)** Diffusion tensors are rendered as glyphs whose color represents the orientation of the primary eigenvector (longitudinal tensors are red, circumferential are blue).

3.2.3. Tissue Sectioning, Staining, and Confocal Microscopy

After DT-MRI, whole heart samples were dissected into three sections after removal of the atria and valve plane: the right ventricle, interventricular septum, and LV free wall. Samples from the equatorial LV free wall were dehydrated in graded ethanol and embedded in paraffin wax for sectioning. Serial sections at 50 μm thickness were obtained parallel to the EPI through the entire ventricular wall using a microtome and mounted on slides. The staining protocol was similar to that described by Bensley, et al, but without the DAPI stain [38]. After

wax removal and rehydration, tissue sections were stained with wheat germ agglutinin (WGA) conjugated to Alexa Fluor 633 (Life Technologies, Carlsbad, California, USA). A Zeiss LSM 880 with Airyscan FAST (Zeiss, Jena, Germany) was used to acquire image volumes in FAST mode. Image stacks were acquired with the following settings: Objective = 20x Pln/Apo, NA = 0.8, resolution = 0.2×0.2×0.4 μm, typical image size = 1220×1220×(80-130) voxels.

Bright-field images were also obtained of the same sections at low magnification (10X) on an EVOS FL Auto Microscope (Life Technologies, Thermo Fisher Scientific, Waltham, MA) to measure fiber angles and dispersions. Fiber angles and dispersions were measured using the image gradient technique described by Karlon, et al [39] implemented in-house in MATLAB (The MathWorks, Natick, MA). The fiber angle and dispersion for a given section were defined as the circular mean and circular standard deviation of detected edges.

3.2.4. Image Processing, Registration, Mesh Generation, and Parameter Calculation

Diffusion Tensor MRI Processing

Diffusion tensors were calculated from diffusion weighted images in AFNI [40] by solving the standard monoexponential, Gaussian model:

$$\frac{S(b)}{S(0)} = \exp(-bD_a)$$

where b is the b-value [s/mm2] indicating the combined magnitude and duration of the diffusion gradient, $S(b)$ is the diffusion-weighted image signal, $S(0)$ is the non-weighted image (b=0), and D_a is the apparent diffusion coefficient [mm^2/s].

Masks were generated by semi-automatic segmentation of the LV from b=0 images in Seg3D (SCI Institute, University of Utah, Salt Lake City, Utah). Papillary muscles and trabeculae were excluded from the segmentation. Segmented masks were converted into mesh surfaces, which were then divided into endocardial and epicardial surfaces and smoothed in Blender. An affine transformation was applied to align each data set with a consistent "cardiac" reference frame. The same affine transformation was applied to the calculated diffusion tensors using the log-Euclidian transform to preserve tensor properties [41]. A prolate spheroidal mesh template with 40 elements was fitted via least-squares to the LV endocardial and epicardial surfaces. This mesh served as a consistent datum across all hearts by which to measure local fiber and sheet angles from the eigenvectors, and to simply and consistently subdivide the tensor data by anatomical region (circumferential, longitudinal, and transmural position) for direct regional comparisons across all hearts. An example mesh with rendered diffusion tensors in a single image slice are shown in **Figure 3.1C**.

The eigenvectors from DT-MRI have been shown to agree closely with the local fiber, sheet, and sheet-normal orientations, respectively, and the eigenvalues represent the apparent diffusion coefficients along those principal directions [28], [30], [42]. Fiber and sheet angles were calculated as previously described [43]. Briefly, the fiber ("helix") angle was defined as the angle between the local circumferential direction and the projection of the primary eigenvector onto the circumferential-longitudinal plane. The sheet angle was defined as the angle between the local radial direction and the secondary eigenvector. The dispersions of these angles were defined as the circular standard deviation of the angles in each spatial region. The fiber, sheet, and sheet-normal diffusivities are the primary, secondary, and tertiary eigenvalues, $(\lambda_1, \lambda_2, \lambda_3)$ respectively. The mean diffusivity (MD) is the mean of the three

eigenvalues. Fractional (FA), linear (CL), planar (CP), and spherical (CS) anisotropies were calculated from the eigenvalues, and their mean ($\hat{\lambda}$) as described previously [44], [45]:

$$FA = \sqrt{\frac{3}{2}}\sqrt{\frac{(\lambda_1 - \hat{\lambda})^2 + (\lambda_2 - \hat{\lambda})^2 + (\lambda_3 - \hat{\lambda})^2}{(\lambda_1^2 + \lambda_2^2 + \lambda_3^2)}}$$

$$CL = \frac{\lambda_1 - \lambda_2}{3\hat{\lambda}}$$

$$CP = \frac{2(\lambda_2 - \lambda_3)}{3\hat{\lambda}}$$

$$CS = \frac{\lambda_3}{3\hat{\lambda}}$$

Confocal Micrograph Processing and Myocyte Geometry

Confocal images were processed using Zeiss Airyscan Processing. Measurements were made of myocyte length, in-plane (parallel to the epicardial surface) myocyte width, and through-plane myocyte height. Lengths were defined as the longest dimension of the myocyte. Width and height were measured across visible nuclei, or across the largest cross-section if no nucleus was visible. Aspect ratios were also computed for length:width ratio (L:W), length:height (L:H), and width-height (W:H). CSA was computed assuming an elliptical cross-section, with major and minor radii defined as half the width and height, respectively. Additionally, myocyte fractional anisotropy (MFA), analogous to FA from DTI, was calculated as:

$$MFA = \sqrt{\frac{3}{2}}\sqrt{\frac{(l - \hat{d})^2 + (w - \hat{d})^2 + (h - \hat{d})^2}{(l^2 + w^2 + h^2)}}$$

where $\hat{d}$ is the mean of myocyte length (l), width (w), and height (h).

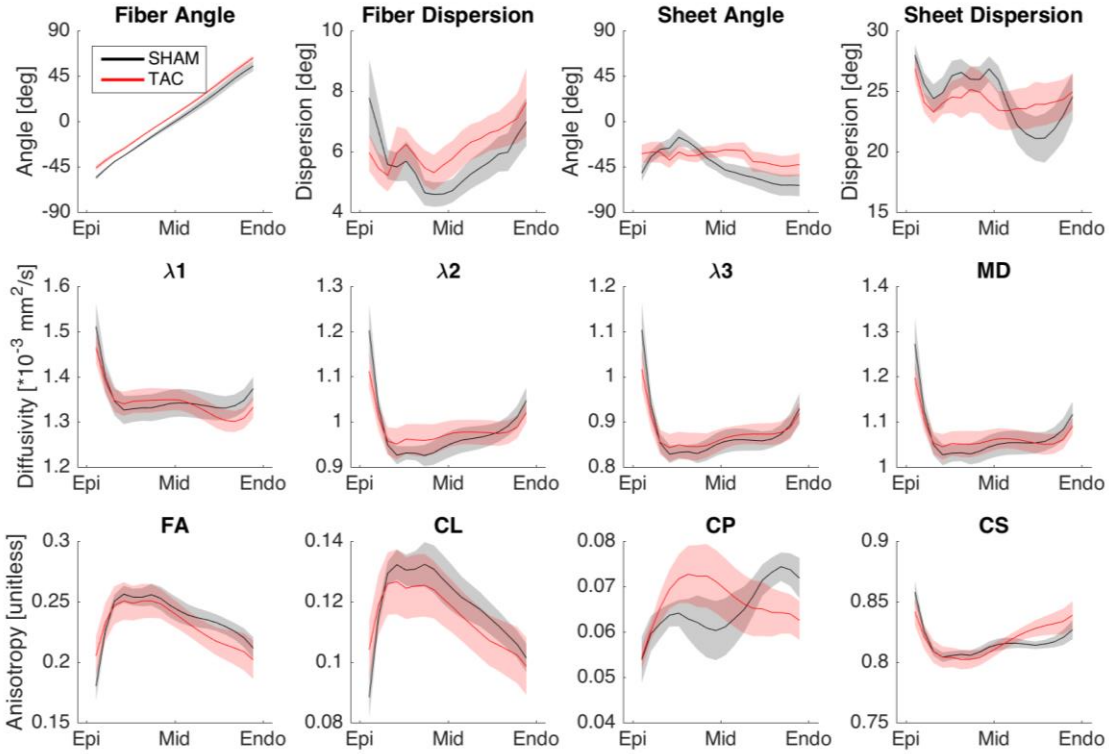

Figure 3.2. Transmural gradients of DTI-derived parameters in the LV free wall. Data shown are mean ± SEM (n=16 SHAM, 16 TAC). Of note are the apparent increase in fiber angle across the wall in this region in TAC vs. SHAM, The transmural patterns of FA and slight decrease in FA in the ENDO, the differential patterns of CP between TAC and SHAM, and the corresponding differences in sheet dispersion.

3.2.5. Statistics

All descriptive statistics in this work comparing SHAM and TAC groups are reported as mean ± SEM. For all statistical inference tests, p-values < 0.05 were considered statistically significant. Student's unpaired, two-tailed t-test with assumed unequal variances was used to test for significance in differences between TAC and SHAM hypertrophic signals, such as heart weight to body weight ratio (HW/BW) and ejection fraction (EF).

The DT-MRI data from each LV were divided into 600 anatomically registered regions (20 transmurally, 10 circumferentially, and 3 longitudinally). A multi-factor ANOVA

for all variables was conducted, with surgical intervention, transmural, circumferential, and longitudinal positions as the four factors. Only between-group differences and the direct linear interactions between factors were considered. Correction for multiple comparisons was performed using the Tukey-Kramer method. For visualization, DT data were divided into 5400 regions (20 transmurally, 30 circumferentially, 9 longitudinally). Group means and the normalized difference between groups (analogous to a t-score) was calculated for each of the 5400 regions. Maps of these values are shown in **Figure 3.3** and in the supplement.

For correlations between parameters measured from DT-MRI and measurements from microscope images, Pearson's correlation coefficient was calculated, along with the p-value for the linear correlation. A random permutation test with 10,000 permutations was performed to correct for multiple comparisons. Once significant correlations were found, analysis of covariance was applied to determine the relative contributions to correlation from the SHAM and TAC groups.

3.3. Results

3.3.1. Transverse Aortic Constriction and Left Ventricular Hypertrophy

At four weeks post-surgery, the systolic pressures in the ascending aorta were significantly elevated in the TAC group compared to SHAM controls (186 ± 33 mmHg TAC vs 118 ± 9 mmHg SHAM, $p<0.01$). Animals in the TAC group were found to be in a state of compensated hypertrophy, with significantly higher heart weight to body weight ratio (4.91 ± 0.45 g/kg TAC vs 3.42 ± 0.16 g/kg SHAM, $p<0.001$), and a significantly lower, yet still normal, (i.e. >50%) EF (79±1% SHAM vs. 72±2% TAC, $p<0.01$). **Table 3.1** summarizes the key differences found between SHAM and TAC hearts.

Table 3.1. Summary of echocardiographic data

Cardiac phase	Variable	Units	SHAM (N=8)	TAC (N=8)	p-value
End-diastole	IVS	[mm]	1.15±0.02	1.47±0.03	<0.001
	LVID	[mm]	7.80±0.19	8.13±0.22	0.30
	LVPW	[mm]	1.50±0.07	2.00±0.12	<0.01
	PAo	[mmHg]	85±2	77±4	0.11
End-systole	IVS	[mm]	1.51±0.10	1.80±0.11	0.10
	LVID	[mm]	4.45±0.15	5.09±0.21	<0.05
	LVPW	[mm]	2.53±0.10	2.94±0.12	<0.05
	PAo	[mmHg]	118±3	186±11	<0.001
--	FS	[%]	43±1	37±1	<0.01
	EF	[%]	79±1	72±2	<0.01
	CO	[L/min]	0.29±0.02	0.28±0.02	0.92
	BW	[g]	334±8	324±6	0.36
	HW	[g]	1.14±0.02	1.59±0.04	<0.001
	HW/BW	[g/kg]	3.42±0.05	4.91±0.15	<0.001

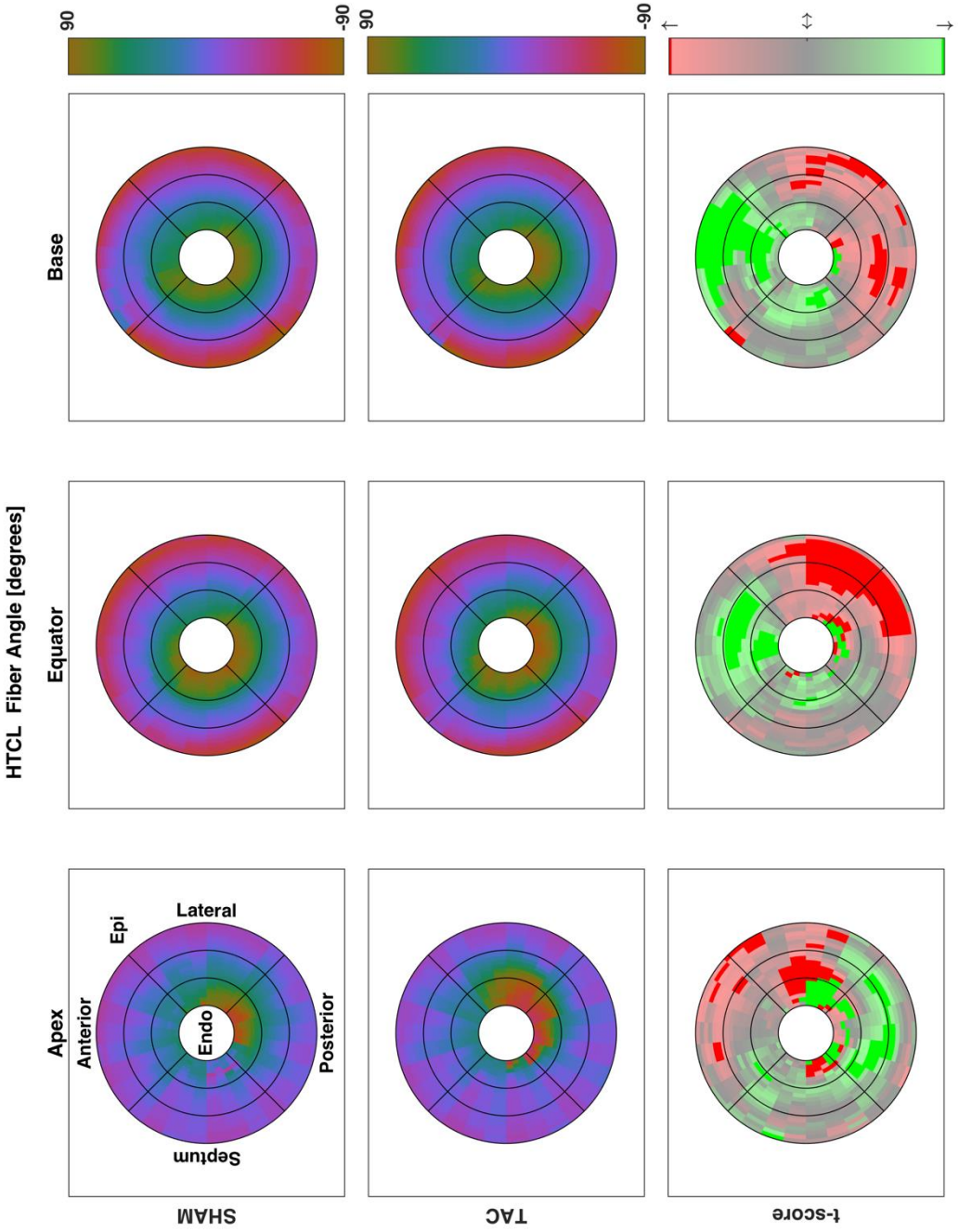

Figure 3.3. Regional variations in select DTI-derived parameters. The comparison between fiber angles in SHAM (top row) and TAC (middle row) animals is indicated by the t-score (bottom row). The data from the LV equatorial lateral wall (in the right-hand side of the circles in the middle column) are also represented in **Figure 3.2. Figure 3.3** continues on the following page.

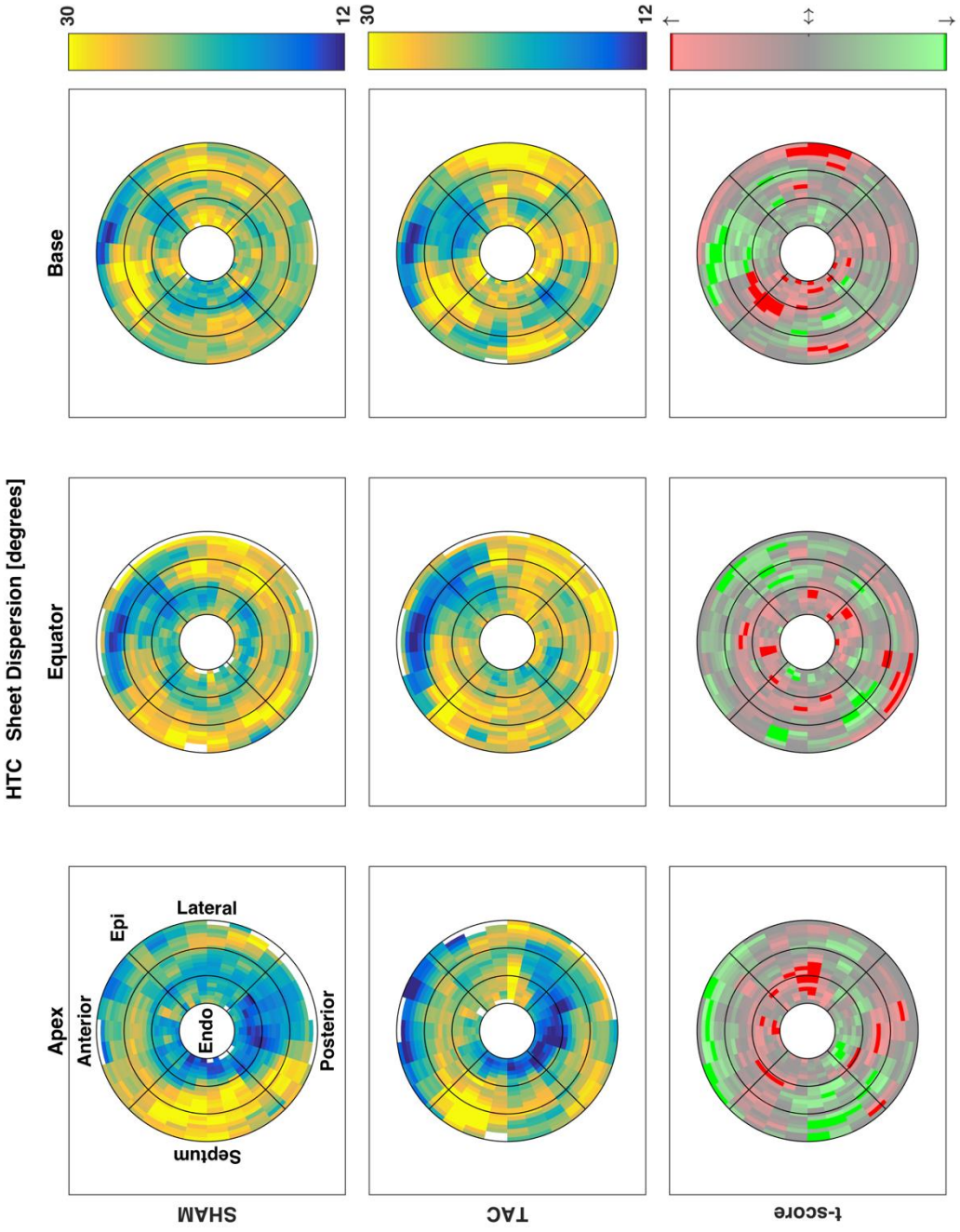

Figure 3.3. (Continued) Regional variations in sheet dispersion. **Figure 3.3** continues on the following page.

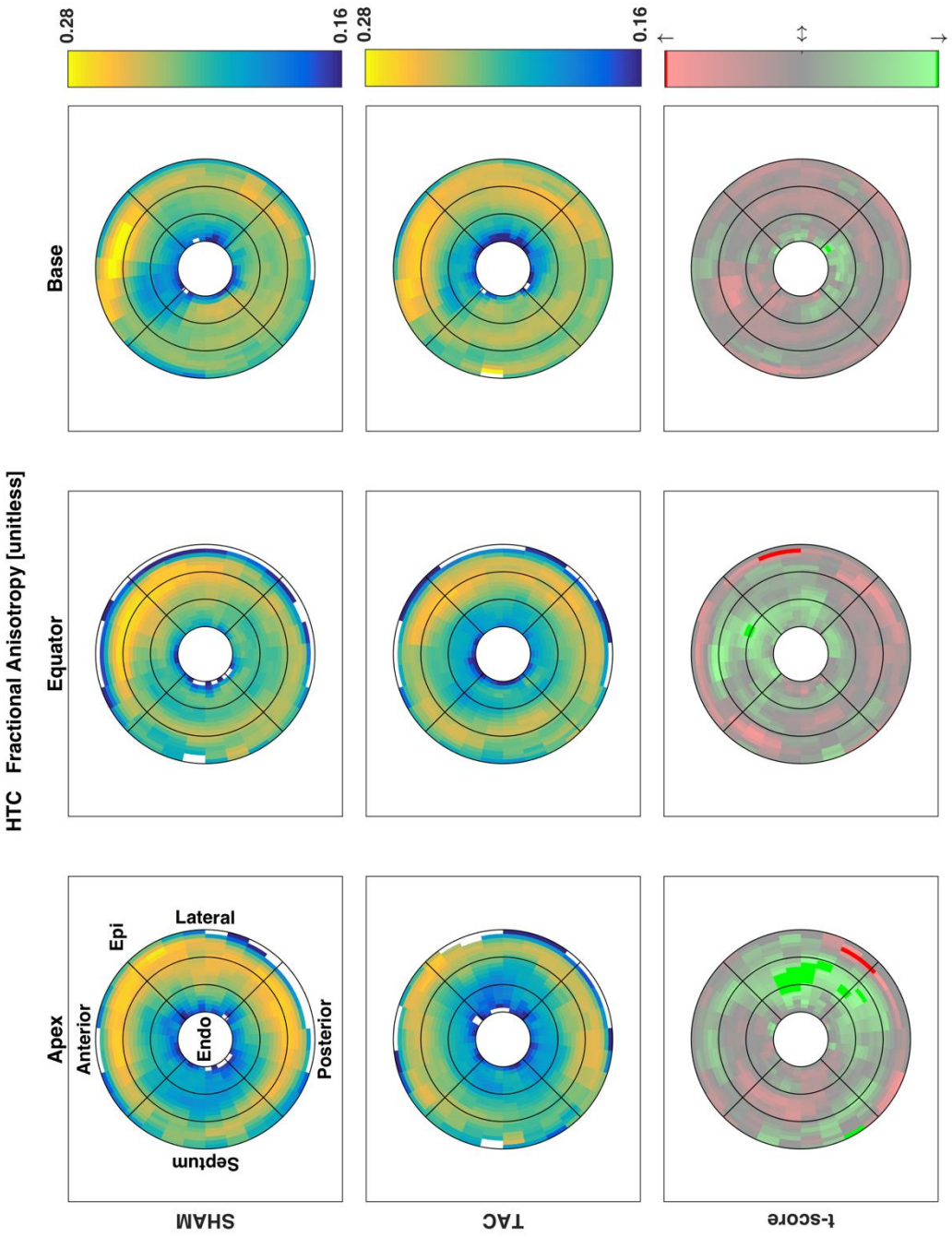

Figure 3.3. (Continued). Regional variations in fractional anisotropy (FA). **Figure 3.3** continues on the following page.

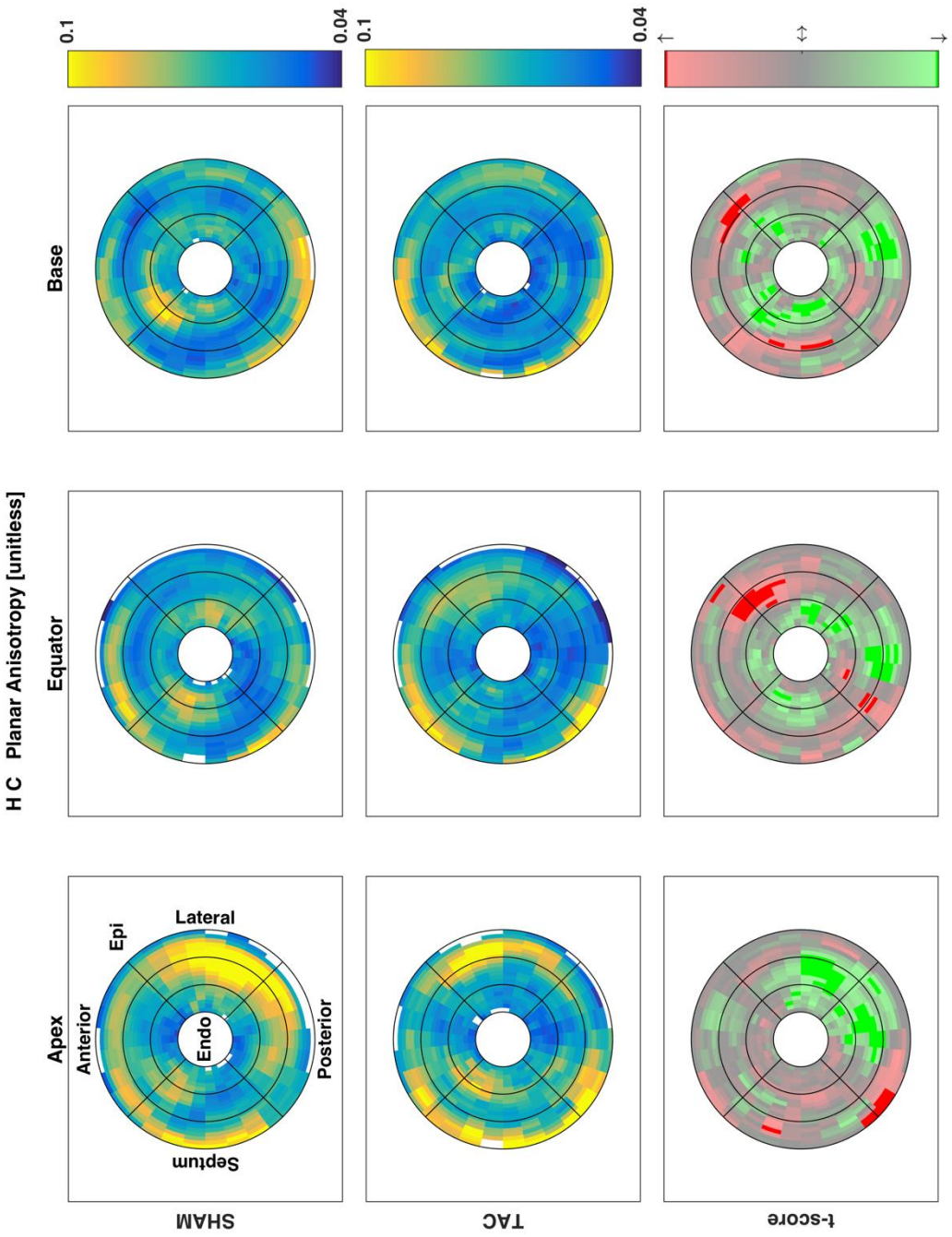

Figure 3.3. (Continued) Regional variations in planar anisotropy (CP).

3.3.2. Diffusion Tensor MRI

The mean (± standard deviation) signal to noise ratio (SNR) of the b=0 images across all hearts was 33±4, where the SNR for each heart was defined as

$$SNR = \frac{\bar{I}_{sig}}{\sigma_{bkg}}$$

where $\bar{I}_{sig}$ is the mean intensity of voxels in a region of myocardium, and σ_{bkg} is the standard deviation of voxel intensities in a region of background signal. In diffusion weighted images, the mean SNR across all animals was 24 ± 4. Representative b=0 and diffusion weighted images are displayed in **Figure 3.1A-B**. **Figure 3.2** shows the transmural distributions of the twelve major variables discussed in this work in the equatorial LV lateral wall. Notably, the fiber angles in this region were consistently slightly higher in TAC animals compared to SHAM controls by approximately 7-8 degrees at all points across the wall. In the opposite (septal) wall, fiber angles were practically identical across the wall, except in the epicardial region, where fiber angles were slightly lower in TAC animals compared to SHAM controls **(Figure 3.3)**. Also of interest is the transmural variation in planar anisotropy (CP) and sheet dispersion.

The regional analysis of diffusion tensor-derived parameters produced several other interesting results, which are summarized in **Table 3.2**. Regional variations in some key variables of SHAM and TAC hearts, as well as the normalized difference between the groups, are shown in **Figures 3.3**. The main differences found between SHAM and TAC groups were as follows: The fiber angle was significantly different in both the mean and the interactions transmurally, circumferentially, and longitudinally, and was apparently slightly higher in the posterolateral EPI (i.e. more circumferential), and slightly lower in the anterior

Table 3.2. ANOVAs for DT-MRI parameter regional variation

Variable	Hypertrophy	Hyp*Trans	Hyp*Circ	Hyp*Long
Fiber Angle	<0.001	<0.001	<0.001	<0.01
Fiber Dispersion	<0.001	<0.001	<0.01	<0.001
Sheet Angle	<0.01	0.19	<0.001	<0.001
Sheet Dispersion	<0.001	<0.01	<0.05	<0.001
Fiber Diffusivity (λ_1)	0.559	--	--	--
Sheet Diffusivity (λ_2)	0.449	--	--	--
Sheet-Normal Diffusivity (λ_3)	<0.05	<0.05	0.568	0.994
MD ($\hat{\lambda}$)	0.187	--	--	--
FA	<0.01	<0.001	0.697	<0.001
CL	0.388	--	--	--
CP	<0.001	<0.001	0.89	0.24
CS	<0.001	<0.001	0.75	<0.001

Table 3.3. ANCOVAs for correlations between DT-MRI and histological measurement

DTI Parameter	Histo Parameter	Best ANCOVA	R^2	Correlation p-value	ANCOVA p-value(s)
Fiber Angle	Fiber Angle	Same Line	0.71	<<0.001 (6e-9)	
	L:W	Same Line	0.23	0.0073	
Fiber Dispersion	Fiber Angle	Parallel Lines	0.23	0.0078	0.0063/0.0008
	Myocyte Width	Same Line	0.31	0.0013	
	L:W	Separate Lines	0.30	0.0019	0.0363/0.0046
Sheet Dispersion	Fiber Angle	Same Line	0.20	0.0130	
	L:H	Same Line	0.25	0.0049	
Fiber Diffusivity	Fiber Angle	Separate Lines	0.27	0.0036	0.0121/0.0025
Sheet Diffusivity	W:H	Same Line	0.21	0.0112	
MD	W:H	Same Line	0.25	0.0053	
FA	Fiber Angle	Same Line	0.48	<0.001 (2e-5)	
CL	Fiber Angle	Same Line	0.56	<0.001 (2e-6)	
CP	Fiber Angle	Same Line	0.27	0.0032	
	L:W	Same Line	0.24	0.0062	
	MFA	Same Line	0.24	0.0057	
CS	Fiber Angle	Same Line	0.26	0.0038	

ENDO (also more circumferential) in TAC vs SHAM. The sheet dispersion was lower on average in TAC hearts compared to SHAM, and the interactions with transmural,

circumferential, and longitudinal position were also significant. Although the diffusivities alone did not show much collective significance in the ANOVA, there was an apparent transmural-longitudinal shift in all three, with lower diffusivities in ENDO and apical regions in TAC vs SHAM. There was a notable transmural gradient of FA in both SHAM and TAC hearts, and this value appeared to decrease in the ENDO and apical regions, whereas it was increased elsewhere in TAC hearts.

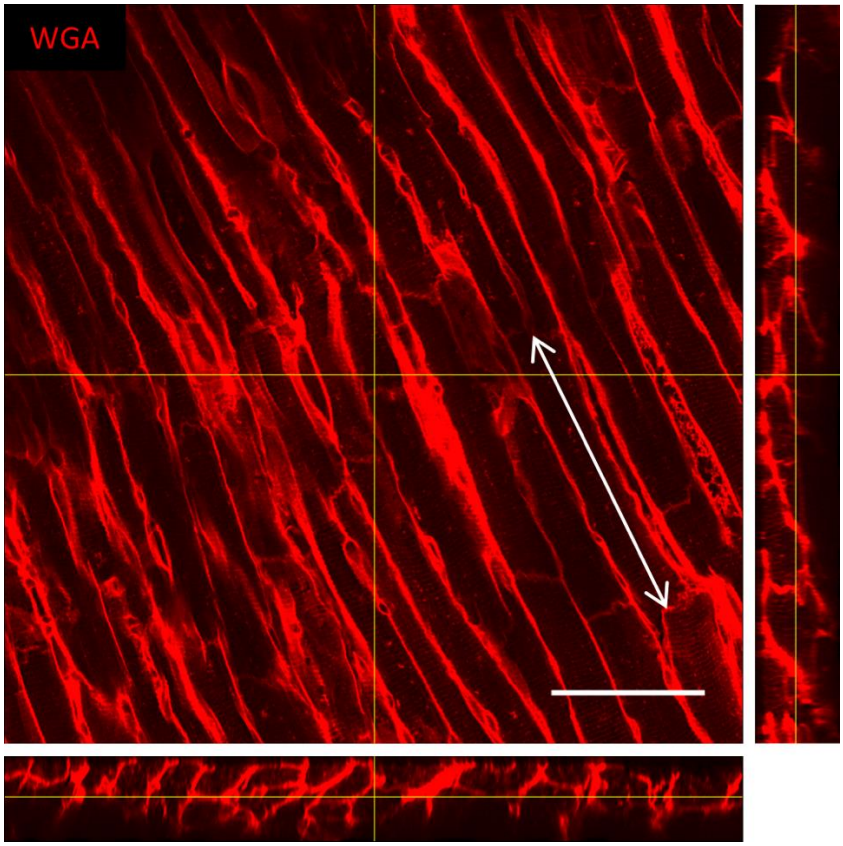

Figure 3.4. Orthogonal views of a representative confocal image volume. The extracellular space is clearly visible with the WGA stain (red), including t-tubule patterns. Cell ends are also visible, making measurement of myocyte length possible, as shown for example by the white arrow. Out-of-plane dimension can also easily be measured in orthogonal views. Scale bar: 50 micrometers.

3.3.3. Confocal Micrographs

A representative image volume is shown in three orthogonal views in **Figure 3.4**. The SNR in the central slice of these image volumes was approximately 50. Lateral and longitudinal cell borders are clearly distinguishable, and t-tubules are also visible. Transmural plots of myocyte length, width, and height, as well as CSA and MFA are shown in **Figure 3.5**. As expected, myocytes in TAC hearts exhibited a larger width and height compared to SHAM controls. SHAM hearts showed a transmural gradient in myocyte CSA, increasing from EPI to ENDO. The transmural gradient in CSA was diminished in TAC hearts, with increasing CSA across the wall, similar to previously measured data [18].

3.3.4. Correlations Between DT-MRI and Myocyte Geometry

Several correlations were found to be statistically significant between the DT-MRI data and measurements of myocyte geometry. As expected, fiber angles measured from bright field images and from DTI correlated significantly ($p<0.001$, $R^2=0.71$). Fiber angles from DTI also correlated with L:W ratio ($p<0.01$, $R^2=0.23$), indicating that MFA varies transmurally. Additional significant correlations between DTI-derived parameters and those measured from confocal images of tissue sections were as follows: Fiber diffusivity (λ_1) and all anisotropy metrics correlated significantly with fiber angle ($p<0.01$, $R^2=0.27$), again, indicating a transmural gradient. Planar anisotropy correlated significantly with fiber angle ($p<0.01$, $R^2=0.25$), myocyte width ($p=0.025$, $R^2=0.16$), MFA ($p<0.001$, $R^2=0.33$), and CSA ($p=0.019$, $R^2=0.17$). Sheet-normal diffusivity (λ_3) correlated significantly with MFA ($p=0.015$, $R^2=0.18$). The results of ANCOVA tests are presented in **Table 3.3**. Six of these correlations are also plotted in **Figure 3.6**.

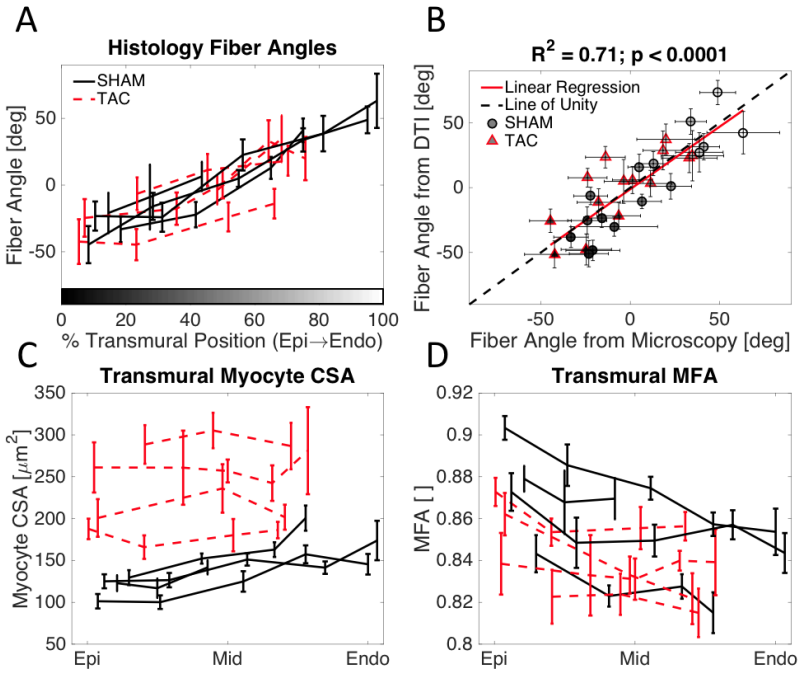

Figure 3.5. Summary of measurements from histological sections. (A) Transmural plots of fiber angle measurements from bright field images. (B) As expected, fiber angles correlated significantly ($p<0.0001$) with those from DTI. (C) Myocyte CSA exhibited a transmural gradient in SHAM hearts, with larger values in the ENDO. In TAC hearts, CSA was elevated, and the transmural gradient was diminished. (D) A Transmural gradient in myocyte fractional anisotropy (MFA) was observed, with lower values in the ENDO, especially in SHAM myocytes.

3.4. Discussion

In this work, we have shown that transmural gradients in myocyte geometry are present in the normal rat LV but are reduced in POH. This normal transmural gradient is characterized by larger myocyte CSA in ENDO than EPI. This is especially obvious in the transmural pattern of CSA and MFA **(Figure 3.5C-D)**. The observed reduction in this gradient in POH is similar to the results of Campbell, et al [18]. We also observed a difference in the transmural patterns of several other structural features, as measured from DT-MRI. One of importance is that of the orientation and dispersion of sheet structures. In agreement with our hypothesis, we observed that the transmural gradients in both the mean sheet angle and

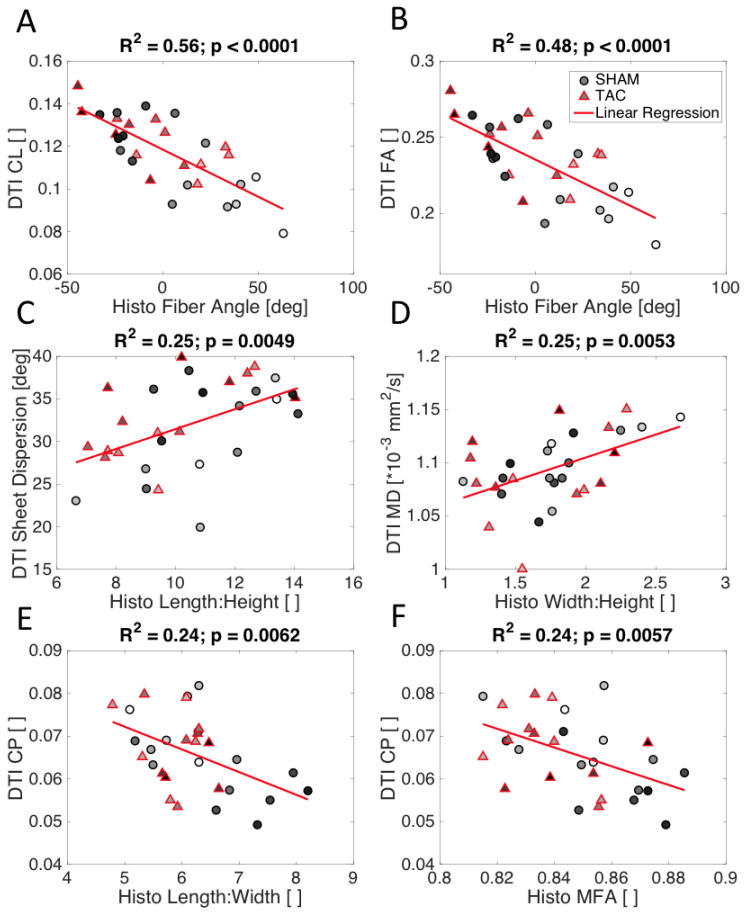

Figure 3.6. Correlations between DTI and histology. Grayscale color of markers indicates transmural location (black: ENDO, white: EPI). (A-B) Both linear and fractional anisotropy, respectively, exhibited a strong correlation with fiber angle, indicating that these parameters vary transmurally. (C) Sheet dispersion correlated with L:H ratio, (D) Mean diffusivity correlated with W:H ratio, and (E-F) Planar anisotropy correlated negatively with both L:W and MFA.

the dispersion of those angles about the mean, were more transmurally uniform in the LV of rats with POH. This does not indicate that sheet angles are globally reoriented to become, for example, more radially aligned as others have observed [35]. Rather, transmural variation is reduced so that across the wall, the orientation and dispersion of sheet structures were similar. Also of note, CP varied in the equatorial LV free wall, with a different pattern in SHAM than TAC hearts. In this region, CP decreased from EPI to ENDO in SHAM hearts, with a low

point in MID, whereas in TAC hearts, CP was lower in EPI and ENDO regions, with a high point in MID **(Figure 3.2)**.

Others have reported transmural gradients and responses to POH in the rat LV with different patterns than the present study [19], [20]. There are many factors that could contribute to these differences, including rat strain, the method of inducing pressure overload, and differences in measurement methods. However, our results do agree nicely with those of Campbell, et al, who showed a transmural gradient in myocyte CSA which is normalized in POH in the rat [17], [18]. Others have reported that transmural gradients in mitochondrial respiratory chain activity and oxidative stress are normalized in POH [46]. As sarcomeres are added and myocyte volume increases, the metabolic capacity must also increase to facilitate the energetic demands of those additional sarcomeres. It is clear that a remodeling balance must be achieved between the need to respond to the increase in downstream resistance to blood flow and the mechanical optimization of maintaining uniform fiber stress and strain under such conditions. Other structural features which exhibit a transmural gradient in normal tissue remodel during POH, such as titin isoform ratio, which modulates stiffness in pacing tachycardia, a model of heart failure [47], [48]. The remodeling of titin isoform leads to a relative increase in passive stiffness which, along with fibrosis and collagen remodeling, likely contribute to diastolic dysfunction.

Previous studies have shown transmural gradients in FA in normal hearts of sheep, human (in-vivo), and rat [31]–[33]. In sheep hearts, FA was lower in ENDO compared to MID or EPI regions [31]. In the human study, FA was higher in MID than ENDO or EPI [32]. Finally, in normal rat LV, a gradient of increasing FA from EPI to ENDO was observed [33]. In the current study, we observed an opposite trend to that of Giannakidis, et al, but similar to

that in sheep hearts, namely, with generally increasing values of FA from ENDO to EPI. Although Giannakidis, et al state that their result is consistent with measurements of myocyte CSA by McCrossan, et al [20], it is unclear how a decrease in L:W ratio would result in an increase in FA. Conversely, our results indicate a more logical correspondence between a decrease in FA when the L:W ratio decreases. In other words, the cell membranes of rounder myocytes with a lower aspect ratio would restrict diffusion in a more isotropic manner than longer, thinner (more anisotropic) myocytes. The same argument holds when comparing our results to those described by Campbell, et al, who showed that in normal Sprague-Dawley rats, myocytes in the ENDO had larger CSA than EPI [17]. However, we did not observe a significant reduction of the gradient of FA in TAC, as one might expect from the results of a follow-up study by Campbell, et al [18].

To our knowledge, this is the first study to show correlations between DTI-derived parameters and myocyte geometry measurements in the same hearts. Others have used a similar approach to validate that the eigenvectors correspond with local fiber and sheet orientations [28], [42], [49], and more recently, that the eigenvalues correlate with collagen content [34]. The correlations we observed between variables from DTI and measurements from histology were statistically significant, which may indicate that the DTI variables are influenced by myocyte geometry. Additionally, however, several of those same variables derived from DTI correlated significantly with the measured fiber angle, which features a roughly linear transmural gradient. This may indicate that both myocyte geometry and some other structural features which contribute to variation in DTI-derived parameters also vary transmurally, giving rise to the moderate correlations we observed. In reality, the restriction to self-diffusion of water at the 100-micrometer scale is highly complex [50] so it is likely that

structural features other than myocyte geometry (such as collagen content and composition) influence the diffusion weighted signal. However, we postulate that myocyte geometry plays an important role at the 100-micrometer resolution of our DTI scans. Potential methods to understand the contributions of different structural features to variation in DTI include simulation [51]–[53], and dPFG or mPFG pulse sequences or qMAS diffusion encoding [54].

Several limitations to this study are worth consideration. First, eight rats in each group is a relatively small number, and a better understanding of the differences between TAC and SHAM animals would require more. However, even with a relatively small N we were able to observe statistically significant, regionally varying differences in many DTI-derived parameters, as well as significant correlations with measurements from histological sections. Second, the region for correlating between DTI and histological measurement was limited to the LV free wall. This region was chosen because it is the most commonly studied. The nature of sectioning, staining, and imaging limits the expanse of regions that can be analyzed using this method. An interesting follow-up study would be to predict with a statistical degree of certainty myocyte geometry based on DTI in a different region, such as the septum. Third, due to the direction of sectioning for confocal imaging, we could not validate sheet angle measurements. However, this has previously been done and close agreement was found between DTI-derived sheet angles and those from histological measurement [30], [42]. Lastly, all image data acquisition was performed on fixed hearts. The process of fixation alters the microstructural environment by cross-linking proteins, and tissue shrinkage is a known side-effect. Thus, 3D diffusivity may not be completely representative of that in vivo. Additionally, further shrinkage is known to occur during processing of samples for histology. Despite these structural changes in tissue structure, we observed significant correlations in

multiple variables, indicating that the essence of tissue anisotropy and microstructure was preserved during fixation and histological processing.

We conclude that regional variations in tissue microstructural features are evident in normal hearts, and that remodeling during POH is spatially non-uniform, with apparently more myocyte remodeling in MID and ENDO regions than EPI. We have also shown that regional remodeling can readily be detected using cardiac DTI, with indications that parameters such as sheet dispersion and measures of anisotropy correlate significantly with variations in myocyte geometry, such as L:W ratio and MFA. As DTI is refined for in-vivo use in humans, this method appears to provide a non-invasive, comprehensive method to detect cardiac tissue microstructure and its remodeling during disease.

3.5. Acknowledgements

Chapter 3, in full, is a reformatted reprint of a paper in preparation to be submitted for publication. Carruth, E.D.; Teh, I.; Schneider, J.E.; McCulloch, A.D.; Omens, J.H.; Frank, L.R., “Regional Variations in Diffusion Tensor Anisotropy are Associated with Myocyte Remodeling in Left Ventricular Pressure Overload”. The dissertation author was the primary investigator and author of this paper.

The authors are grateful for the surgical and animal handling expertise of Diane Huang.

This project was supported by the National Institute of General Medical Sciences of the National Institutes of Health under grant number P41 GM103545-18.

3.6. Appendix: Additional Figures

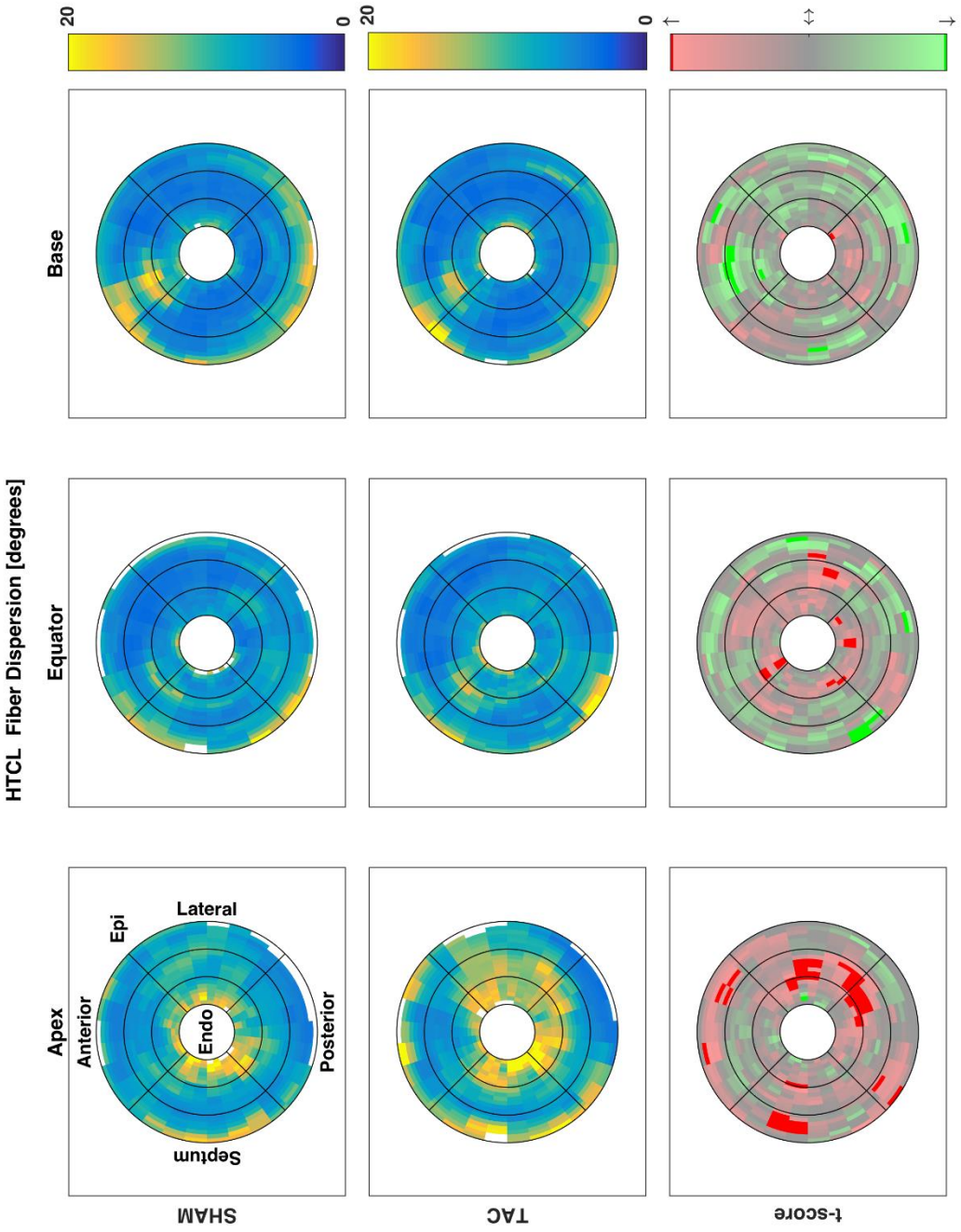

Figure 3.7. Regional distributions of additional DTI-derived parameters. Regional variations in fiber dispersion. **Figure 3.7** continues on the following page.

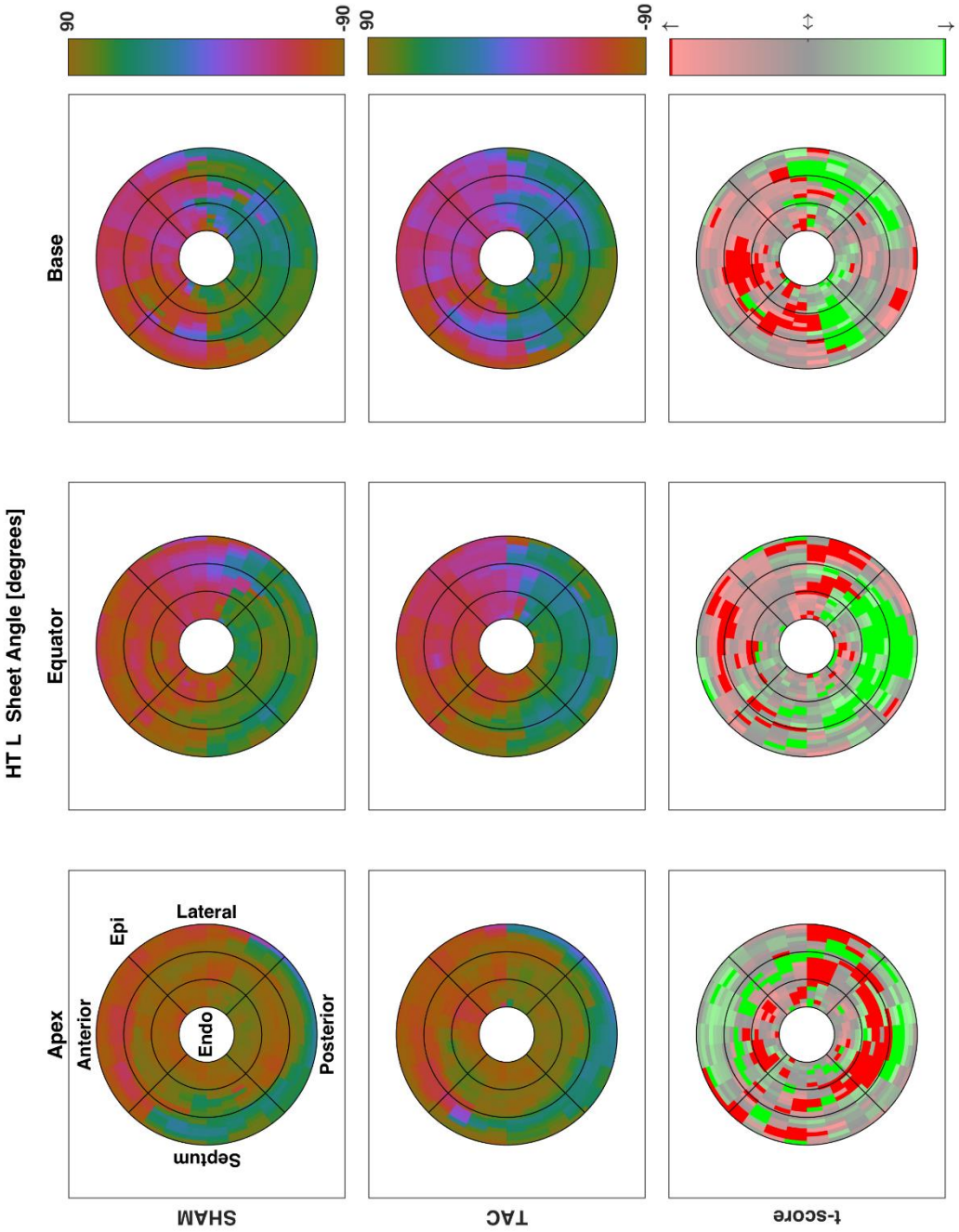

Figure 3.7. (Continued). Regional variations in sheet angle. **Figure 3.7** continues on the following page.

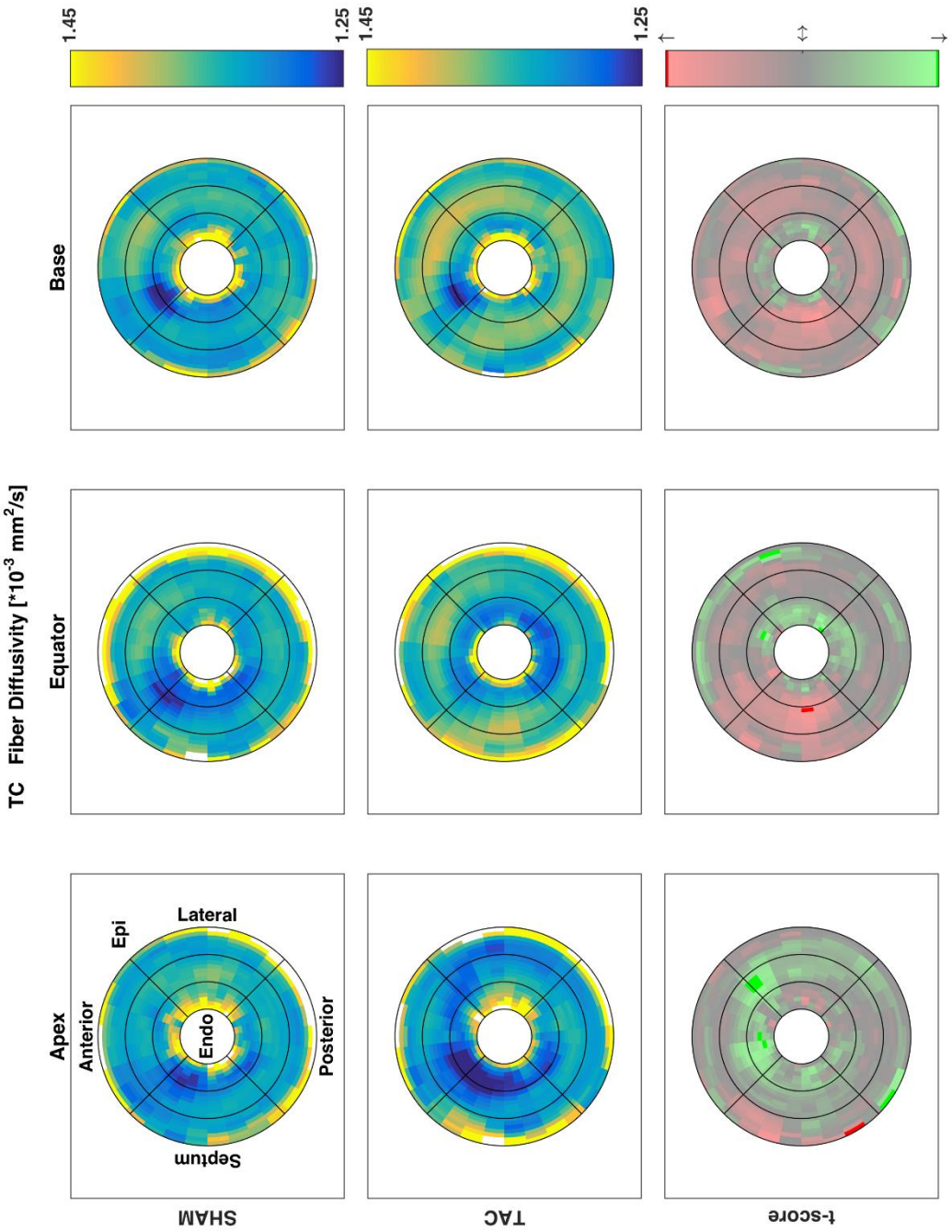

Figure 3.7. (Continued). Regional variations in fiber diffusivity (λ_1). **Figure 3.7** continues on the following page.

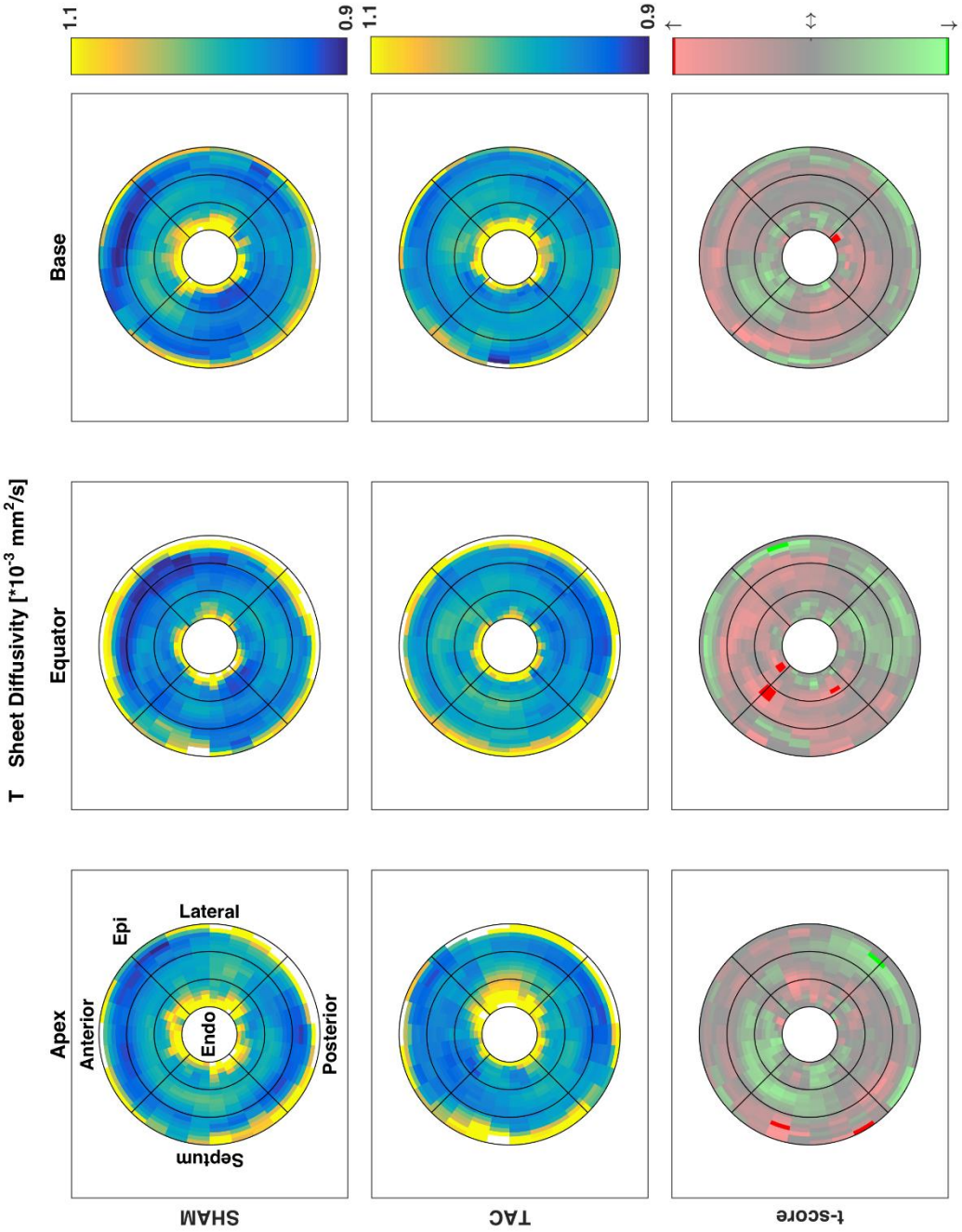

Figure 3.7. (Continued). Regional variations in sheet diffusivity (λ_2). **Figure 3.7** continues on the following page.

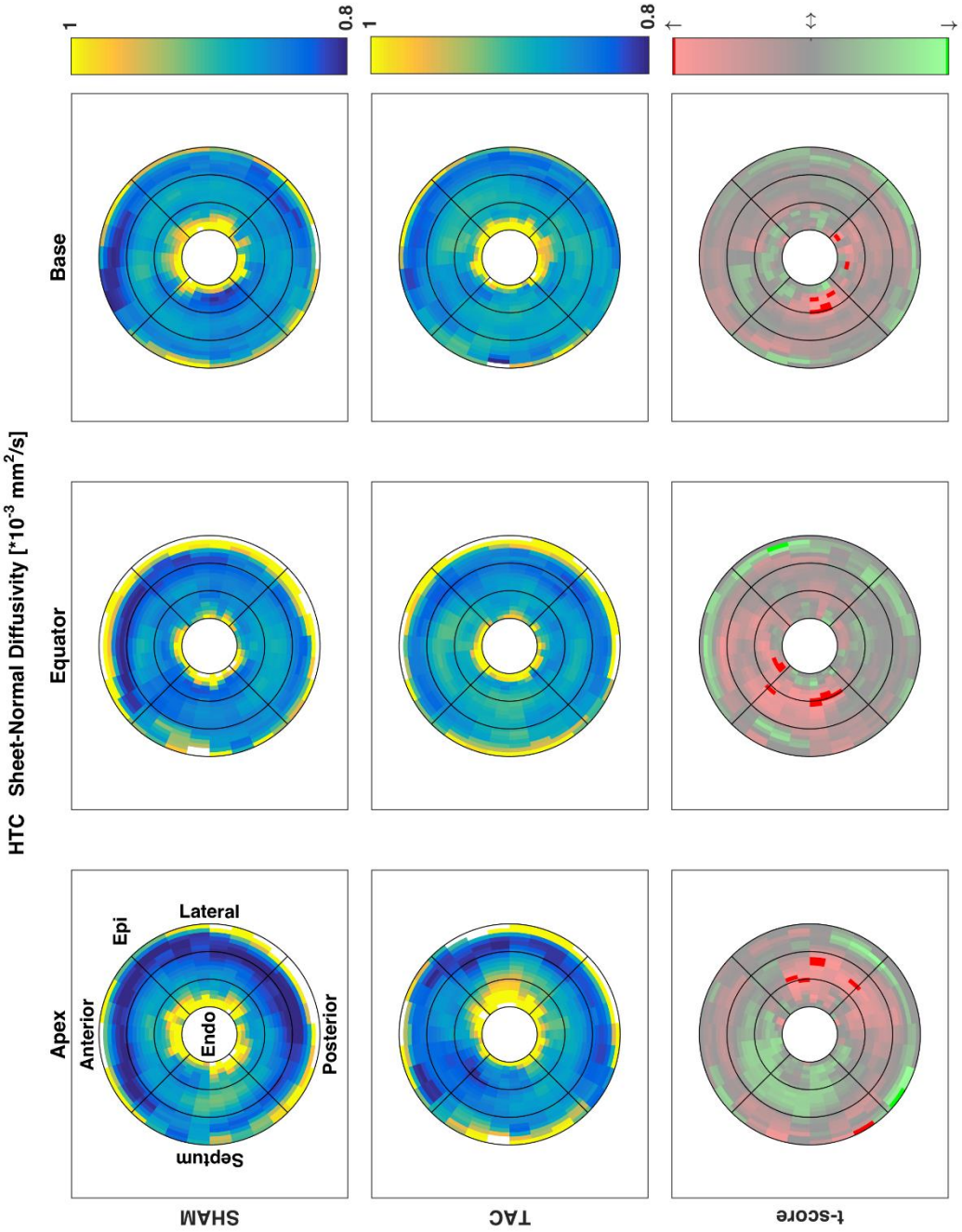

Figure 3.7. (Continued). Regional variations in sheet-normal diffusivity (λ_3). **Figure 3.7** continues on the following page.

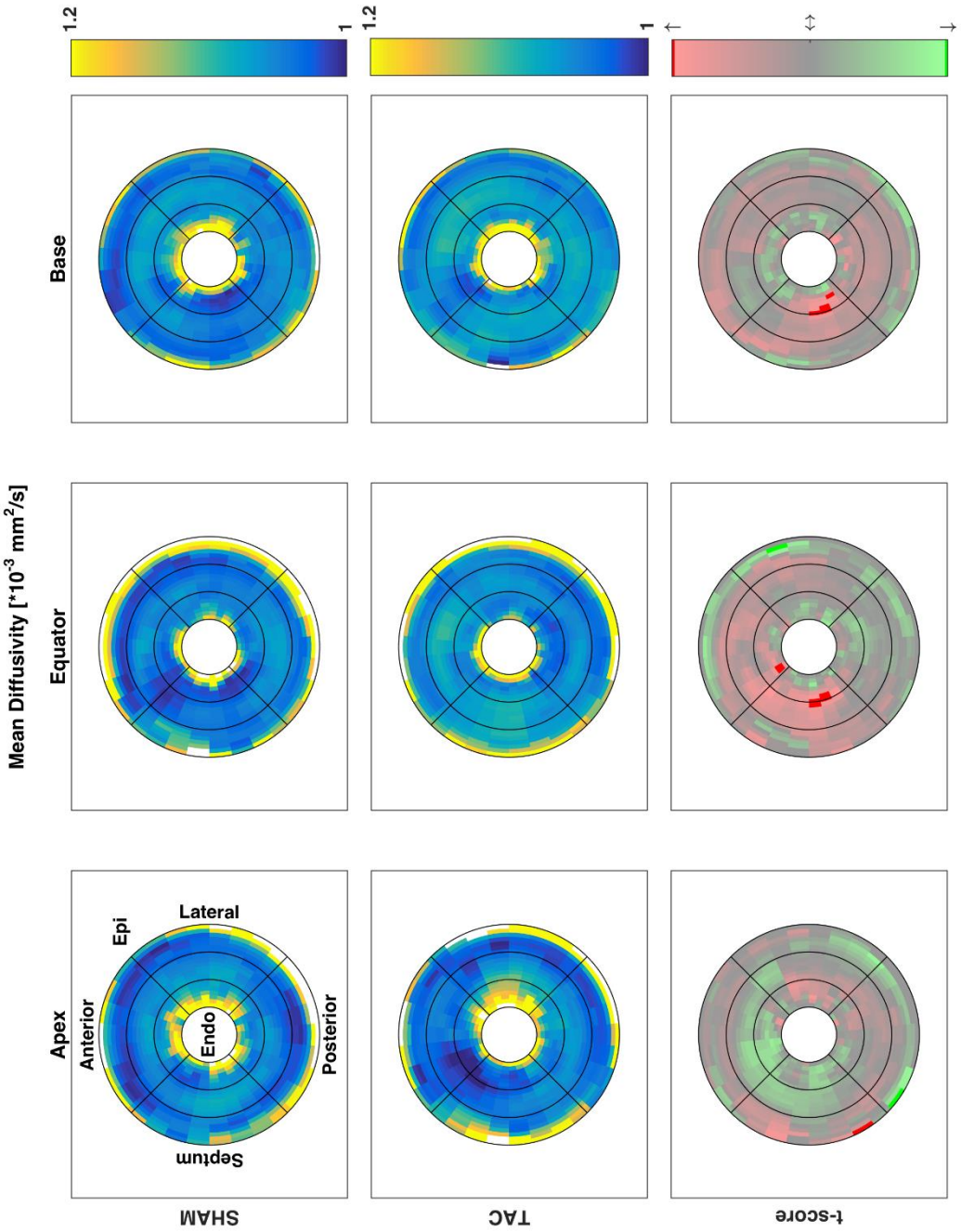

Figure 3.7. (Continued). Regional variations in mean diffusivity ($\hat{\lambda}$). **Figure 3.7** continues on the following page.

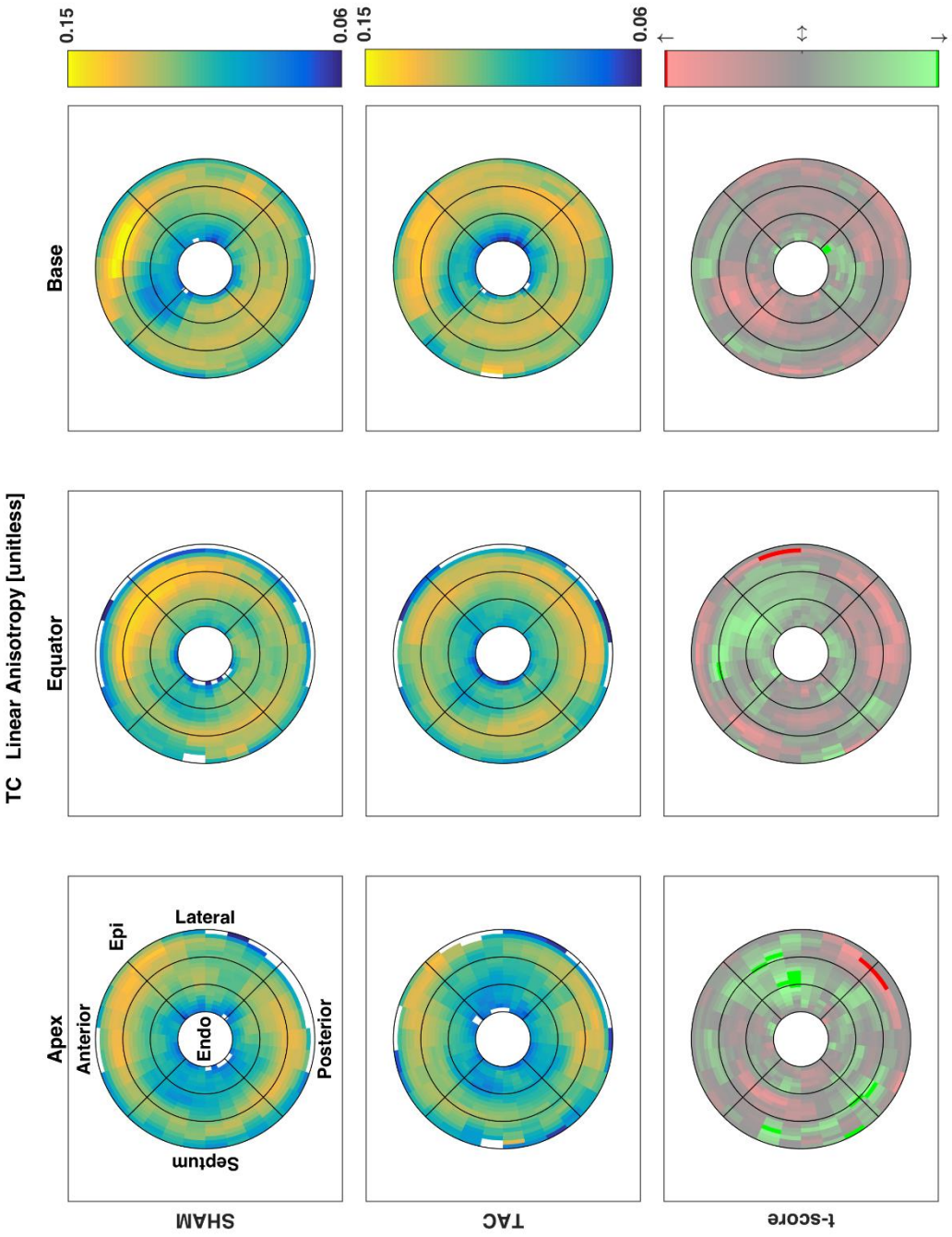

Figure 3.7. (Continued). Regional variations in linear anisotropy (CL). **Figure 3.7** continues on the following page.

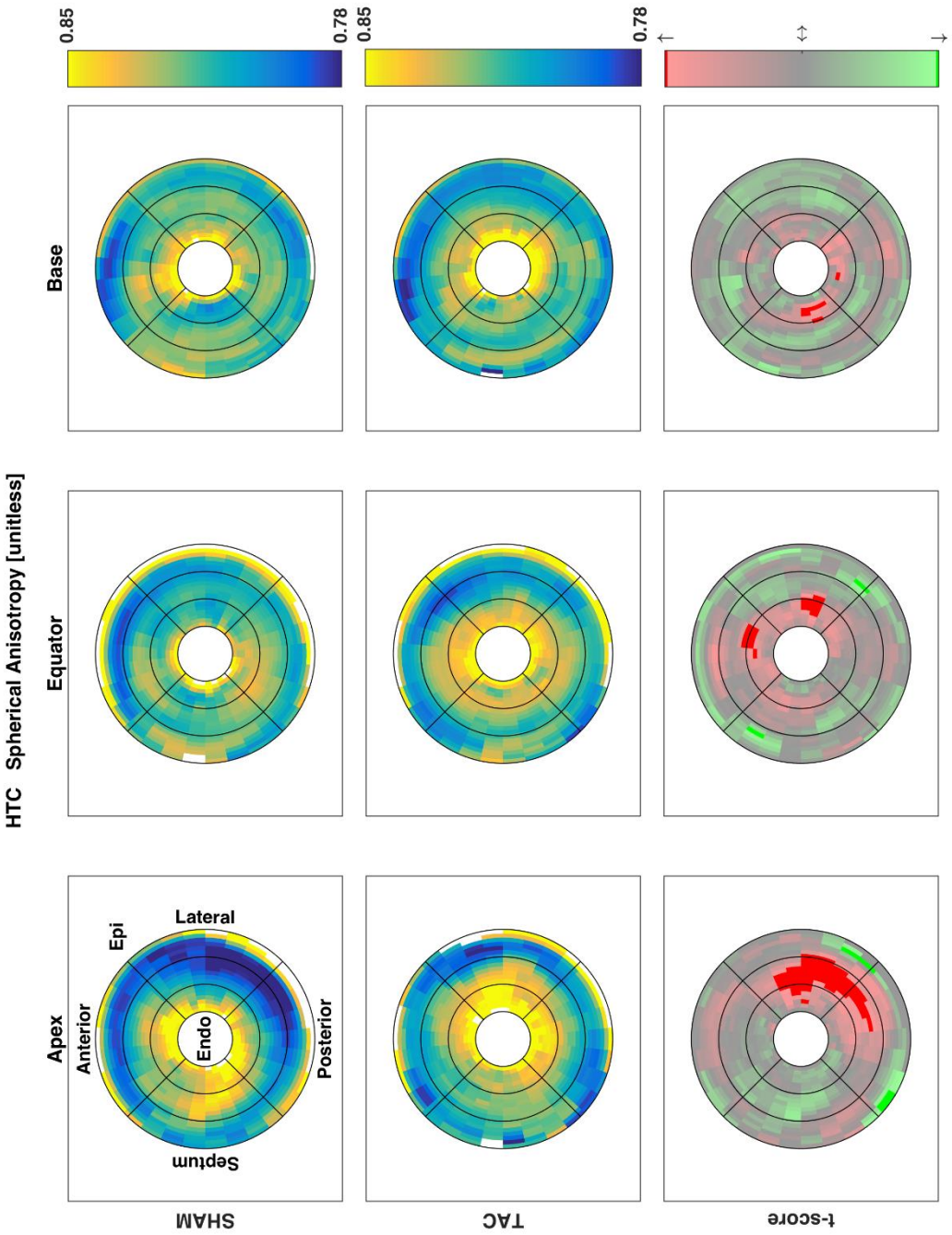

Figure 3.7. (Continued). Regional variations in spherical anisotropy (CS).

3.7. References

[1] E. J. Benjamin, S. S. Virani, C. W. Callaway, A. R. Chang, S. Cheng, S. E. Chiuve, M. Cushman, F. N. Delling, R. Deo, S. D. de Ferranti, J. F. Ferguson, M. Fornage, C. Gillespie, C. R. Isasi, M. C. Jiménez, L. C. Jordan, S. E. Judd, D. Lackland, J. H. Lichtman, L. Lisabeth, S. Liu, C. T. Longenecker, P. L. Lutsey, D. B. Matchar, K. Matsushita, M. E. Mussolino, K. Nasir, M. O'Flaherty, L. P. Palaniappan, D. K. Pandey, M. J. Reeves, M. D. Ritchey, C. J. Rodriguez, G. A. Roth, W. D. Rosamond, U. K. A. Sampson, G. M. Satou, S. H. Shah, N. L. Spartano, D. L. Tirschwell, C. W. Tsao, J. H. Voeks, J. Z. Willey, J. T. Wilkins, J. H. Wu, H. M. Alger, S. S. Wong, P. Muntner, M. J. Blaha, S. E. Chiuve, M. Cushman, S. R. Das, R. Deo, S. D. de Ferranti, J. Floyd, M. Fornage, C. Gillespie, C. R. Isasi, M. C. Jiménez, L. C. Jordan, S. E. Judd, D. Lackland, J. H. Lichtman, L. Lisabeth, S. Liu, C. T. Longenecker, R. H. Mackey, K. Matsushita, D. Mozaffarian, M. E. Mussolino, K. Nasir, R. W. Neumar, L. P. Palaniappan, D. K. Pandey, R. R. Thiagarajan, M. J. Reeves, M. D. Ritchey, C. J. Rodriguez, G. A. Roth, W. D. Rosamond, C. Sasson, A. Towfighi, C. W. Tsao, M. B. Turner, S. S. Virani, J. H. Voeks, J. Z. Willey, J. T. Wilkins, J. H. Wu, H. M. Alger, S. S. Wong, P. Muntner, C. W. Callaway, A. R. Chang, S. Cheng, S. E. Chiuve, M. Cushman, F. N. Delling, R. Deo, S. D. de Ferranti, J. F. Ferguson, M. Fornage, C. Gillespie, C. R. Isasi, M. C. Jiménez, L. C. Jordan, S. E. Judd, D. Lackland, J. H. Lichtman, L. Lisabeth, S. Liu, C. T. Longenecker, P. L. Lutsey, D. B. Matchar, K. Matsushita, M. E. Mussolino, K. Nasir, M. O'Flaherty, L. P. Palaniappan, D. K. Pandey, M. J. Reeves, M. D. Ritchey, C. J. Rodriguez, G. A. Roth, W. D. Rosamond, U. K. A. Sampson, G. M. Satou, S. H. Shah, N. L. Spartano, D. L. Tirschwell, C. W. Tsao, J. H. Voeks, J. Z. Willey, J. T. Wilkins, J. H. Wu, H. M. Alger, S. S. Wong, and P. Muntner, "Heart Disease and Stroke Statistics—2018 Update: A Report From the American Heart Association," *Circulation*, vol. 135, no. 10, p. CIR.0000000000000558, 2018.

[2] A. M. Gerdes, "The use of isolated myocytes to evaluate myocardial remodeling," *Trends Cardiovasc. Med.*, vol. 2, no. 4, pp. 152–155, 1992.

[3] O. Gjesdal, D. A. Bluemke, and J. A. Lima, "Cardiac remodeling at the population level--risk factors, screening, and outcomes.," *Nat. Rev. Cardiol.*, vol. 8, no. 12, pp. 673–85, 2011.

[4] K. I. and M. J, "Molecular pathways underlying cardiac remodeling during pathophysiologic stimulation," *Jorunal Amerian Hear. Assoc. Circ.*, vol. 122, no. 25, pp. 2727–2735, 2011.

[5] I. J. LeGrice, a. J. Pope, G. B. Sands, G. Whalley, R. N. Doughty, and B. H. Smaill, "Progression of myocardial remodeling and mechanical dysfunction in the spontaneously hypertensive rat," *AJP Hear. Circ. Physiol.*, pp. 1353–1365, 2012.

[6] J. E. Bishop and G. J. Laurent, "Collagen turnover and its regulation in the normal and

hypertrophying heart.," *Eur. Heart J.*, vol. 16 Suppl C, pp. 38–44, 1995.

[7] N. Bursac, "Cardiac fibroblasts in pressure overload hypertrophy: The enemy within?," *J. Clin. Invest.*, vol. 124, no. 7, pp. 2850–2853, 2014.

[8] T. Moore-morris, N. Guimarães-camboa, I. Banerjee, A. C. Zambon, T. Kisseleva, A. Velayoudon, W. B. Stallcup, Y. Gu, N. D. Dalton, M. Cedenilla, R. Gomez-amaro, B. Zhou, D. A. Brenner, K. L. Peterson, J. Chen, and S. M. Evans, "Resident fibroblast lineages mediate pressure overload – induced cardiac fi brosis," *J. Clin. Invest.*, vol. 124, no. 7, pp. 1–14, 2014.

[9] C. H. Conrad, W. W. Brooks, J. A. Hayes, S. Sen, K. G. Robinson, and O. H. L. Bing, "Myocardial Fibrosis and Stiffness With Hypertrophy and Heart Failure in the Spontaneously Hypertensive Rat," *Circ.* , vol. 91, no. 1, pp. 161–170, Jan. 1995.

[10] C. A. Souders, T. K. Borg, I. Banerjee, and T. A. Baudino, "Pressure overload induces early morphological changes in the heart," *Am. J. Pathol.*, vol. 181, no. 4, pp. 1226–1235, 2012.

[11] E. D. Carruth, A. D. Mcculloch, and J. H. Omens, "Transmural gradients of myocardial structure and mechanics : Implications for fiber stress and strain in pressure overload," *Prog. Biophys. Mol. Biol.*, vol. 122, no. 3, pp. 215–226, 2016.

[12] T. Arts, R. Reneman, and P. Veenstra, "A model of the mechanics of the left ventricle," *Ann. Biomed. Eng.*, vol. 7, no. 3–4, pp. 299–318, 1979.

[13] T. Arts, P. C. Veenstra, and R. S. Reneman, "Epicardial deformation and left ventricular wall mechanics during ejection in the dog.," *Am. J. Physiol.*, vol. 243, pp. H379–H390, 1982.

[14] P. H. M. Bovendeerd, T. Arts, J. M. Huyghe, D. H. van Campen, and R. S. Reneman, "Dependence of local left ventricular wall mechanics on myocardial fiber orientation: A model study," *J. Biomech.*, vol. 25, no. 10, pp. 1129–1140, 1992.

[15] J. M. Guccione, K. D. Costa, and A. D. McCulloch, "Finite element stress analysis of left ventricular mechanics in the beating dog heart," *J. Biomech.*, vol. 28, no. 10, pp. 1167–1177, 1995.

[16] B. L. Leonard, B. H. Smaill, and I. J. LeGrice, "Structural remodeling and mechanical function in heart failure.," *Microsc. Microanal.*, vol. 18, no. 1, pp. 50–67, 2012.

[17] S. E. Campbell, A. M. Gerdes, and T. D. Smith, "Comparison of regional differences in cardiac myocyte dimensions in rats, hamsters, and guinea pigs.," *Anat. Rec.*, vol. 219, no. 1, pp. 53–9, Sep. 1987.

[18] S. E. Campbell, B. Korecky, and K. Rakusan, “Remodeling of myocyte dimensions in hypertrophic and atrophic rat hearts.,” *Circ. Res.*, vol. 68, no. 4, pp. 984–996, 1991.

[19] J. H. Omens, E. K. Rodriguez, and A. D. McCulloch, “Transmural changes in stress-free myocyte morphology during pressure overload hypertrophy in the rat.,” *J. Mol. Cell. Cardiol.*, vol. 28, no. 9, pp. 1975–1983, 1996.

[20] Z. A. McCrossan, R. Billeter, and E. White, “Transmural changes in size, contractile and electrical properties of SHR left ventricular myocytes during compensated hypertrophy,” *Cardiovasc. Res.*, vol. 63, no. 2, pp. 283–292, 2004.

[21] S. M. Weis, J. L. Emery, K. D. Becker, D. J. McBride, J. H. Omens, and A. D. McCulloch, “Myocardial Mechanics and Collagen Structure in the Osteogenesis Imperfecta Murine (oim),” *Circ. Res.*, vol. 87, no. 8, pp. 663–669, 2000.

[22] I. K. Rüssel, M. J. W. Götte, J. G. Bronzwaer, P. Knaapen, W. J. Paulus, and A. C. van Rossum, “Left Ventricular Torsion. An Expanding Role in the Analysis of Myocardial Dysfunction,” *JACC Cardiovasc. Imaging*, vol. 2, no. 5, pp. 648–655, 2009.

[23] M. Stuber, M. B. Scheidegger, S. E. Fischer, E. Nagel, F. Steinemann, O. M. Hess, and P. Boesiger, “Patients Suffering From Pressure Overload,” *Methods*, 1999.

[24] E. Nagel, M. Stuber, B. Burkhard, S. E. Fischer, M. B. Scheidegger, P. Boesiger, and O. M. Hess, “Cardiac rotation and relaxation in patients with aortic valve stenosis,” *Eur. Heart J.*, vol. 21, no. 7, pp. 582–589, 2000.

[25] J. J. W. Sandstede, T. Johnson, K. Harre, M. Beer, S. Hofmann, T. Pabst, W. Kenn, W. Voelker, S. Neubauer, and D. Hahn, “Cardiac Systolic Rotation and Contraction Before and After Valve Replacement for Aortic Stenosis,” *Am. J. Roentgenol.*, vol. 178, no. 4, pp. 953–958, Apr. 2002.

[26] F. W. Aelen, T. Arts, D. G. Sanders, G. R. Thelissen, A. M. Muijtjens, F. W. Prinzen, and R. S. Reneman, “Relation between torsion and cross-sectional area change in the human left ventricle.,” *J. Biomech.*, vol. 30, no. 3, pp. 207–12, Mar. 1997.

[27] F. W. Prinzen, T. Arts, G. J. van der Vusse, and R. S. Reneman, “Fiber shortening in the inner layers of the left ventricular wall as assessed from epicardial deformation during normoxia and ischemia,” *J. Biomech.*, vol. 17, no. 10, pp. 801–811, 1984.

[28] E. W. Hsu, A. L. Muzikant, S. A. Matulevicius, R. C. Penland, and C. S. Henriquez, “Magnetic resonance myocardial fiber-orientation mapping with direct histological correlation.,” *Am. J. Physiol.*, vol. 274, pp. H1627–H1634, 1998.

[29] D. F. Scollan, A. Holmes, R. Winslow, and J. Forder, “Histological validation of myocardial microstructure obtained from diffusion tensor magnetic resonance

imaging.," *Am. J. Physiol.*, vol. 275, no. 6 Pt 2, pp. H2308-18, 1998.

[30] A. A. Holmes, D. F. Scollan, and R. L. Winslow, "Direct histological validation of diffusion tensor MRI in formaldehyde-fixed myocardium," *Magn Reson Med*, vol. 44, no. 1, pp. 157–161, 2000.

[31] Y. Jiang, J. M. Guccione, M. B. Ratcliffe, and E. W. Hsu, "Transmural heterogeneity of diffusion anisotropy in the sheep myocardium characterized by MR diffusion tensor imaging," *Am. J. Physiol. - Hear. Circ. Physiol.*, vol. 293, no. 4, pp. H2377–H2384, 2007.

[32] L. A. McGill, A. D. Scott, P. F. Ferreira, S. Nielles-Vallespin, T. Ismail, P. J. Kilner, P. D. Gatehouse, R. De Silva, S. K. Prasad, A. Giannakidis, D. N. Firmin, and D. J. Pennell, "Heterogeneity of fractional anisotropy and mean diffusivity measurements by in vivo diffusion tensor imaging in normal human hearts," *PLoS One*, vol. 10, no. 7, pp. 1–17, 2015.

[33] A. Giannakidis, P. Ferreira, G. T. Gullberg, D. Firmin, and D. J. Pennell, "Transmural gradients of preferential diffusion motility in the normal rat myocardium characterized by diffusion tensor imaging," *J. Cardiovasc. Magn. Reson.*, vol. 17, no. Suppl 1, p. Q117, 2015.

[34] O. M. Abdullah, S. G. Drakos, N. A. Diakos, O. Wever-Pinzon, A. G. Kfoury, J. Stehlik, C. H. Selzman, B. B. Reid, K. Brunisholz, D. R. Verma, C. Myrick, F. B. Sachse, D. Y. Li, and E. W. Hsu, "Characterization of diffuse fibrosis in the failing human heart via diffusion tensor imaging and quantitative histological validation," *NMR Biomed.*, vol. 27, no. 11, pp. 1378–1386, 2014.

[35] P. F. Ferreira, P. J. Kilner, L.-A. McGill, S. Nielles-Vallespin, A. D. Scott, S. Y. Ho, K. P. McCarthy, M. M. Haba, T. F. Ismail, P. D. Gatehouse, R. de Silva, A. R. Lyon, S. K. Prasad, D. N. Firmin, and D. J. Pennell, "In vivo cardiovascular magnetic resonance diffusion tensor imaging shows evidence of abnormal myocardial laminar orientations and mobility in hypertrophic cardiomyopathy," *J. Cardiovasc. Magn. Reson.*, vol. 16, no. 1, p. 87, Nov. 2014.

[36] D. McClymont, I. Teh, E. Carruth, J. Omens, A. McCulloch, H. J. Whittington, P. Kohl, V. Grau, and J. E. Schneider, "Evaluation of non-Gaussian diffusion in cardiac MRI," *Magn. Reson. Med.*, Sep. 2016.

[37] I. Teh, D. McClymont, R. A. B. Burton, M. L. Maguire, H. J. Whittington, C. A. Lygate, P. Kohl, and J. E. Schneider, "Resolving Fine Cardiac Structures in Rats with High-Resolution Diffusion Tensor Imaging," *Sci. Rep.*, vol. 6, p. 30573, Jul. 2016.

[38] J. G. Bensley, R. De Matteo, R. Harding, and M. J. Black, "Three-dimensional direct measurement of cardiomyocyte volume, nuclearity, and ploidy in thick histological

sections," *Sci. Rep.*, vol. 6, p. 23756, Apr. 2016.

[39] W. J. Karlon, P.-P. Hsu, S. Li, S. Chien, A. D. McCulloch, and J. H. Omens, "Measurement of Orientation and Distribution of Cellular Alignment and Cytoskeletal Organization," *Ann. Biomed. Eng.*, vol. 27, no. 6, pp. 712–720, Nov. 1999.

[40] R. W. Cox, "AFNI: Software for Analysis and Visualization of Functional Magnetic Resonance Neuroimages," *Comput. Biomed. Res.*, vol. 29, no. 3, pp. 162–173, Jun. 1996.

[41] V. Arsigny, P. Fillard, X. Pennec, and N. Ayache, "Log-Euclidean metrics for fast and simple calculus on diffusion tensors," *Magn. Reson. Med.*, vol. 56, no. 2, pp. 411–421, 2006.

[42] D. F. Scollan, A. Holmes, J. Zhang, and R. L. Winslow, "Reconstruction of cardiac ventricular geometry and fiber orientation using magnetic resonance imaging," *Ann. Biomed. Enigneering*, vol. 28, no. 8, pp. 934–944, 2000.

[43] P. W. Hales, J. E. Schneider, R. A. B. Burton, B. J. Wright, C. Bollensdorff, and P. Kohl, "Histo-anatomical structure of the living isolated rat heart in two contraction states assessed by diffusion tensor MRI," *Prog. Biophys. Mol. Biol.*, vol. 110, no. 2–3, pp. 319–330, 2012.

[44] P. J. Basser and C. Pierpaoli, "Microstructural and physiological features of tissues elucidated by quantitative-diffusion-tensor MRI," *J. Magn. Reson. - Ser. B*, vol. 111, no. 3, pp. 209–219, 1996.

[45] B. T. T. Yeo, T. Vercauteren, P. Fillard, J. M. Peyrat, X. Pennec, P. Golland, N. Ayache, and O. Clatz, "DT-REFinD: Diffusion tensor registration with exact finite-strain differential," *IEEE Trans. Med. Imaging*, vol. 28, no. 12, pp. 1914–1928, 2009.

[46] M. Kindo, S. Gerelli, J. Bouitbir, A. L. Charles, J. Zoll, T. H. Minh, L. Monassier, F. Favret, F. Piquard, and B. Geny, "Pressure overload-induced mild cardiac hypertrophy reduces left ventricular transmural differences in mitochondrial respiratory chain activity and increases oxidative stress," *Front. Physiol.*, vol. 3 AUG, no. August, pp. 1–14, 2012.

[47] S. P. Bell, L. Nyland, M. D. Tischler, M. McNabb, H. Granzier, and M. M. LeWinter, "Alterations in the determinants of diastolic suction during pacing tachycardia.," *Circ. Res.*, vol. 87, no. 3, pp. 235–240, 2000.

[48] G. W. Moe, "Pacing-induced heart failure: a model to study the mechanism of disease progression and novel therapy in heart failure," *Cardiovasc. Res.*, vol. 42, no. 3, pp. 591–599, 1999.

[49] I. J. LeGrice, B. H. Smaill, L. Z. Chai, S. G. Edgar, J. B. Gavin, and P. J. Hunter, "Laminar structure of the heart: ventricular myocyte arrangement and connective tissue architecture in the dog," *Am J Physiol*, vol. 269, no. 2 Pt 2, pp. H571-82, 1995.

[50] L. Wang, Y. M. Zhu, H. Li, W. Liu, and I. E. Magnin, "Simulation of diffusion anisotropy in DTI for virtual cardiac fiber structure," *Lect. Notes Comput. Sci. (including Subser. Lect. Notes Artif. Intell. Lect. Notes Bioinformatics)*, vol. 6666 LNCS, pp. 95–104, 2011.

[51] G. T. Balls and L. R. Frank, "A simulation environment for diffusion weighted MR experiments in complex media," *Magn. Reson. Med.*, vol. 62, no. 3, pp. 771–778, 2009.

[52] G. T. Baxter and L. R. Frank, "A computational model for diffusion weighted imaging of myelinated white matter," *Neuroimage*, vol. 75, pp. 212–220, 2013.

[53] D. B. Berry, B. Regner, V. Galinsky, S. R. Ward, and L. R. Frank, "Relationships between tissue microstructure and the diffusion tensor in simulated skeletal muscle," *Magn. Reson. Med.*, vol. 329, no. October 2017, pp. 317–329, 2017.

[54] F. Szczepankiewicz, S. Lasič, D. van Westen, P. C. Sundgren, E. Englund, C. F. Westin, F. Ståhlberg, J. Lätt, D. Topgaard, and M. Nilsson, "Quantification of microscopic diffusion anisotropy disentangles effects of orientation dispersion from microstructure: Applications in healthy volunteers and in brain tumors," *Neuroimage*, vol. 104, pp. 241–252, 2015.

4. Myocardial Infarction Sizing in the Mouse by 3D Multiplanar Reconstruction of Late Gadolinium Enhanced Magnetic Resonance Cardiac Imaging: Correlation with Regional Left Ventricular Dysfunction and Contractile Reserve

4.1. Introduction

Investigations of pharmacologic, cell-based, and gene treatments for the adverse effects of myocardial infarction (MI) are hampered by imprecise in vivo measurements of the extent of associated left ventricular (LV) regional dysfunction [1], [2]. Most contemporary small animal, cardiovascular experimental laboratories depend on two-dimensional (2D) echocardiography, with incorporated speckle tracking [3], for assessment of LV global and regional function. Despite its sophistication and easy implementation, 2D echocardiography remains limited perforce by planigraphic views that reflect incompletely the full, or three-dimensional (3D), extent of left ventricular myocardial shortening.

Some investigators have attempted to address shortcomings of 2D echocardiography by 3D reconstruction of 2D ultrasound images, acquired on a platform with micrometer precision rotation and translation and a holder device for probe stability [4], [5]. Relatively favorable intra-observer, inter-observer, and interstudy variability in calculations of LV volumes, mass, and ejection fraction (EF) were reported. We encountered technical difficulty in implementing such a protocol and have turned, along with others, to cardiac magnetic resonance imaging with late gadolinium enhancement (LGE) to evaluate myocardial infarct size and its associated pathophysiology and pathoanatomy [6]–[19].

When combined with cine-MR protocols, LGE MR images provide information on both cardiac structure and function, as well as an accurate non-invasive method to determine the MI size compared with histological standards. Gadolinium provides relatively selective

labeling of the area of injury in the near-term days following an infarct [13]. Membrane disruption of cardiomyocytes and increased capillary permeability within infarcted regions result in an expansion of extracellular volume, and this allows LGE to infiltrate, thus reflecting the area of myocardial damage after infarction. LGE MR-determined MI size has been widely used in human and mouse models with relatively good accuracy in predicting long-term mortality [19], as well as cardiac function and remodeling [8], [9], [11]. Nevertheless, in most of these studies, the degree of associated regional myocardial dysfunction has been quantified using a 2D analysis, with minimal use of parametric 3D display and without normalization of regional wall motion to overall ventricular size.

We aimed in this murine experiment, using 3D constructs, to compare in vivo LGE-MI and post-mortem histologic infarct size with both regional dysfunction and left ventricular contractile reserve, assessed early (2 days) and late (4 weeks) following the onset of injury. Endocardial segmentation of multiplanar (base to apex) slices, with subsequent 3D reconstruction, was utilized to define both global and regional LV function. The ultimate goal was to provide tissue and functional standards for measuring infarct size against which therapeutic interventions could be more accurately compared.

4.2. Methods

4.2.1. Animal Model and Experimental Protocol

All procedures were conducted according to established guidelines, and with the approval of the UC San Diego Institutional Animal Care and Use Committee (IACUC). A total of 22 male, C57BL/6J mice were purchased from a licensed vendor (Jackson Laboratory, Bar Harbor, ME) and used in this study. Of these 22 mice, 3 died before the MRI scan on day 2 post-MI, 5 died before the MRI scan on week 4, and 3 died before finishing the

hemodynamic study on week 4. For the remaining 11 mice, the baseline body weight was 24.6 ± 1.5 g, mean age was 12.4 ± 0.3 weeks.

4.2.2. MI Surgery

The mouse model of chronic myocardial infarction was produced by ligation of the anterior descending branch of the left coronary artery (LAD) as previously described [Kumara 2005]. Briefly, mice were anesthetized with 1-1.5% isoflurane, intubated via the trachea, and mechanically ventilated with room air (respiratory rate 55–65 breaths per minute, tidal volume 2.5 ml). Under sterile conditions, a left anterior thoracotomy was performed to expose the heart. The left anterior descending coronary artery was ligated between the right ventricular outflow tract and the left atrium with a 6-0 silk suture that was passed through the superficial layers of myocardium [20]. The lungs were then reinflated and the chest incision closed.

4.2.3. MRI Protocol

All mice were scanned on a horizontal Bruker Biospec 7T/20 MRI system (Bruker, Germany). MRI scans were performed 1-2 days before surgery as a baseline, then follow-up scans were done 2 days and 4 weeks after surgery. Animals were anesthetized with 2% isoflurane in oxygen [11]. Heart rate ranged from 350 to 450 bpm, and respiratory rate was 30 to 40 breaths per minute. Two metallic needles were placed subcutaneously over the axillary area to monitor the ECG signal, and a pressure transducer was placed under the animal's back to monitor respiration. The body temperature was monitored and maintained at 37°C by a feedback controlled forced air heating system (SA Instruments, Stony Brook, NY). The ECG and respiratory signals were sent to a gating system (SA Instruments) for simultaneous ECG triggering and respiration gating.

MR images were acquired with a quadrature birdcage transceiver coil. All imaging protocols were performed with the animal lying on its back, with no rotation of the spine. For LGE imaging, a 30μL bolus of 0.5 mmol/kg Gd-DTPA (Magnevist®, Schering Healthcare, UK) was given by intraperitoneal injection 20-50 minutes prior to the MR scan [21], **Figure 4.1B**. A coronal view was used as a long axis reference. Short axis planes were manually set perpendicular to both the coronal plane and the long axis. In mice, 6-7 (depending on heart size) contiguous short axis slices were required to cover the entire left ventricle. FLASH-CINE images were acquired with the following image acquisition parameters: FOV: 1.5 × 2.0 cm, matrix size: 128 × 128, slice thickness: 1 mm, inter-slice distance: 1 mm, echo time: 2.1 msec, repetition time: 6 msec, 6 averages, flip angle: 40°, and 20 frames per cardiac cycle. For a single slice, the total acquisition time was approximately 100 to 110 seconds. Acquisitions were synchronized with the peak of the QRS complex. On average, MRI sessions were 35 ± 5 minutes per mouse.

4.2.4. Hemodynamic Measurements

Hemodynamic measurements were acquired within 1-2 days after the 4 week MR scan. Before cardiac catheterization, the mice were anesthetized with an intraperitoneal injection of ketamine (100 mg/kg) and xylazine (10 mg/kg). The animals were then intubated, placed on a ventilator (100-110 stroke/min, 0.4-0.5 mL stroke volume), and the right carotid artery exposed. The femoral vein was cannulated with stretched PE50 tubing for drug administration. A 1.4 French high fidelity catheter-tip micromanometer (Millar Instruments, Houston, TX) was inserted retrograde into the aorta via the left carotid artery and advanced into the left ventricle.

After bilateral vagotomy, baseline pressures were recorded when pressure returned to a stable state. Dobutamine was given through the femoral vein at successively higher dosages of 0.75, 2, 4, 6 and 8 μg/kg/min. Pressure data was analyzed three minutes after the administration of each dose. Pressure was recorded through the LabChart acquisition system (AD Instruments), and analyzed by a custom-made program (HeartBeat) as described previously [20].

4.2.5. Post-Mortem Histology

Immediately following the hemodynamic study, the mouse was treated with 200 μL heparin (1000 units/mL) and 0.3M PBS KCl solution was injected through the inferior vena cava for induction of diastolic cardiac arrest. After surgical isolation from the right ventricle and atria, the LV was weighed, frozen on dry ice, and kept at -20°C for 40 minutes. A tissue matrix and stainless steel blades (Electron Microscopy Sciences, Hatfield, PA) were then used to cut the LV into 6-8 transverse slices, the thickness of which was approximately 1 mm. These slices were transferred into a 1.5% 2,3,5-triphenyltetrazolium chloride (TTC) solution and incubated at 37°C for 15 minutes. The slices were then immersed in 10% neutral formalin for 1 hour to enhance the contrast between the viable myocardium and scar tissue. The TTC-stained slices were finally scanned (4800 dpi) for the measurement of infarction size [22]. The MI size was calculated by an area-based algorithm **(Figure 4.1C)**, and expressed as a percentage of LV mass, inasmuch as this algorithm had been reported to give the same relative relationship of MI size measured as that by a length-based algorithm [23].

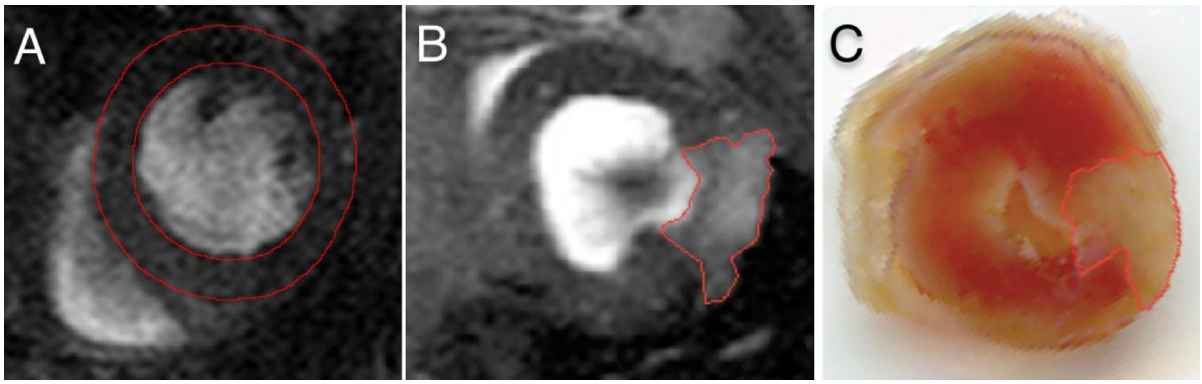

Figure 4.1. Segmentation of MRI and TTC images. (A) The segmentation of endocardial (interior) and epicardial (exterior) borders in Seg3D (segmented in red). **(B)** Myocardial infarction tissue on an LGE MR image (segmented in red). **(C)** Corresponding post-mortem slice of left ventricle with TTC staining of area of infarction (segmented in red).

4.2.6. Image Analysis

End-diastolic (ED) and end-systolic (ES) frames were chosen as those with the largest and smallest chamber area, respectively, and slices were stacked into a 3D image volume. Each slice was zero-filled to improve the smoothness of resulting endocardial and epicardial borders. Seg3D (Scientific Computing Institute, University of Utah, Salt Lake City, Utah) was used to manually create a mask of the myocardium, excluding papillary muscles and trabeculae when defining the endocardial surface **(Figure 4.1A)**. An in-house developed script was written in MATLAB® (MathWorks, Natick, MA), to read in the myocardial masks, detect the endocardial and epicardial borders, and register those data into scanner space. Data were interpolated along the long axis using cubic interpolation to improve mesh fitting in Continuity 6 (National Biomedical Computation Resource), as described below.

4.2.7. 3D Reconstruction in Continuity – 3D Kinesis Analysis

The borders derived from MR images were imported into Continuity (6.4b revision 8234, National Biomedical Computation Resource) for 3D reconstruction and regional

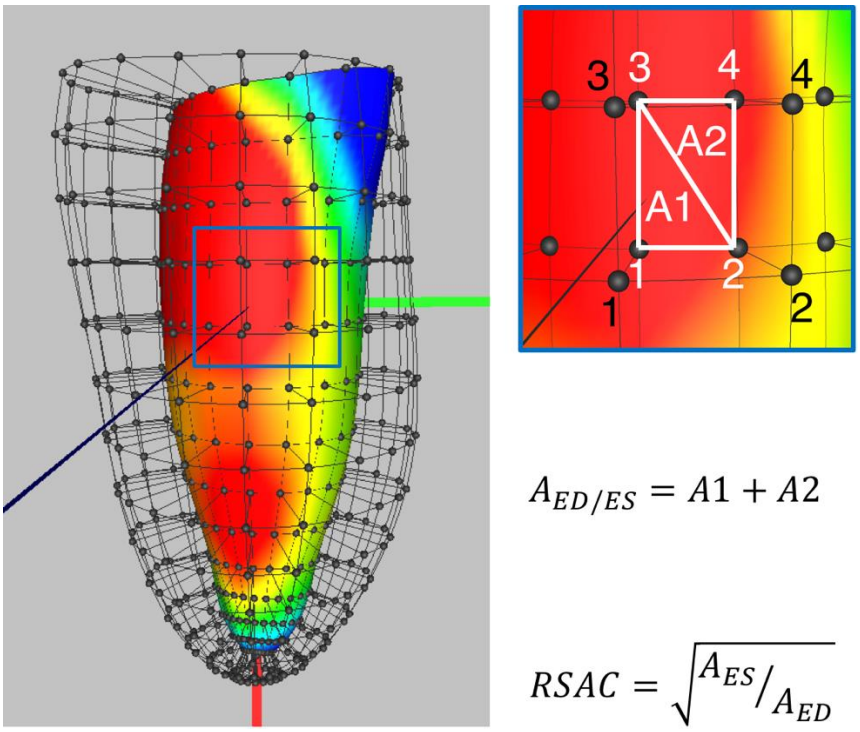

Figure 4.2. RSAC Algorithm. Illustration of the algorithm used to calculate the RSAC of each surface area element. Triangulation was used to calculate the two areas comprising each of the rectangular-like elements created by the fitted mesh for both end-systolic (ES, white numbering) and end-diastolic (ED, black numbering) surfaces.

displacement analysis. In Continuity, a prolate spheroidal finite element mesh was fitted using least squares to the data points of ED borders to form the ED mesh. The ES border underwent the same fitting process to create the ES mesh. Initially, 50 nodes were arranged on each fitted mesh, and after the refining process, a total of 300 nodes were rendered according to the curvature of the mesh surface [12].

Displacement between ED and ES was determined as the Euclidian distance (calculated based upon Cartesian coordinates x, y, and z in 3D space) between corresponding nodes on the ED and ES endocardial mesh surfaces. For rendering purposes in order to better understand endocardial 3D deformation, a composite mesh was created with outer and inner

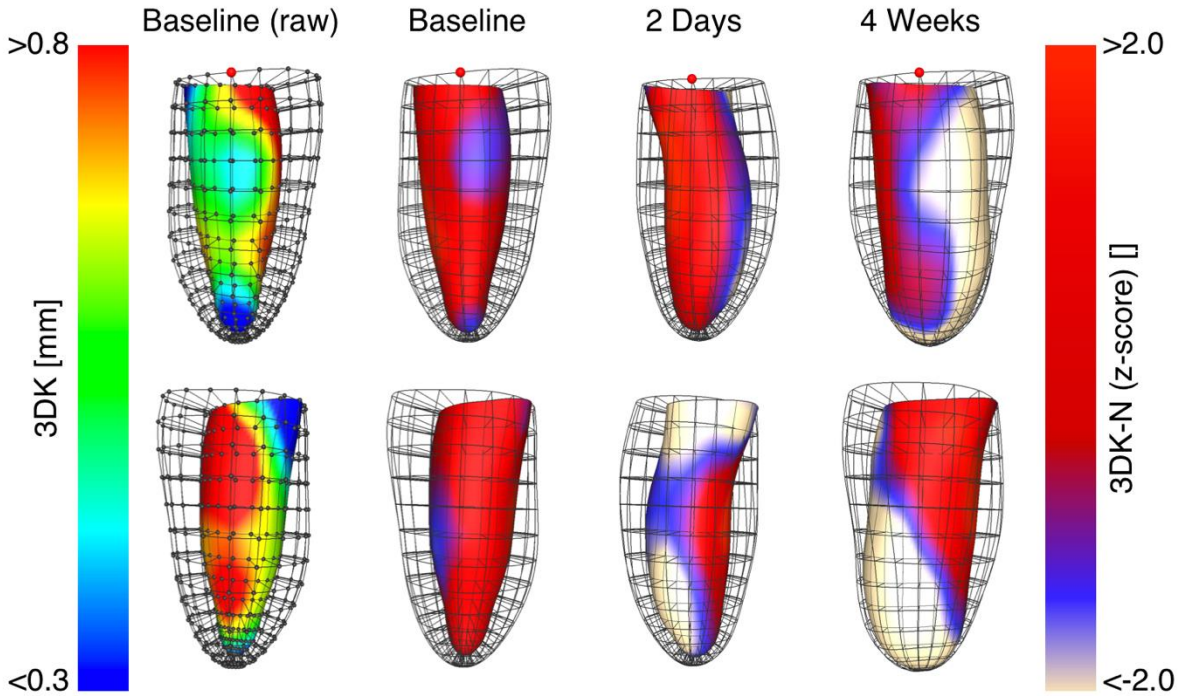

Figure 4.3. Representative serial parametric images of infarcted mouse heart. Note the change in relative wall motion and cardiac remodeling post-myocardial infarction. Top row is an anterior view, bottom row is a posterior view. Color-coded parametric images, left to right, show raw (baseline) and calculated Z scores for 3D-kinesis (3DK) at baseline, 2 days post-MI, and 4 weeks post-MI. The % of abnormal 3DK values (-2.0 SD's) were 14.6% and 31.4%, respectively, at 2 days and 4 weeks.

surfaces representing the endocardial surface at ED and ES, respectively **(Figure 4.3)**. For all other analyses, the 80 most apical nodes were excluded to avoid error since no reliable image data were available in these regions. The 3D Kinesis (3DK) was defined as the Euclidian distance a between a node's position at ED and ES.

4.2.8. MRI Determination of LV Mass and LV Ejection Fraction

Both ED and ES chamber volumes (EDV and ESV, respectively), and ED myocardial volume (EDMV) were calculated from the fitted meshes in Continuity. LV EF was then derived. LV mass was calculated by ED myocardial volume multiplied by myocardial specific gravity, γ_{myo} (1.055 g/cm3):

$$Mass_{LV} = \gamma_{myo} \times EDMV$$

These MRI-derived estimates of LV mass were compared with the LV wet weight of all surviving mice (n=11).

4.2.9. 3D Reconstruction in Continuity – Regional Surface Area Change Analysis

In order to evaluate the effects of the infarction on regional circumferential and longitudinal myocardial shortening, excluding radial movement, the SQUEEZ algorithm developed by Pourmorteza et al. in 2012 [24] was modified for the generated LV model to calculate 3D regional surface area change (RSAC). The 3D RSAC values were calculated on each surface element according to the following formula:

$$RSAC = \sqrt{Area_{ES}/Area_{ED}}$$

In order to fit a node-based data structure on the mesh, a RSAC value was assigned to each node by averaging the RSAC values of its surrounding elements, **(Figure 4.2)**.

4.2.10. Regional Variability of Contraction

Since myocardial kinetic movement varies from region to region of the heart, applying a single threshold for abnormality to an absolute displacement parameter may reveal false, sub-threshold values in some regions of a normal heart. Therefore, a comparison based upon the geometric variability of normal left ventricular motion is necessary. Similar to the work of Sheehan *et al* in the so-called "centerline method" for 2D wall motion analysis [25], [26], we used control (pre-infarction) measurements to calculate the baseline mean and standard deviation for each individual node (1-220) for each wall motion parameter (3DK and RSAC).

The statistical distribution of each control node was then applied to the linear transformation of every corresponding node post-MI to calculate a so-called Z score,

according to the formula below (Xi indicates the parameter on node i, where i = 1 to 220) [25], [26]:

$$X_{i,Z} = \frac{X_{i,ischemic} - X_{i,mean\ (control)}}{SD_{i,control}}$$

For 3DK, a node that moved less than 2.0 standard deviations from the mean of the control group was classified as akinetic/dyskinetic (abnormal). For RSAC, a node with its normalized value larger than 2.0 standard deviations was similarly classified as abnormal. For analysis of the post-MI evolution of individual nodes, those values beyond -2.0 (3DK) or +2.0 (RSAC) standard deviations were classified as clearly "abnormal" and within the MI zone, and those with values between -1.5 to - 2.0 (3DK) or +1.5 to +2.0(RSAC) were classified as within the peri-MI zone.

A pseudo-color spectrum, calibrated to the magnitude of a given shortening parameter, was used to create a 3D parametric display of endocardial movement in relation to topographic location, **Figure 4.3**. As expected, the baseline parametric image displayed relatively uniform color (homogeneous regional contraction) and the post-infarct color display reflected the heterogeneity of abnormal regional wall motion, **Figure 4.3**. The 3D reconstruction can be shown in any given projection. In **Figure 4.3**, the top row represents an anterior-posterior projection, whereas the bottom row is posterior-anterior. Dynamic display of the transition between ED and ES showed clearly an area of abnormal kinesis in relation to its topographic location. The mesh composite provides a reference frame to see the change in endocardial surface shape from ED (outer wireframe surface) to ES (parametric image). For both normalized parameters (3DK, RSAC) the amount of abnormal myocardium (hence the

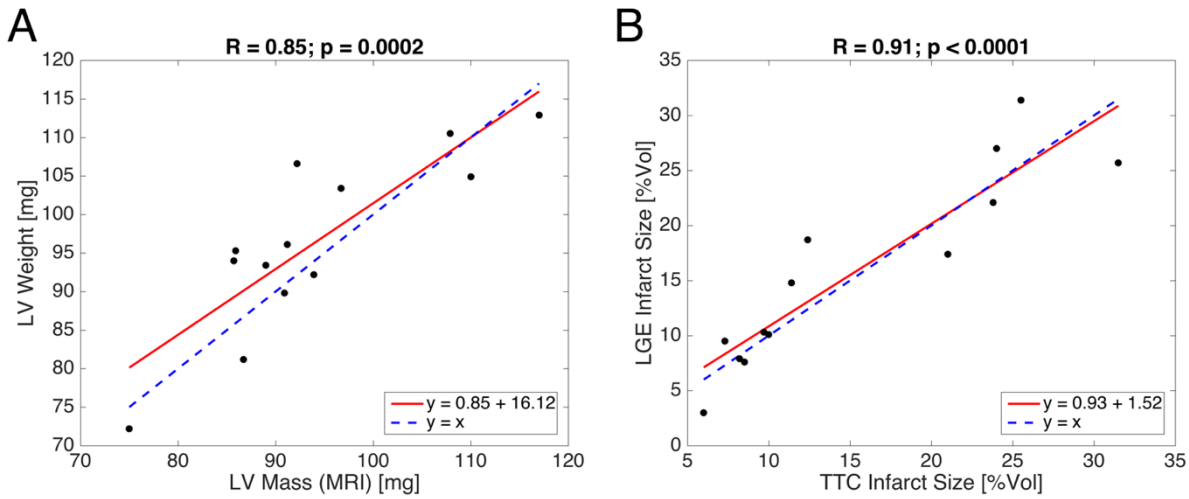

Figure 4.4. Verification of MRI segmentation. (A) Correlation of LV mass derived from cardiac MRI (abscissa) versus post-mortem LV wet weight (ordinate). **(B)** Correlation of MI size, determined by TTC staining (abscissa) and LGE (ordinate).

"functional infarct size") was calculated by summing the number of all abnormal nodes, and was expressed as a percentage of the total of 220 nodes.

4.2.11. MRI Determination of Myocardial Infarction Size

ED LGE images of each slice were selected for infarction scar delineation. The infarction scar borders were traced by an observer in ImageJ (NIH, using a semi-automatic segmentation plugin (JFilament) to minimize observer influence on the ROI [27]. In order to exclude artifacts, adjacent frames at the same slice location and adjacent slices were also used as references. The observer was blinded from hemodynamic information during image segmentation. The sizes of the contrast-enhanced areas in the MR images were plotted against the corresponding areas obtained from TTC staining, as shown in **Figure 4.4B**. Infarction size was expressed as a percentage of LV mass:

$$LGE\ MI\ size = 100\% \times \left[\gamma_{myo} \sum_{Base}^{Apex} (ED\ area_{scar}) \times slice\ thickness\right] / LV\ mass$$

Table 4.1. Summary of functional parameters from MRI

	LV EDV [μL]	LV ESV [μL]	LV EF [%]
Baseline	50.6 ± 6.6	15.6 ± 3.7	69.7 ± 4.1
2 Days	58.4 ± 13.9	29.6 ± 13.8	51.5 ± 14.1
4 Weeks	98.3 ± 43.0	62.6 ± 41.7	41.9 ± 14.9

4.2.12. Statistical Data Analysis

Prism 5.0 (GraphPad Software, Inc., San Diego, CA) was used for most standard statistical analyses. All values are reported herein as mean ± standard deviation. Linear regression, and a correlation coefficient (R) value, was used to assess the agreement between two correlated parameters. The paired, two-tailed Student's t-test was used for comparison between baseline and 2-day or 4-week MI groups. We also used the Bland-Altman analysis to assess the relative agreement of (1) MRI-derived LV mass and LV wet weight, and (2) LGE MR image and TTC staining measured infarction size. A p-value less than 0.05 was considered statistically significant for all comparison tests.

4.3. Results

4.3.1. Validation of MRI-Derived LV Mass and Infarct Size

The measurements of LV wet weight were plotted against the corresponding calculated, MRI-derived LV mass data. A strong linear correlation was demonstrated ($r=0.85$, $n=13$, $P<0.001$); the slope was close to unity (0.85) with an intercept of 16.12, **Figure 4.4A**. A Bland-Altman analysis showed a mean difference of 0.03 mg between the two methods, with upper 95% limits of agreement at 14.29 mg, and lower 95% limits at -14.23 mg. MRI-derived LV mass was 85.7 ± 8.7 mg at baseline, 93.9 ± 10.8 mg at 2 days and 97.6 ± 10.0 mg at 4 weeks post-MI. By comparison, the LV wet weight was 95.6 ± 10.4 mg at 4 weeks post-MI, P =NS. Functional parameters measured from CINE MRI data are summarized in **Table**

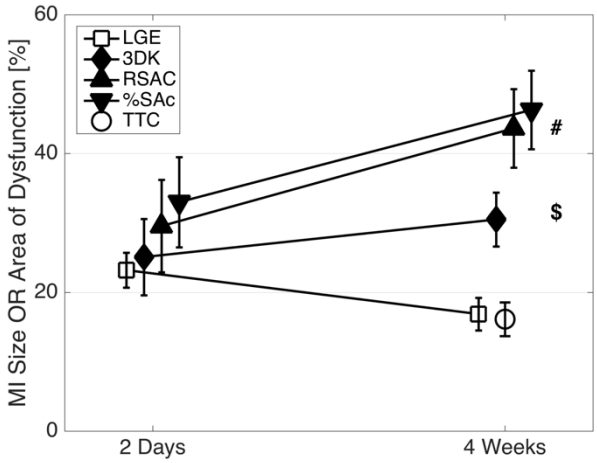

Figure 4.5. Time course of MI size. Comparison is between infarct size by histology (TTC, white circle) and MRI (LGE, white square) with percentage of abnormal functional indices (black markers). The differences in the measurement of MI size by LGE was not statistically different than any abnormal dysfunction indices at 2 days. However, at 4 weeks, the % abnormal 3DK, RSAC, and %SA change were all significantly different from MI size measured by both LGE and TTC ($p<0.001$ for all 6 comparisons).

4.1, below**.** The mean of LGE MI size was 22.1 ± 9.1% (ranging from 7.5% to 35.4%) at 2 days post-MI, and 15.8 ± 8.7% at 4 weeks post-MI. Post-mortem TTC measurements at 4 weeks gave a mean of 15.3 ± 8.6%, **Figure 4.5**.

4.3.2. Quantification of Regional Myocardial Dysfunction

The percentage (%) of abnormal 3DK nodes (Z score ≤ -2.0) and RSAC nodes (Z score ≥ +2.0) observed in the chronic MI group at 4 weeks post-MI, averaged 55.4 ± 24.5% and 56.3 ± 23.6%, both markedly disparate and statistically different from TTC and LGE measurements of infarct size. As shown in **Figure 4.5**, the serial measurement of 3DK and RSAC demonstrated the dramatic change in the size of these territories between 2 days and 4 weeks. Individual correlations between functional wall motion indices and LGE infarct size are shown graphically in **Figure 4.6**. At the 2-day time point, % abnormal 3DK, % abnormal RSAC, and LV EF correlated significantly (R = 0.74 0.82, and -0.81, respectively) with LGE-

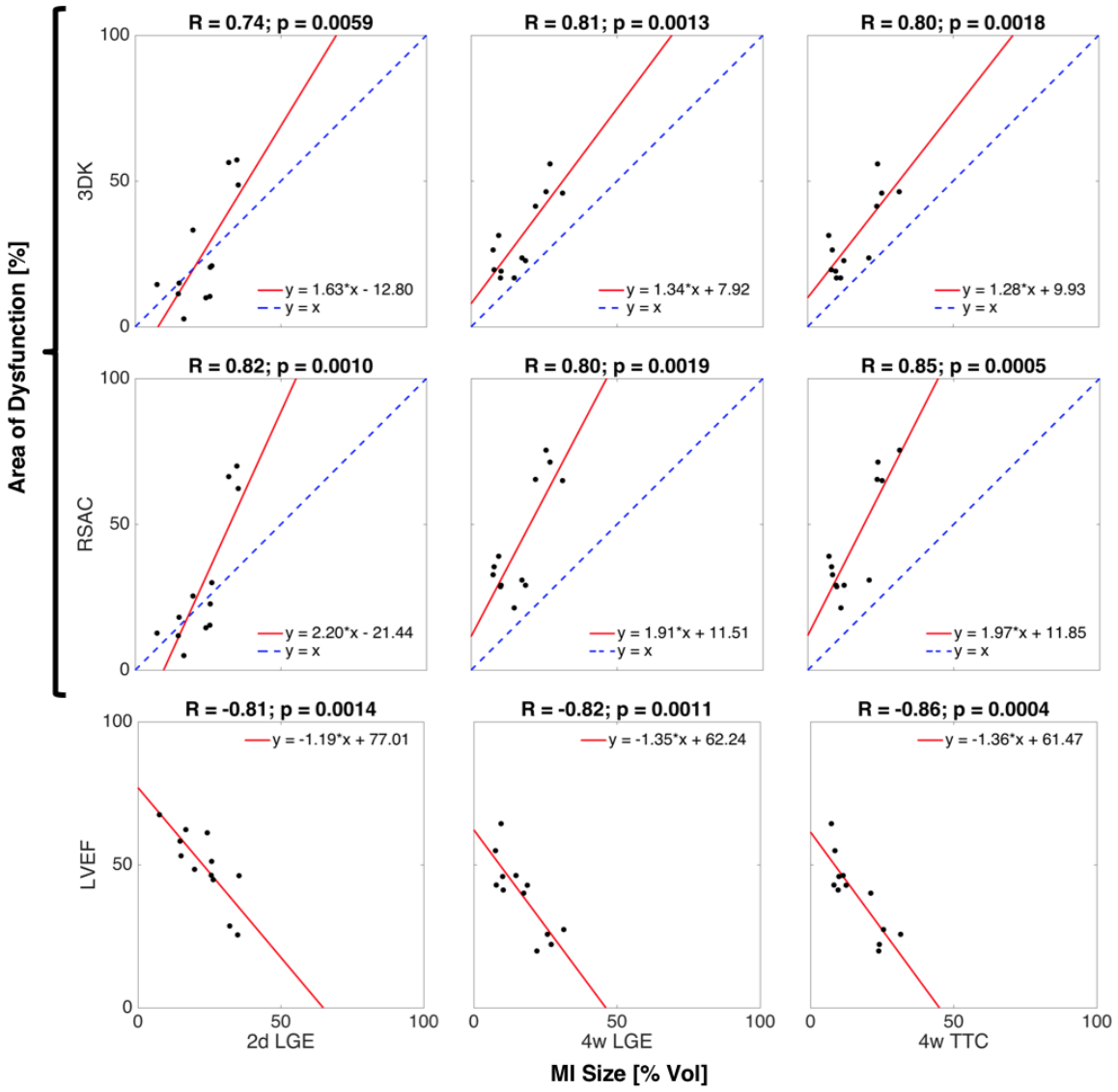

Figure 4.6. Correlations of MI size with area of dysfunction. MI size was measured by LGE or TTC (ordinate) with % abnormal 3DK and RSAC, as well as ejection fraction (EF). Left column: LGE 2 days post-MI. Middle column: LGE 4 weeks post-MI. Right column: TTC 4 weeks post-MI. Of note are the upward shift between 2 days and 4 weeks, and the slopes of all lines, which indicate that the disparity between functional and structural measurements in these parameters increases with MI size.

measured infarct size. Interestingly, the slope of the functional indices we introduce here was 1.63 and 2.20 for 3DK and RSAC, respectively. This indicates that the disparity between

LGE-measured infarct size and the size of the area of dysfunction increases with the size of the injury.

It was notable that the linear correlations, segregated according to 2 days or 4 weeks post infarct, between LGE size and the Z scores for 3DK and RSAC were statistically very significant and strong, **Figure 4.6**, right two columns. However, while the slopes of these correlations were not statistically different between 2 days and 4 weeks, with the remodeling process each linear fit shifted upward, giving rise to different y intercepts between the two time points (see Discussion).

4.3.3. Hemodynamics

The results of hemodynamic measurements are shown in **Figure 4.7** and summarized in **Table 4.2.** In addition to basal measurements, the responsiveness of all conventional micromanometer LV pressure parameters to beta-adrenergic receptor stimulation was defined and calculated as the slope of each relation to variable doses of dobutamine (0.75, 1.0, 2.0, 4.0, 6.0, 8.0 μg/kg/min), **Figure 4.7A-B**. Notable was the inverse correlation between the LV dP/dt max to inotropic stimulation and the LGE infarct size at 4 weeks ($r = -0.64$, $p<0.05$), **Figure 4.7C**. Similar significant correlations were seen between this responsiveness slope of LV dP/dt max to dobutamine and the % abnormal 3DK and % abnormal RSAC, all of which support the prediction that LV force generation post-MI is inversely proportional to the size of an infarct and its associated regional dysfunction.

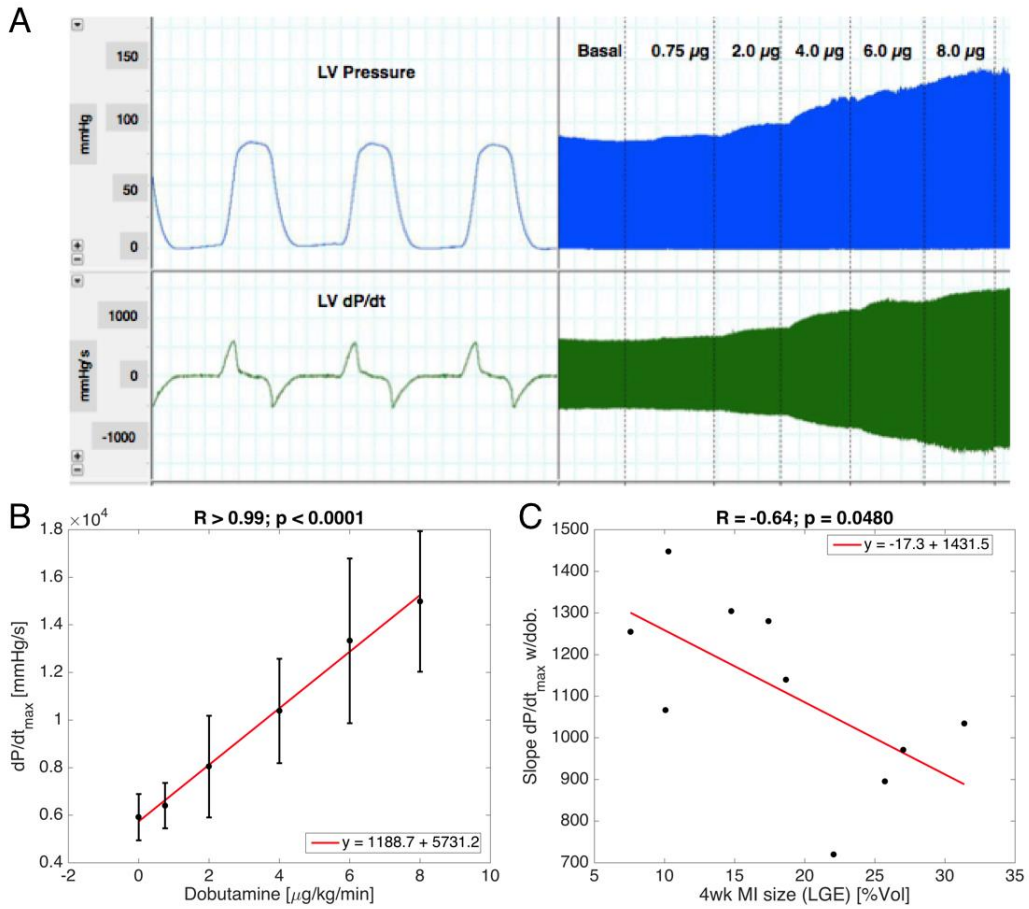

Figure 4.7. Correlation of MI size with inotropic contractile reserve. (A) LV pressure waveform (top), LV dP/dt max (bottom). **(B)** Contractile reserve is defined by the slope of LV dP/dt max to incremental increases of dobutamine concentration. Shown are means of all mice studied (n=11). **(C)** Contractile reserve was significantly correlated with LGE MI size for all mice with both hemodynamic and MR study data (n=10).

Table 4.2. Hemodynamic data

Dobu. Dose [u]	Parameter	Mean ± SD	Parameter	Mean ± SD
Basal (0)	Heart rate [bpm]	401.6 ± 29.4	Max dP/dt [mmHg/s]	5917.1 ± 974.5
0.75		416.9 ± 33.3		6401.9 ± 949.9
2		450.4 ± 31.5		8043.5 ± 2139.2
4		477.6 ± 36.9		10380.0 ±
6		512.1 ± 43.0		13327.5 ±
8		545.9 ± 46.3		14982.5 ±
Basal (0)	Max pressure [mmHg]	88.9 ± 7.7	Min dP/dt [mmHg/s]	-5127.2 ±
0.75		93.0 ± 6.7		-5493.4 ± 847.9
2		107.8 ± 21.9		-6295.6 ±
4		120.7 ± 21.7		-7736.6 ±
6		134.2 ± 23.7		-9457.4 ±
8		135.2 ± 19.6		-10572.2 ±
Basal (0)	EDP [mmHg]	5.0 ± 2.3	Exponential Tau [ms]	5.0 ± 2.3
0.75		5.5 ± 2.5		5.5 ± 2.5
2		6.7 ± 4.9		6.7 ± 4.9
4		6.9 ± 4.7		6.9 ± 4.7
6		7.8 ± 3.7		9.6 ± 1.5
8		8.8 ± 3.7		8.7 ± 1.2

4.4. Discussion

Using LGE magnetic resonance cross-sectional images, we have demonstrated the utility of 3D reconstruction of the mouse left ventricle for precise *in vivo* quantitation of both anatomic and functional indices of myocardial infarct size. We have shown that the gadolinium-labeled area of injury correlates highly with the magnitude of regional dysfunction, the global LV EF, and with both early and late post-injury contractile reserve. The 3D imaging technique also is valuable for its quantitation and display

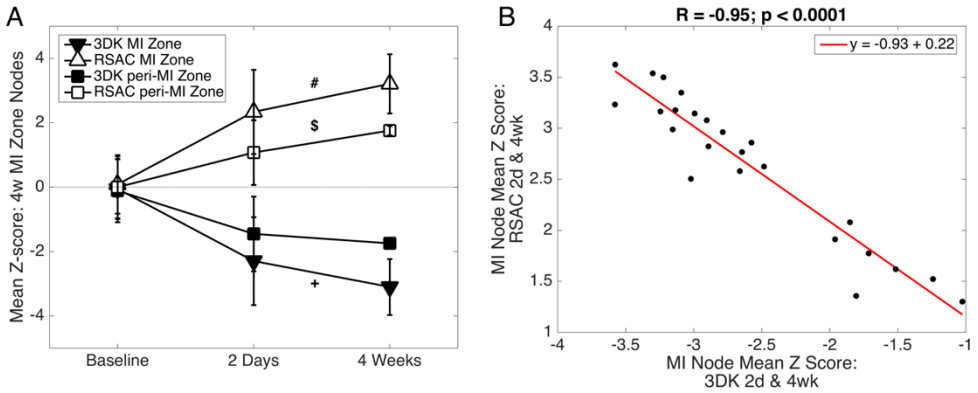

Figure 4.8. Time course of MI zone nodes and correlation of 3DK and RSAC. (A) The evolution of the MI zone (defined as nodes with a Z score greater than 2.0 for RSAC or less than -2.0 for 3DK at 4 weeks). Mean Z scores for MI zone (#) and peri-MI zone ($) nodes of RSAC at 4 weeks were significantly greater than those at 2 days. Only mean Z scores for MI zone (*) nodes of 3DK were significantly different between the two time points. **(B)** RSAC and 3DK MI zone Z scores correlated significantly.

of the remodeling changes as the left ventricle dilates and the infarct area thins and expands, over a period of weeks post-infarct. We believe this approach has significant advantages over 2D echocardiography for assessment in small animals of pharmacologic and genomic interventions aimed at mitigating infarct size and ischemic-reperfusion injury. Moreover, we observed a consistent and strong disparity between the size of the infarct and the area of dysfunctional tissue both at 2 days and 4 weeks post-MI.

4.4.1. Territory of Regional Dysfunction in Mouse Model of Myocardial Infarction

At 2-3 days after left anterior descending ligation, the parametric images (3DK or RSAC) demonstrated that the territory of myocardial dysfunction involved the anterior wall, extending over the anterolateral surface, and around the apex onto the apical-inferior segment of the LV. The distribution of the infarction territory is highly consistent with the distinctive features of mouse coronary artery anatomy as shown in C57Bl/6 mice published by Kumara, et al [28].

Most 2-day, 3DK parametric images showed a distinct area of hyperkinesis along the inferior-basal region of the LV, corresponding to the flow distribution of the mouse right coronary artery [28]. This territory of hyperkinesis appears to be dependent upon the size of the myocardial infarction, since hyperkinesis was less marked in those mice that sustained infarcts that covered a significantly smaller extent of the total surface area of the LV. This localized and compensatory hyperkinetic behavior at 2 days post-infarction, however, does not comport with Yang, et al, who concluded from a murine, 60 minute, ischemia-reperfusion model, using a 2D slice segmental analysis alone, that the fall in EF and rise in ESV at a 24-hour time-point were due primarily to coincident reduction of percentage wall thickening in non-infarcted territory [10]. Their findings may be due to a 2D analysis of minor axis slices acquired at the mid-level of the LV, whereas our observation of hyperkinesis in 3D was in the high inferior-basal territory of the LV. Also, one cannot rule out differences in a given animal's hemodynamic condition at the time when MR images were acquired.

4.4.2. Chronic MI Model

All of the animals in the chronic MI group underwent magnetic resonance imaging prior to the induction of the infarction, and, thus, served as their own controls. The protocol therefore allowed serial assessment of regional dysfunction, over 4 weeks of the relative change in LGE MI size and the evolution of regional and global LV dysfunction as the chamber remodeled in response to the regional injury.

As shown in **Figure 4.5B**, LGE infarct size, at 4 weeks as opposed to 2 days, becomes significantly disparate from the magnitude of regional dysfunction, measured either by 3DK or RSAC. This might be expected as a result of the well-described progressive thinning, expansion, and fibrosis in the infarcted myocardium wall over a period of weeks following

loss of its blood supply [29]. Serial parametric images in a given mouse highlight the progressive dilation of the chamber and expansion of the territory of reduced myocardial shortening **(Figure 4.3)**. It is also instructive to note that the linear correlation between LGE size and the percentage of regional dysfunction remained statistically significant both at 2 days and at 4 weeks. The fitted line of the correlation shifted upward in most mice (except those with very small infarcts), giving rise at 4 weeks to a much larger territory of dysfunction for any given LGE infarct size **(Figure 4.6, middle and right panels)**. Despite these dramatic regional changes with time, the correlation between LGE size and global EF remained nearly the same **(Figure 4.6, bottom row)**.

In order to track more specifically the behavior of the expanding infarct territory, we identified the nodes that were topographically situated within the area of regional dysfunction at 4 weeks (based upon a Z score beyond 2 standard deviations) and then retrospectively analyzed these same nodes on the 2 day scans. As shown in **Figure 4.8A**, these infarct nodes (MI zone) manifested progressively and significantly worsening Z scores between 2 days and 4 weeks post-infarction. The degree of worsening myocardial shortening in the radial direction (3DK) appeared to be approximately the same in magnitude as the aggregate worsening in the circumferential and longitudinal direction (RSAC). Moreover, there was a highly significant inverse correlation between the average 3DK and RSAC Z scores for these MI zone nodes of each mouse, indicating that a displacement index incorporating shortening in the radial direction (3DK) provides no unique information as opposed to one reflecting loss of circumferential and longitudinal shortening (RSAC), **Figure 4.8B**. The parallel deformation of radial and endocardial surface components (circumferential and longitudinal) comports with a previous in vitro observation, which demonstrated isotropic behavior of

rodent myocardium in the region of a myocardial infarction at all time points between 1 and 6 weeks after onset [30]. It is possible that these two indices could become more disparate if the expansion of the infarct worsened further beyond the time post-infarct when we carried out our final image.

4.4.3. Inotropic Reserve and LGE MI Size

As expected, at both 2 days and 4 weeks post infarction, 3DK and RSAC Z scores showed significant inverse correlations with conventional indices of LV global performance, including EF and basal LV dP/dt max. We queried further, however, whether contractile reserve, important to progressive levels of physical exertion, would correlate with our efforts to quantitate both anatomical and functional infarct size. We sought to identify a predictable relationship between myocardial infarct size and global LV contractile force generation in response to beta-adrenergic inotropic stimulation, both before and after the period of LV remodeling.

Gerber et al. have previously described the relationship of regional myocardial strain function and LGE myocardium, and concluded that inotropic reserve was confined to remote myocardium, or areas with non-transmural infarction. Transmural infarction demonstrated absence of inotropic response, and was believed to indicate irreversibly injured myocardium [14].

At 4 weeks, when comparing LGE MI size and the slope of the incremental response of isovolumic max dP/dt to graded doses of dobutamine, we found a highly significant correlation (R = -0.64), **Figure 4.7C**. This observation indicates that LGE infarction size is an inverse determinant of the global inotropic contractile reserve at 4 weeks post-MI. It also

implies that testing of this slope provides a useful approach for the assessment of pharmacologic and cellular interventions aimed at restoring global LV function post-MI.

4.4.4. Limitations

Different anesthetic agents were used for the acquisition of MRI scans (1.5-2.0% isoflurane) and hemodynamic variables (xylazine and ketamine). These agents may cause some differing effects on mouse cardiac function, and thus the correlation of MR-derived LV function parameters and hemodynamic indices should be interpreted with that caveat. The agreement of LV mass by MRI and wet LV weight was not as close as previous studies [3], [22], although it may be due to our smaller sample size, limited extent of axial MR image data, and an increased variability of our LV volume determinations.

4.5. Conclusions

This experimental in vivo murine 3D imaging study has shown that LGE-MR determined infarction size, measured either early or late following a myocardial infarction, is linearly correlated with the percentage of regional dysfunction as well as the EF. Moreover, global LV inotropic reserve, as measured by responsiveness to dobutamine, is highly correlated with the magnitude of LGE labeling.

The 3D reconstructed model of multiplanar slices has now been shown to be a powerful tool for quantitating, localizing and visualizing regional myocardial dysfunction in the mouse left ventricle. The percentage abnormal 3DK and percentage abnormal 3D RSAC both serve as myocardial shortening indices that can be followed serially while the left ventricle remodels and dilates in response to myocardial infarction. Despite wall thinning in the post-MI heart, the calculation of these regional shortening indices, based on endocardial border tracing, remains automatically definable.

The success of 3D reconstructed MR images in this small animal model of myocardial infarction portends a valuable application of the same technique in man for improved prognostication and assessment of therapeutic interventions.

4.6. Acknowledgements

Chapter 4, in full, is in preparation to be submitted for publication. Chao, C.J.; Carruth, E.D.; Bobar, M.; Bradford, W.; Bussell, R.; Gu, Y.; Hoshijima, M.; Peterson, K.L., "Myocardial Infarction Sizing in the Mouse by 3D Multiplanar Reconstruction of Late Gadolinium Enhanced Magnetic Resonance Cardiac Imaging: Correlation with Regional Left Ventricular Dysfunction and Contractile Reserve". The dissertation author contributed equally as a primary co-author of this paper.

4.7. References

[1] S. Kanno, D. L. Lerner, R. B. Schuessler, T. Betsuyaku, K. A. Yamada, J. E. Saffitz, and A. Kovacs, "Echocardiographic evaluation of ventricular remodeling in a mouse model of myocardial infarction," *J. Am. Soc. Echocardiogr.*, vol. 15, no. 6, pp. 601–609, Jun. 2002.

[2] X. Gao, A. M. Dart, E. Dewar, G. Jennings, and X.-J. Du, "Serial echocardiographic assessment of left ventricular dimensions and function after myocardial infarction in mice," *Cardiovasc. Res.*, vol. 45, no. 2, pp. 330–338, Jan. 2000.

[3] A. Bhan, A. Sirker, J. Zhang, A. Protti, N. Catibog, W. Driver, R. Botnar, M. J. Monaghan, and A. M. Shah, "High-frequency speckle tracking echocardiography in the assessment of left ventricular function and remodeling after murine myocardial infarction," *Am. J. Physiol. Circ. Physiol.*, vol. 306, no. 9, pp. H1371–H1383, May 2014.

[4] D. Dawson, C. A. Lygate, J. Saunders, J. E. Schneider, X. Ye, K. Hulbert, J. A. Noble, and S. Neubauer, "Quantitative 3-Dimensional Echocardiography for Accurate and Rapid Cardiac Phenotype Characterization in Mice," *Circulation*, vol. 110, no. 12, pp. 1632–1637, Sep. 2004.

[5] A. Ghanem, C. Troatz, N. Elhafi, O. Dewald, C. Heeschen, G. Nickenig, J. Stypmann, and K. Tiemann, "Quantitation of Myocardial Borderzone Using Reconstructive 3-D Echocardiography After Chronic Infarction in Rats—Incremental Value of Low-Dose Dobutamine," *Ultrasound Med. Biol.*, vol. 34, no. 4, pp. 559–566, Apr. 2008.

[6] A. Akki, A. Gupta, and R. G. Weiss, "Magnetic resonance imaging and spectroscopy of the murine cardiovascular system," *Am. J. Physiol. Circ. Physiol.*, vol. 304, no. 5, pp. H633–H648, Mar. 2013.

[7] S. Bohl, C. A. Lygate, H. Barnes, D. Medway, L.-A. Stork, J. Schulz-Menger, S. Neubauer, and J. E. Schneider, "Advanced methods for quantification of infarct size in mice using three-dimensional high-field late gadolinium enhancement MRI," *Am. J. Physiol. Circ. Physiol.*, vol. 296, no. 4, pp. H1200–H1208, Apr. 2009.

[8] A. Protti, X. Dong, A. Sirker, R. Botnar, and A. M. Shah, "MRI-based prediction of adverse cardiac remodeling after murine myocardial infarction," *Am. J. Physiol. Circ. Physiol.*, vol. 303, no. 3, pp. H309–H314, Aug. 2012.

[9] E. Wu, J. T. Ortiz, P. Tejedor, D. C. Lee, C. Bucciarelli-Ducci, P. Kansal, J. C. Carr, T. A. Holly, D. Lloyd-Jones, F. J. Klocke, and R. O. Bonow, "Infarct size by contrast enhanced cardiac magnetic resonance is a stronger predictor of outcomes than left ventricular ejection fraction or end-systolic volume index: prospective cohort study.," *Heart*, vol. 94, no. 6, pp. 730–6, Jun. 2008.

[10] Z. Yang, S. S. Berr, W. D. Gilson, M.-C. C. Toufektsian, and B. A. French, "Simultaneous Evaluation of Infarct Size and Cardiac Function in Intact Mice by Contrast-Enhanced Cardiac Magnetic Resonance Imaging Reveals Contractile Dysfunction in Noninfarcted Regions Early after Myocardial Infarction," *Circulation*, vol. 109, no. 9, pp. 1161–1167, Mar. 2004.

[11] A. Young, B. French, Z. Yang, B. Cowan, W. Gilson, S. Berr, C. Kramer, and F. Epstein, "Reperfused Myocardial Infarction in Mice: 3D Mapping of Late Gadolinium Enhancement and Strain," *J. Cardiovasc. Magn. Reson.*, vol. 8, no. 5, pp. 685–692, Oct. 2006.

[12] J. S. Chuang, A. Zemljic-Harpf, R. S. Ross, L. R. Frank, A. D. McCulloch, and J. H. Omens, "Determination of three-dimensional ventricular strain distributions in gene-targeted mice using tagged MRI," *Magn. Reson. Med.*, vol. 64, no. 5, pp. 1281–1288, Nov. 2010.

[13] A. Doltra, B. H. Amundsen, R. Gebker, E. Fleck, and S. Kelle, "Emerging concepts for myocardial late gadolinium enhancement MRI.," *Curr. Cardiol. Rev.*, vol. 9, no. 3, pp. 185–90, Aug. 2013.

[14] B. L. Gerber, C. E. Rochitte, D. A. Bluemke, J. A. Melin, P. Crosille, L. C. Becker, and J. A. C. Lima, "Relation between Gd-DTPA contrast enhancement and regional inotropic response in the periphery and center of myocardial infarction," *Circulation*, vol. 104, no. 9, pp. 998–1004, 2001.

[15] G. Geskin, C. M. Kramer, W. J. Rogers, T. M. Theobald, D. Pakstis, Y.-L. L. Hu, and N. Reichek, "Quantitative Assessment of Myocardial Viability After Infarction by Dobutamine Magnetic Resonance Tagging," *Circulation*, vol. 98, no. 3, p. 217 LP-223, Jul. 1998.

[16] W. D. Gilson, Z. Yang, B. A. French, and F. H. Epstein, "Complementary displacement-encoded MRI for contrast-enhanced infarct detection and quantification of myocardial function in mice," *Magn. Reson. Med.*, vol. 51, no. 4, pp. 744–752, Apr. 2004.

[17] W. D. Gilson, Z. Yang, B. A. French, and F. H. Epstein, "Measurement of myocardial mechanics in mice before and after infarction using multislice displacement-encoded MRI with 3D motion encoding," *Am. J. Physiol. Circ. Physiol.*, vol. 288, no. 3, pp. H1491–H1497, Mar. 2005.

[18] R. J. Kim, D. S. Fieno, T. B. Parrish, K. Harris, E. Chen, O. Simonetti, J. Bundy, J. P. Finn, F. J. Klocke, R. M. Judd, O. Simonetti, E. Chen, O. Simonetti, J. Bundy, J. P. Finn, F. J. Klocke, R. M. Judd, E. Chen, O. Simonetti, J. Bundy, and J. P. Finn, "Irreversible injury, infarct age, and contractile function," *Circulation*, vol. 100, pp.

1992–2002, 2002.

[19] S. D. Roes, S. Kelle, T. A. M. Kaandorp, T. Kokocinski, D. Poldermans, H. J. Lamb, E. Boersma, E. E. van der Wall, E. Fleck, A. de Roos, E. Nagel, and J. J. Bax, "Comparison of Myocardial Infarct Size Assessed With Contrast-Enhanced Magnetic Resonance Imaging and Left Ventricular Function and Volumes to Predict Mortality in Patients With Healed Myocardial Infarction," *Am. J. Cardiol.*, vol. 100, no. 6, pp. 930–936, Sep. 2007.

[20] Y. Iwanaga, M. Hoshijima, Y. Gu, M. Iwatate, T. Dieterle, Y. Ikeda, M. Date, J. Chrast, M. Matsuzaki, K. L. Peterson, K. R. Chien, and J. Ross, "Chronic phospholamban inhibition prevents progressive cardiac dysfunction and pathological remodeling after infarction in rats.," *J. Clin. Invest.*, vol. 113, no. 5, pp. 727–36, Mar. 2004.

[21] A. Protti, A. Sirker, A. M. Shah, and R. Botnar, "Late gadolinium enhancement of acute myocardial infarction in mice at 7T: Cine-FLASH versus inversion recovery," *J. Magn. Reson. Imaging*, vol. 32, no. 4, pp. 878–886, Sep. 2010.

[22] C. Csonka, K. Kupai, G. F. Kocsis, G. Novák, V. Fekete, P. Bencsik, T. Csont, and P. Ferdinandy, "Measurement of myocardial infarct size in preclinical studies," *J. Pharmacol. Toxicol. Methods*, vol. 61, no. 2, pp. 163–170, Mar. 2010.

[23] J. Takagawa, Y. Zhang, M. L. Wong, R. E. Sievers, N. K. Kapasi, Y. Wang, Y. Yeghiazarians, R. J. Lee, W. Grossman, and M. L. Springer, "Myocardial infarct size measurement in the mouse chronic infarction model: comparison of area- and length-based approaches," *J. Appl. Physiol.*, vol. 102, no. 6, pp. 2104–2111, Jun. 2007.

[24] A. Pourmorteza, K. H. Schuleri, D. A. Herzka, A. C. Lardo, and E. R. McVeigh, "A new method for cardiac computed tomography regional function assessment: stretch quantifier for endocardial engraved zones (SQUEEZ).," *Circ. Cardiovasc. Imaging*, vol. 5, no. 2, pp. 243–50, Mar. 2012.

[25] F. H. Sheehan, D. K. Stewart, H. T. Dodge, S. Mitten, E. L. Bolson, and B. G. Brown, "Variability in the measurement of regional left ventricular wall motion from contrast angiograms.," *Circulation*, vol. 68, no. 3, pp. 550–9, Sep. 1983.

[26] F. H. Sheehan, E. L. Bolson, H. T. Dodge, D. G. Mathey, J. Schofer, and H. W. Woo, "Advantages and applications of the centerline method for characterizing regional ventricular function.," *Circulation*, vol. 74, no. 2, pp. 293–305, Aug. 1986.

[27] M. B. Smith, H. Li, T. Shen, X. Huang, E. Yusuf, and D. Vavylonis, "Segmentation and tracking of cytoskeletal filaments using open active contours," *Cytoskeleton*, vol. 67, no. 11, pp. 693–705, Nov. 2010.

[28] D. Kumar, T. A. Hacker, J. Buck, L. F. Whitesell, E. H. Kaji, P. S. Douglas, and T. J. Kamp, “Distinct mouse coronary anatomy and myocardial infarction consequent to ligation,” *Coron. Artery Dis.*, vol. 16, no. 1, pp. 41–4, Feb. 2005.

[29] H. F. Weisman, D. E. Bush, J. A. Mannisi, M. L. Weisfeldt, and B. Healy, “Cellular mechanisms of myocardial infarct expansion.,” *Circulation*, vol. 78, no. 1, pp. 186–201, Jul. 1988.

[30] G. M. Fomovsky, S. Thomopoulos, and J. W. Holmes, “Contribution of extracellular matrix to the mechanical properties of the heart,” *J. Mol. Cell. Cardiol.*, vol. 48, no. 3, pp. 490–496, 2010.

5. Conclusion to the Dissertation

In this work, I have shown that regional variations in structural features are very common in the mammalian ventricles, and that such regional variation helps to optimize ventricular function in the normal ventricle. Furthermore, disruptions to the distribution of such structures, e.g. during disease, lead to complex, spatially heterogeneous dysfunction.

Specifically, in Chapter 2 I showed that pressure overload alters the regional distribution of key electrophysiological and calcium handling proteins such as SERCA2a and Cx43, which are known to affect regional tissue mechanics and therefore overall ventricle pump function. These distributions were previously unclear in the rat ventricles and provide useful experimental data for generating computational models of ventricular mechanics to better understand the contributions of protein structures to pump function.

The spatial organization of left ventricular microstructure is known to have a marked effect on functional efficiency. In Chapter 3, we found that the transmural gradients in myocyte geometry and sheet dispersion are diminished in pressure overload. We also demonstrated that these structural features can be detected consistently via DT-MRI, which is non-invasive, non-destructive, comprehensive, and efficient compared to histological methods.

Lastly, in Chapter 4 we showed that a 3D, comprehensive approach to measuring the extent of injury during myocardial infarction using MRI-derived computational models of ventricular geometry are superior to traditional methods of measuring infarct size and dysfunction. We specifically showed that the area of regional dysfunction is significantly larger than the size of a measured infarction, and that this disparity increases with the duration of the coronary occlusion. This novel method for quantifying 3D dysfunction in the mouse is

useful because it provides a straightforward way to more accurately quantify the effect of a pharmacologic or cell-based treatment on regional function and will enable researchers to better identify whether a treatment has any beneficial effect.

Future work could enhance and clarify the findings presented herein. The regional distribution of the proteins examined in Chapter 2 could be more comprehensively characterized with a more consistent histological approach, as long as objective quantification was successfully implemented. Additionally, only a handful of select electrophysiological and calcium handling proteins were investigated, even though there are myriad proteins with important functions that vary regionally and are altered during disease. Building a library of 3D heterogeneous protein densities in normal and diseased hearts would be beneficial for building computational models of ventricular mechanics. Such models provide an excellent means to identify key contributors to dysfunction during disease.

Although the correlations between regional variations in tissue microstructure and DTI-derived parameters (Chapter 3) were statistically significant, it is possible that other structural features are involved in modulating the DT-MRI signal. A critical study that has not been done would be to model a diffusion MRI experiment in computational models of cardiac tissue microstructure in order to determine the relative contributions of altered structural properties to parameters such as anisotropy. Such computational methods would also allow for separating the otherwise linked variations in fiber or sheet dispersion and linear or planar anisotropy, respectively. The diminished gradient of myocyte geometry in pressure overload undoubtedly affects ventricular mechanics, but because of the complexity of ventricular structure and function, understanding how they do so is not straightforward. Again, computational models of left ventricular mechanics constitute an ideal method for

determining this effect, especially if combined with protein density distributions or other known forms of remodeling.

The 3D regional dysfunction we observed in Chapter 4 was wholly dependent on 5-7 1-mm thick short-axis slices that spanned the length of the left ventricle. Because of longitudinal (through plane) deformation and the limits of MR imaging, including the partial volume effect, there is undoubtedly error in the calculation of endocardial geometry. One simple way to improve this method is to acquire two to three long-axis slices, which would help to define the curvature and function of the apex, as well as define more concretely the valve plane so that the model spans the entire ventricle. Indeed, we have already begun implementing this improvement and seen a beneficial effect [unpublished data].

A major bottleneck to this approach is manual segmentation of ENDO and EPI borders. Convolutional neural networks may provide a much faster, automated approach to segmentation that would remove the current bottleneck and make this method even more useful to the research community. We have begun developing such a tool using available data from human cardiac cine-MRI scans with promising results. However, it must be cautioned that the quality of segmentation has a very strong influence on the results of this type of analysis and so any automated method to perform the segmentation must be extremely well tuned, or the benefit would be lost. Semi-automation would remain as a potential approach.

As shown in this dissertation, generalizations from global or localized measurement are insufficient to characterize structure-function relationships in the heart, whereas regional variations in structure and function are critical to understanding normal pump function and the spatially heterogeneous remodeling response that occurs in cardiac disease.